Properties of electrospun superconducting and magnetoresistive nanowires

Dissertation

zur Erlangung des Grades
des Doktors der Naturwissenschaften
der Naturwissenschaftlich-Technischen Fakultät NT
der Universität des Saarlandes

von

XianLin Zeng

Saarbrücken, 2019

Tag des Kolloquiums:	18. November 2019
Dekan:	Prof. Dr. G. Jung
Berichterstatter/in:	Prof. Dr. U. Hartmann Prof. Dr. R. Birringer
Vorsitzende/r:	Prof. Dr. F. Wilhelm-Mauch
Akad. Mitarbeiter/in:	Dr. T. John

Declaration of Authorship

I hereby certify that this thesis has been composed by me and is based on my own work, unless stated otherwise. All references and verbatim extracts have been quoted, and all sources of information, including graphs and data sets, have been identified.

Hiermit versichere ich, die vorliegende Arbeit selbstständig verfasst und keine anderen als die angegebenen Quellen und Hilfsmittel benutzt sowie die Zitate deutlich kenntlich gemacht zu haben.

Saarbrücken, August 5, 2019

XianLin Zeng

Abstract

Superconducting nanofibers (nanowires and nanoribbons) and magnetoresistive nanowires were fabricated by the electrospinning technique accompanied with appropriate thermal treatment. The mechanism of electrospinning is introduced. The key points of producing nanoribbons and the idea of parallel nanofiber collection are demonstrated. To obtain the superconducting or magnetoresistive phases while maintaining the fiber structure, a thermal treatment based on the thermal gravity analysis is proposed.

The investigation of the superconducting nanofibers is based on two cuprate superconducting materials: $La_{1.85}Sr_{0.15}CuO_4$ and $Bi_2Sr_2CaCu_2O_8$ (Bi-2212). A comparison of the superconductivity between $La_{1.85}Sr_{0.15}CuO_4$ nanowires and nanoribbons is presented. The magnetic and electric properties of the Bi-2212 nanowire networks are presented, including a comparison between pure Bi-2212, Pb-doped Bi-2212, and Li-doped Bi-2212 nanowire networks. The extended critical state model is applied for the critical current density estimation, and a Josephson junction network model is proposed to explain the unique features of the electric properties. As a special section, the properties of a single Bi-2212 thick fiber are also demonstrated.

The characterization of the magnetoresistive nanowire networks is based on the perovskite materials $La_{1-x}Sr_xMnO_3$. The influence of the Sr doping level on the magnetic properties and magnetoresistance is discussed.

At the end, the properties of $La_{1.85}Sr_{0.15}CuO_4/La_{0.7}Sr_{0.3}MnO_3$ hybrid nanowire networks are presented.

Zusammenfassung

Supraleitende Nanofasern und magnetoresistive Nanodrähte wurden durch Elektrospinnen und entsprechende Temperaturbehandlung hergestellt. Der Mechanismus des Elektrospinnens wird vorgestellt. Die Kernpunkte der Herstellung von Nanobändern und die Idee des Auffangens von parallelen Nanofasern werden demonstriert. Um supraleitende oder magnetoresistive Phasen unter Erhalt der Faserstruktur zu erzeugen, wird die Temperaturbehandlung basierend auf einer thermogravimetrischen Analyse vorgeschlagen.
Die Untersuchung der supraleitenden Nanofasern basiert auf den zwei Kuprat-Supraleitern $La_{1.85}Sr_{0.15}CuO_4$ und $Bi_2Sr_2CaCu_2O_8$ (Bi-2212). Ein Vergleich der supraleitenden Eigenschaften zwischen $La_{1.85}Sr_{0.15}CuO_4$ Nanodrähten und Nanobändern wird vorgestellt. Die magnetischen und elektrischen Eigenschaften der Bi-2212 - Netzwerke, mit reiner Bi-2212 Phase, aber auch Pb - und Li - dotierten Phasen, werden präsentiert. Das erweiterte Bean-Modell des kritischen Zustandes wird zur Bestimmung der kritischen Stromdichte angewendet und ein Modell eines Netzwerks bestehend aus Josephson-Kontakten wird vorgeschlagen, um die einzigartigen elektrischen Eigenschaften zu erklären. In einem eigenen Abschnitt werden die Eigenschaften einer einzelnen, dicken Bi-2212 Faser demonstriert.
Die Eigenschaften von magnetoresistiven Nanodrahtnetzwerken werden anhand des Perowskits $La_{1-x}Sr_xMnO_3$ untersucht. Der Einfluss des Dotierungsgrads von Sr auf die magnetischen und magnetoresistiven Eigenschaften wird diskutiert. Zum Schluss werden die Eigenschaften von hybriden $La_{1.85}Sr_{0.15}CuO_4/La_{0.7}Sr_{0.3}MnO_3$ - Nanodrahtnetzwerken präsentiert.

Acknowledgments

Here I would like to thank all the people who supported me in my Ph.D. work from the start.
Firstly I want to thank Prof. Dr. Uwe Hartmann. He suggested my interesting research topic and provided support in experimentation.
Secondly, I would like to thank Dr. Michael Koblischka. He supervised my whole Ph.D. work and gave me a lot of suggestions about the practical modalities of my experiments. I learned a lot from Dr. Koblischka on how to write a paper.
I would like to thank Prof. Dr. Jian-Min Li. He is my former supervisor during my post-graduate stage. And he still gives me a lot of suggestions and measurement support like the SQUID and the MTGA measurements.
Then I would like to thank all other people supporting me in my research: Prof. Dr. Volker Presser for providing me the electrospinning instrument. This was the main instrument for my nanowire fabrication; Mr. Jörg Schmauch (AG Birringer) for the TEM, EDX and EBSD characterisation; Michael Deckarm (AG Birringer) for performing XRD measurements; Prof. Birringer for providing the PPMS for magnetic properties characterisation and Dr. Flavio Soldera (AG Mücklich) for the FIB preparation of single wires.
Furthermore, I would like to Prof. Dr. Leon Abelmann for fruitful discussions.
Then I would like to thank my colleague Thomas Karwoth. He made a significant contribution to my work like establishing the electric measurement system with the cryostat and software programming. We had frequent discussions and collaborations on the sample measurements and data analysis.
I would like to thank my colleagues Anne Holtsch and Fabian Laurent. They provided a lot of useful suggestions on the correction of my thesis. I appreciate their time and effort.
I would also like to thank the Volkswagen Foundation and the German Research Foundation (Deutsche Forschungsgemeinschaft) for their financial support granted by the funding initiative "Experiment!".

Abbreviations

Table 1: List of abbreviations I

1112 precursor	A precursor with the molar ratio of Bi : Sr : Ca : Cu = 1 : 1 : 1 : 2
1D	One-dimensional
2D	Two-dimensional
AFM	Atomic force microscopy
APS	Anti-phase slip
BCS theory	Theory established by J. Bardeen, L. N. Cooper and J. R. Schrieffer
Bi-2201	$Bi_2Sr_2CuO_6$
Bi-2212	$Bi_2Sr_2CaCu_2O_8$
BSCCO	Superconductors with elements Bi, Sr, Ca, Cu, and O
CMR	Colossal magnetoresistance
CSM	Critical state model
DSC	Differential scanning calorimetry spectrum
ECSM	Extended critical state model
FC	Field cooling
FIB	Focused ion beam technique
FWHM	Full width at half maximum
GB	Grain boundary
GL theory	Ginzburg-Landau theory
H_c	Critical magnetic field
H_{irr}	Irreversibility field
HTSc	High temperature superconductor
k_B	The Boltzmann constant
LAMH theory	Theory developed by Langer, Ambegaokar, McCumber, and Halperin
LSCO	$La_{1.85}Sr_{0.15}CuO_4$
LSMO	$La_{1-x}Sr_xMnO_3$
MI transition	Metal-insulator transition
MIBK	Methyl-isobutyl-ketone
PMMA	Poly(methyl methacrylate)
PPMS	Physical properties measurement system
PVP	Polyvinylpyrrolidone (M.W. 1,300,000)
QPS	Quantum phase slip
RCSJ	A resistively and capacitively shunted junction
RP phase	Ruddlesden-Popper phase

Table 2: List of abbreviations II

SEM	Scanning electron microscope
TAFF	Thermal activation of flux flow
TAPS	Thermally activated phase slips
T_c	Critical temperature
TEM	Transmission electron microscope
TGA	Thermal gravity analysis
V_c	Critical voltage
ξ	Coherence length
ZFC	Zero field cooling

Contents

1 Introduction

Electrospinning is a fiber fabrication technique in an electrical environment. Continuous microscale fibers are created from a charged jet of polymer solution or melt. This technique is applied to produce ultrathin fibers in biomedical and industrial fields.
The initial idea of electrospinning originated in 1934. Anton and Formhals [1, 2, 3] patented an experimental setup for a polymer filament preparation by electrostatic forces. Until 1966, an improved apparatus was demonstrated by Simons [4]. It was able to fabricate continuous ultrathin fibers by electrical spinning. In 1969, a theoretical study of the electrospinning process was given by Taylor [5]. An angle of 49.3° was determined as the critical angle at which the surface tension is in balance with the electric field. The conical shape of the droplet was then referred to as the 'Taylor cone'. Research on electrospinning gained further traction due to the increasing knowledge of the application potential of nanofibers in various fields. Electrospinning is a relative clean preparation method for fibers with diameters of micro- to nanometer scale via a contactless procedure. Unlike self-assembly, it is less complex and focuses on polycrystalline materials. Combined with the sol-gel method, which has the advantage of synthesizing multi-element polycrystalline materials, electrospinning can be applied for a wide range of organic and inorganic nanofiber fabrication. This offers some unique advantages such as high surface to volume ratio, adjustable porosity of the electrospun structure and flexibility to spin into various shapes and sizes.
Originating from the discovery in 1911, superconductors have inspired a significant development of condensed matter physics. With the zero electrical DC resistance and the flux expulsion (Meissner effect), superconductors possess attributes which make them enormous open topics of theoretical research and high potential in industrial applications. The theoretical explanation of superconductivity went through a long history from phenomenological theories like the London theory to a phonon–conventional theory. The BCS theory (established by J. Bardeen, L. N. Cooper and J. R. Schrieffer in 1957) successfully reveals the microscopic mechanism of conventional superconductors [6, 7, 8]. According to the BCS theory, the superconducting state is a quantum state of two electrons, a so-called Cooper pair. The pairing electrons interact through the exchange of a virtual phonon in a certain distance (coherence length) and keep themselves always in the same phase, which leads to no energy consumption during their movement in external electric fields. This is the origin of the non-resistance phenomenon. The BCS theory predicted a temperature limit of 40 K for a transition to the superconducting state. However, the appearance of cuprate

superconductors contradicted this prediction. The cuprate superconductors are called unconventional superconductors as they do not conform to the BCS theory. Before the discovery of iron-based superconductors in 2008, cuprate superconductors were believed to be the only oxide superconductor family showing high-temperature superconductivity.

High critical temperatures and remarkable critical current densities lead to cuprate superconductors having superior energy transportation properties compared to conventional superconductors. Additionally, the pinning force properties provide wider application potential and inspire further investigation. Theoretical mechanisms of the superconductivity of cuprates have been developed for decades. The central issue is the layered two-dimensional (2D) structure of copper oxides (called the CuO2 plane), on which the carrier Cooper pairs, substituting for electron Cooper pairs, occur. Such carrier pairs are induced by the loss of the oxygen component or the dopant in the rare earth oxide layer. Several theoretical publications [9, 10, 11] propose that cuprate superconductivity might be rooted in a 2D Bose-Einstein condensate (BEC) of Cooper pairs pre-existing above the critical temperature, which are coupled through a BCS-like phonon mechanism. However, a precise description of the dynamic nature of those pairs is unestablished. The mechanism of cuprate superconductivity is still under intensive research.

With the progress of nanotechnology, research in the field of the superconductivity comes to the nanoscale era. The 2D systems have been proved to maintain superconductivity. Meanwhile, various interface effects induced by the layered structures enable to tailor the superconductivity of these materials. Over decades, blossoms of researches on 2D superconductors appear, especially in quantum physics. Compared to 2D systems, the one-dimensional (1D) systems are more complicated. When the diameter d of a fiber is smaller than the superconducting coherence length ξ, it is classified as 1D. In this case, the superconducting condensate wave function depends only on the position along the axis of the fiber. If $\xi < d < \pi\sqrt{2}\xi$, the vortices of the fiber are not energetically stable, still, the order parameter is approximately constant within the cross-section of the fiber. Such a fiber is classified as quasi-one-dimensional (quasi-1D) [13]. The Mermin–Wagner theorem [14] points out that superconducting long-range order and zero resistance are forbidden in the limit of a strictly 1D system. This indicates that the superconducting properties of the nanowires can be entirely different from those of bulk superconductors. The physics of 1D superconducting nanowires is abundant, with a large number of unresolved puzzles. The main issues focus on the non-zero resistivity below T_c. The theory of thermally activated phase slip (TAPS) was developed by Langer, Ambegaokar, McCumber, and Halperin (LAMH) [15, 16] to provide an explanation of such non-zero resistance behavior. However, this theory is not suitable to explain the non-zero resistance behavior far below T_c. A theory based on the quantum fluctuation was established to solve this problem [17, 18], with the effect called quantum phase slip (QPS).

The high-temperature superconducting material $Bi_2Sr_2CaCu_2O_8$ (Bi-2212)

presents lattice anisotropy even in the coherence length. Generally, the coherence length obeys the equation $\xi(T) = \xi(0)(1 - T/T_c)^{-1/2}$ [8]. However, the coherence length in the lattice *ab* plane ξ_a is around 3.8 nm, which is much larger than the one along the *c* axis ξ_c, which is around 0.2 nm [19]. The QPS appears when a fiber is 1D or quasi-1D [20]. One can not expect to discover the QPSs in a fiber with the diameter on the scale of 100 nm. Relatively, the TAPSs have been discovered in a superconducting whisker with a diameter of roughly 500 nm [21]. This indicates that even when the diameter of the fiber is ten times larger than its coherence length, the influence of the thermal fluctuation is not negligible.

In polycrystalline superconductors, grain boundaries (GBs) play an important role. GBs appear when the lattice orientation of a group of grains is different from the lattice orientation of another group, or defects like lattice distortions or oxygen vacancies appear in a certain region of the crystal. This has been investigated in polycrystalline thin films for decades [22, 23, 24, 25]. Generally, the GBs function as non-superconducting layers in the film. Therefore, polycrystalline thin films consist of Josephson junctions. The nanowires fabricated by electrospinning technique are randomly aligned on the collector, with the diameter being in the 100 nm scale. The nanowires cross each other, forming a network system with inter-wire weak links. Such a network system looks similar to a porous thin film system with a thickness of ∼100 nm. In this case, the superconducting behavior of such a system should not be special. However, an unexpected feature is found in the electric behavior of such a network system, which will be presented in the following chapters.

The La-based perovskite superconductors were the pioneering material that attracted the attention of researchers to cuprate superconductors. Beginning with the discovery of $LaBaCuO_4$ ($T_c = 35$ K) by J. G. Bednorz and K. A. Müller in 1986, a new family of materials called high-temperature superconductors (HTSc) was induced. In the same year, another La-based perovskite, $La_{2-x}Sr_xCuO_4$ was found to be superconducting, the higher T_c stemmed from the optimised Sr doping level of the materials ($La_{1.85}Sr_{0.15}CuO_4$, $T_c = 39$ K). Similar to other cuprate superconductors, it has a small value of the coherence length of $\xi(0)$ ∼6 nm [26] and a penetration depth of ∼100 nm [27]. For the $La_{1.85}Sr_{0.15}CuO_4$ nanowires with a diameter of around 180 nm, the superconductivity has already been confirmed [28]. But what about ribbons with a thickness of less than 100 nm? Will the Meissner effect be observed? The answers are given in this work. For an accurate description, $La_{2-x}Sr_xCuO_4$ has a Ruddlesden-Popper (RP) phase, consisting of 2D perovskite layers interleaved with cations. On the other hand, $La_{1-x}Sr_xMnO_3$, a La-based manganite with simplified perovskite structure, is a member of the well-known materials with colossal magnetoresistance (CMR) . The question, how do the CMR materials interact with superconductors, is a significant issue appealing in physics and of importance in device application. This has been investigated in thin film systems by Blagoev [35]. However, the superconductor they chose was $YBaCu_2O_7$, whose lattice structure is far different from La-based perovskites. So what would happen if both the

chosen superconductor and the CMR materials have similar lattice structures? Furthermore, what would happen if the interaction occured in the full crossover structure? These questions are answered in this work.
This thesis is mainly focused on the characterization of the electric and magnetic properties of the electrospun nanowires based on the background above. In chapter 2, a theoretical framework of electrospinning and superconductivity is given, including an introduction of granular superconductors and the model estimation for critical current densities from a magnetic measurement. In chapter 3, the setups for the experiments are introduced. In chapter 4, details of the sample preparation are described, including a discussion about the influence of the thermal treatment. In chapter 5, the main results of the electrospun nanowires are shown, including the characterization of the properties of $La_{1.85}Sr_{0.15}CuO_4$ (LSCO) nanowires/nanoribbons, Bi-2212 nanowires and the $La_{1.85}Sr_{0.15}CuO_4/La_{0.7}Sr_{0.3}MnO_3$ hybrid nanowire networks. In chapter 6, conclusions and an outlook for future investigations are given.

2 Fundamentals

This chapter is separated into five sections. The first section demonstrates the mechanism of electrospinning and the process of fiber formation, including a discussion about the parameters controlling the fiber morphology. The second section introduces three established theories of the mechanism of superconductivity. The third section introduces one type of junction consisting of superconductors and non-superconducting materials. This junction plays an important role in the electric properties of the nanowire network system in this work. The fourth section introduces two types of phase slip behaviors existing in a 1D superconducting system. The last section presents the traditional and an extended approach of an estimation of the critical current density from the magnetization data of superconductors.

2.1 Electrospinning

A schematic drawing of the electrospinning instrument is shown in Fig. 2.1. A basic electrospinning setup consists of four components: a high-voltage power supply, a microspeed boost pump, a conducting spinneret and a collector with a certain distance from the spinneret. The spinneret is always fixed on the syringe and connected to the high-voltage power supply. In order to obtain an optimal electric field, the collector is grounded, and the whole setup is usually stored in a sealed cage to maintain a relatively stable low humidity.
The mechanism of electrospinning can be described as follows: a droplet appears at the bottom of the spinneret when the precursor is pushed out by the microspeed boost pump. Due to the connection with the high-voltage power supply, the electrons escape from the droplet. The droplet is then charged positively. The charged droplet experiences both the surface tension and a Coulomb force from the external electric field between the spinneret and the grounding collector. The electrostatic interaction results in the elongation of the droplet from a hemisphere to a conical object. This conical object is known as the 'Taylor cone' [5]. Once the applied voltage reaches the critical value (V_c), the electrostatic force overcomes the surface tension. A jet appears at the bottom of the cone. The jet experiences elongation by the electric field and rapid evaporation of the solvent, forming a polymeric fiber before it arrives at the collector. The electric instability of the jet leads to the fiber locating on the collector with a random orientation.
The whole electrospinning process can be separated into three parts: jet initiation, jet thinning and jet solidification.

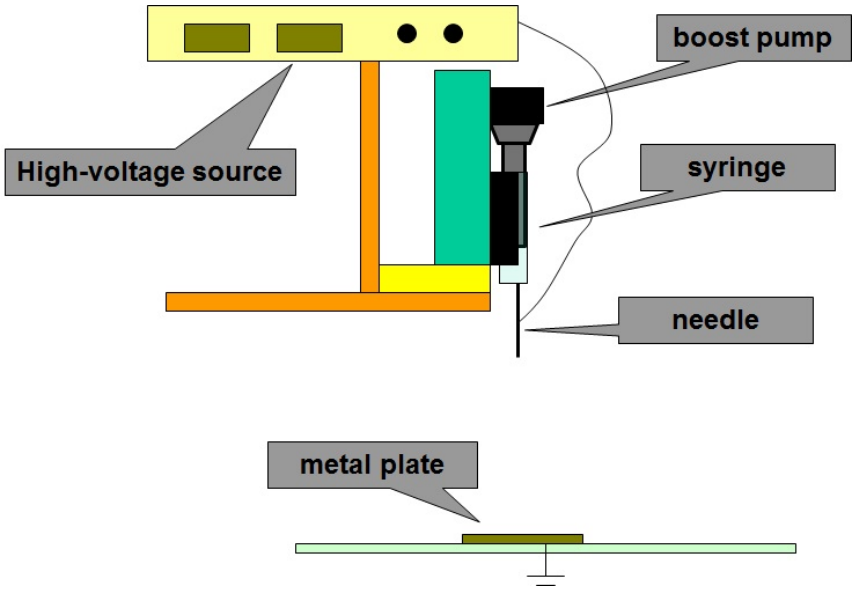

Figure 2.1: Scheme of the electrospinning setup.

2.1.1 Jet initiation

When a droplet of the precursor is pushed out from the orifice, it is charged because of the connection with the high-voltage power supply. For a fixed quantity of fluid, the Coulomb repulsion between the charged ions in the droplet favors the jet-like formation, while the surface tension of the fluid prefers sphere-like shapes with a smaller surface area per unit mass. Therefore, in the beginning, the surface tension makes the droplet form a hemisphere. The electrostatic force between the spinneret and the grounding collector elongates the droplet towards a cone shape. Taylor proposed that the attractive force F_a and the square of the voltage V between the jet and the grounding collector obey a proportional relationship as follows [5]:

$$V^2 \sim 4F_\mathrm{a}\left(\frac{H^2}{L^2}\right)\left(\ln\frac{2L}{R}-1.5\right), \tag{2.1}$$

where H is the distance between the orifice and the vertical projection on the collector, L is the length of the spinneret, R is the radius of the spinneret. When the applied voltage reaches V_c, the attractive force F_a overcomes the surface tension and lets the jet, forming at the tip of the Taylor cone, eject. The highest charge density appears at the tip of the Taylor cone.
Spivak et al. provided a mathematical model of the steady state of the jet, considering a steady-state flow of an infinite viscous jet pulled from a capillary orifice and accelerated by a constant external electric field. The initial radius R_0 is given by [36]:

$$R_0 = 2[\varepsilon_0\sigma_0]^{\frac{1}{3}}(\frac{Q}{J})^{\frac{2}{3}}, \tag{2.2}$$

where ε_0 is the permittivity of vacuum, σ_0 is the coefficient of surface tension γ, Q is the volumetric flow rate and J is the electric current.

2.1.2 Jet thinning

Once the jet is established, the uncompensated ions from the electrical charges are carried away by the flowing jet. Thus before reaching the collector, the jet experiences a thinning process by the electrostatic force. Especially for the low-viscosity precursor, the thinning rate of the jet depends on the flow rate of the precursor. The faster the precursor flows, the smaller the radius of the jet becomes. This has been explained by Deitzel et al. [37] with a simplified cylinder model of an electrospinning jet segment. Assuming the height and the radius of the segment as h and R, the ratio of surface area to volume is given by the equation below [37]:

$$\frac{A}{V} = \frac{2\pi Rh}{\pi R^2 h} = \frac{2}{R}. \tag{2.3}$$

The acceleration of the jet flow a is determined by the experienced electric force, thus it can be expressed as

$$a = E(\frac{q}{m}), \tag{2.4}$$

where E is the external electric field, q is the charge in the jet segment and m is the segment mass. The density of the polymer solution and the surface charge density are regarded as constant. The relationship between the acceleration a and the jet radius R can be written as

$$a \sim \frac{q}{m} \sim \frac{A}{V} = \frac{2}{R} \implies a \sim \frac{2}{R}. \tag{2.5}$$

With the development of the jet, its shape becomes longer and thinner. The time of the excessive charge redistribution along the whole jet becomes longer. The repulsive Coulomb forces between the excessive charges elongate the jet along the direction of its cylindrical axis until the jet solidifies. The competition between the repulsive charges and the surface tension of the jet provides a perturbance to the straight segment of the jet. The growth path of the charged jet is quickly bent into a three-dimensional coil, which is carried down-stream and increased in diameter as both the elongation and the bending continue. Typically, the electrical bending coil starts to form at a particular distance from the orifice, and the diameter of turns of the coil grows larger and moves toward the collector [38].

2.1.3 Jet solidification

The fiber forming from the jet experiences a rapid liquid evaporation and solidification process. The solidification rate is determined by the viscosity of

the precursor, electrostatic field, and gap distance. Yarin et al. described the mass decrease and the shape variation of the fiber during the evaporation and solidification by using a quasi-1D equation. They reported that the radius of the dry fiber was about 1/1000 of the initial fluid jet [39].
The electrical bending of the jet results in a complicated fiber path. When the fiber locates at the collector, a conglutination appears inevitably at partial crossing points of the fiber. Therefore, the fiber forms a network structure.

2.1.4 Formation of ribbon structure

The surface evaporation plays an important role in the cross-section shape formation of the electrospun fiber. When the concentration of the precursor is high enough, a 'thick skin' forms on the surface of the jet during the rapid evaporation (Fig. 2.2a). Then the inner part becomes hollow after the evaporation of the inner solvent (Fig. 2.2b). Atmospheric pressure forces the tube formed by the 'thick skin' to collapse. The circular cross section becomes elliptical and then flat (Fig. 2.2c). As the collapse occurs, the electrical charges distributed uniformly on the cylindrical jet tend to flow to the long axis edges of the ellipse, where they produce a lateral force that favors the collapse, forming a ribbon with a cross-sectional perimeter of nearly the same magnitude as the perimeter of the jet (Fig. 2.2d).

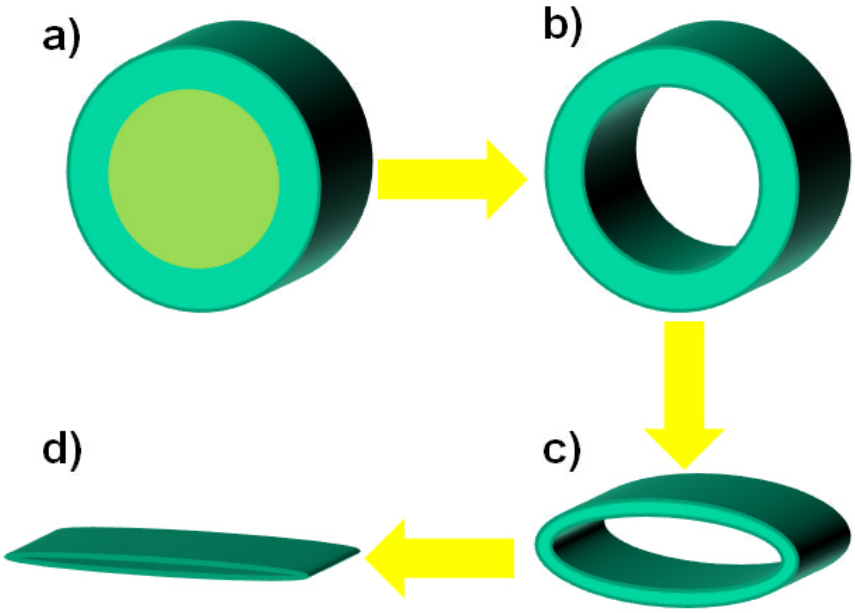

Figure 2.2: Formation of an electrospun nanoribbon. a) A 'thick skin' forms when the precursor concentration is high enough; b) The inner solvent evaporates and a hollow forms in the center; c) The hole collapses due to the outer atmospheric pressure; d) A ribbon forms after the charge redistribution.

Guenthner et al. have provided a fluidics dynamic model describing the formation process of the electrospun fiber during the evaporation and solidification [40]. The model starts with an adiabatic quasi-cylinder fluid with a gradient concentration in the cross-section. The initial distribution of polymer in the system is considered to be homogeneous. However, a concentration fluctuation is introduced by thermal perturbation at the interface boundary which is in contact with the surrounding air. The Péclet number Pe is defined as a value which determines the cross-section shape formation of the fluidic fiber [41]:

$$Pe = \frac{\alpha_0}{\Lambda} \frac{\kappa^{1/2}}{\Delta R}. \tag{2.6}$$

The value Pe describes the ratio of advective and diffusive effects in the system. In the equation (2.6), α_0 is the diffusivity of the solvent through the densified polymer skin to the surrounding air, Λ is the concentration-dependent mobility of the polymer solution, κ is the coefficient of the interface gradient, while ΔR is the thickness of the 'skin'.
According to Guenthner's model, when Pe is low, the system is in a solution with slow diffusional flux. A significant amount of polymer will diffuse away from the inner wall towards the center of the fiber, resulting in a gradual increase of polymer concentration at the core. In this case, a fiber with a decreasing diameter after the evaporation is formed. On the other hand, if Pe is high, the system is in a solution with a fast diffusional flux. A thin skin forms rapidly. The concentration of the skin remains sharply differentiated from the fiber core throughout the evaporation process. This prevents the polymer from diffusing completely before being swept up by the advancing wall. With the help of a faster solvent evaporation rate, the system tends to form a hollow fiber with a distinct skin layer. Further influenced by the atmospheric pressure and the Coulomb force of the redistributed charge, a ribbon structure is eventually formed.

2.2 Superconductivity

Superconductivity stems from the behavior of certain materials through which the current can pass without consumption of any energy. On closer inspection, superconductivity consists of two basic properties: zero DC resistance and the ability of external magnetic field expulsion. The latter property is also called the 'Meissner effect'. The superconducting state is constricted by external experimental factors such as temperature, applied current, and external magnetic field. Correspondingly, there are three critical values defined as critical temperature T_c, critical current I_c (current density j_c) and critical field H_c, which are used to describe the environmental limits of the superconducting state.

2.2.1 London theory

Right after the discovery of the Meissner effect, the first phenomenological theory of superconductivity was established by the brothers Fritz and Heinz London, therefore called the 'London theory'. The core of the theory lies in the 'London equations' as shown below [6]:

$$\begin{aligned} \frac{\partial \mathbf{j}_\mathrm{s}}{\partial t} &= \frac{n_2 e^2}{m}\mathbf{E}, \\ \nabla \times \mathbf{j}_\mathrm{s} &= -\frac{n_2 e^2}{m}\mathbf{B}. \end{aligned} \tag{2.7}$$

Here $\mathbf{j}_\mathrm{s}$ is the superconducting current density, $\mathbf{E}$ and $\mathbf{B}$ are the electric and magnetic fields within the superconductor, respectively, e is the charge of an electron, m is electron mass, and n_s is a phenomenological constant loosely associated with the number density of superconducting carriers. If the second London equation is manipulated by applying Ampere's law $\nabla \times \mathbf{B} = \mu_0 \mathbf{j}$, the expression of the magnetic field can be written as

$$\begin{aligned} \nabla^2 \mathbf{B} &= \frac{1}{\lambda^2}\mathbf{B}, \\ \text{with } \lambda &= \sqrt{\frac{m}{\mu_0 n_\mathrm{s} e^2}}. \end{aligned} \tag{2.8}$$

Considering a depth x from the surface, the solution of equation (2.8) can be described as $B_\mathrm{z}(x) = B_0 e^{-x/\lambda}$. Here, λ is defined as the 'London penetration depth'. The London theory managed to explain the Meissner effect, it pointed out the exponential dependence of the magnetic field penetrating the superconductor.

2.2.2 Ginzburg-Landau theory

In 1950, Ginzburg and Landau established a mathematical theory to describe superconductivity. It was a phenomenological model which could describe the Type I superconductors without examining their microscopic properties. Lev Gor'kov [42] reported a later version derived from the BSC theory, providing a quantum mechanical description for the wave function of the superconducting charge carriers and an expression for the free energy of the resulting thermodynamic system near and below T_c. The Helmholtz free energy of a superconductor is defined by [7]:

$$F = F_n + \alpha|\psi|^2 + \frac{\beta}{2}|\psi|^4 + \frac{1}{2m}\left|(-i\hbar\nabla - 2e\mathbf{A})\,\psi\right|^2 + \frac{|\mathbf{B}|^2}{2\mu_0}, \tag{2.9}$$

where F_n denotes the normal state free energy, assumed to be constant. The parameters α and β are material and temperature dependent values. $\mathbf{A}$ is the magnetic vector potential, $\mathbf{H}$ (with $\mathbf{B} = \mu_0 \mathbf{H}$) is the magnetic field, which is also

connected to $\mathbf{A}$ as $\mathbf{B} = \nabla \times \mathbf{A}$. The wave function $\Psi(\mathbf{x})$ is the superconducting order parameter, it describes the spatial and temporal dependence of the superconductivity.
For a charge in a magnetic field, its kinetic energy can be described as [42]:

$$< \Psi|F_{\text{kin}}|\Psi > = -\frac{1}{2m}\int \mathrm{d}^3 r \Psi^*(\hbar\nabla + 2ie\mathbf{A})^2\psi = \frac{1}{2m}\int \mathrm{d}^3 r|(\hbar\nabla + 2ie\mathbf{A})\psi|^2. \tag{2.10}$$

After integration of the last segment, a similar expression as the third part of equation (2.9) is obtained. Thus it can be found that the third part of equation (2.9) is the kinetic part. Considering the static state without an external magnetic field, equation (2.9) can be written as [42]:

$$F = \alpha|\Psi|^2 + \frac{\beta}{2}|\Psi|^4. \tag{2.11}$$

The solution of the equilibrium state can be achieved when F is minimal. The values of the wave function at the equilibrium state are obtained as follows:

$$|\Psi|_{\text{eq}} = \begin{cases} \sqrt{-\frac{\beta}{\alpha}}, & \alpha < 0, \\ 0, & \alpha > 0. \end{cases} \tag{2.12}$$

The transition between superconducting and normal state was empirically known to be of second-order in zero magnetic field. For a second-order transition which lowers the temperature, it can be assumed that α and β are smooth functions of T near T_{c}. In the region near T_{c}, by taking the leading terms in the Taylor series in this region, the expression can be written as

$$\begin{aligned} \alpha(T) &= a(T - T_{\text{c}}) + O((T - T_{\text{c}})^2), \\ \beta(T) &= b + O(T - T_{\text{c}}). \end{aligned} \tag{2.13}$$

Analogous to liquid helium, where $|\Psi|^2$ is known to represent superfluid density, the probability of the wave function is $|\Psi(\mathbf{x})|^{\mathbf{2}} = n_{\text{s}}(\mathbf{x})$, where n_{s} is by convention half of the density of the superconducting electrons. Avoiding a divergent solution of $|\Psi|$, the value of β should be a positive constant. The value of α changes from positive to negative, which corresponds to the temperature decreasing from above to below T_{c}. Therefore, the wave function $\Psi(\mathbf{x})$ can be interpreted as the wave function of the Cooper pairs, which pair up and condense into a coherent state below T_{c}. Since the Cooper pairs have zero spin, they are treated as if they were bosons.
To evaluate the minimum of the free energy in the full expression, it is required to calculate all possible states of the superconductor defined by the wave function and the external fields. Since the minimum of the free energy F varies with the value of $\mathbf{A}$, the calculus of variations is used to solve this issue. The

variation with respect to the order parameter can be written as

$$\begin{aligned} F\{\Psi,\Psi^*,\mathbf{A}\} = F_n + \int \delta^3 x \{\alpha|\Psi|^2 + \frac{\beta}{2}|\Psi|^4 \\ + \frac{1}{2m}|(-i\hbar\nabla - 2e\mathbf{A})\Psi|^2 + \frac{(\nabla\times\mathbf{A})^2}{8\pi}\}. \end{aligned} \tag{2.14}$$

Considering a system in the equilibrium state, the minimum of the free energy can be obtained by $\delta F = 0$, this leads to the Ginzburg-Landau (GL) differential equation [7]:

$$\alpha\psi + \beta|\psi|^2\psi + \frac{1}{2m}\left(-i\hbar\nabla - 2e\mathbf{A}\right)^2\psi = 0. \tag{2.15}$$

As it has been discussed before, the third part of the equation (2.14) is the kinetic energy part, it can be written as

$$\begin{aligned} F_{kin} &= \int \delta^3 x \left[\frac{1}{2m}|(-i\hbar\nabla - 2e\mathbf{A})\Psi|^2\right] \\ &= \int \delta^3 x \left[\frac{1}{2m}(-i\hbar\nabla\phi - 2e\mathbf{A})^2|\Psi|^2\right] \equiv \frac{1}{2}mn_{\mathrm{s}}{\mathbf{v_s}}^2, \\ &\text{with } \nabla\phi = \frac{i}{2}\frac{\Psi\nabla\Psi^* - \Psi^*\nabla\Psi}{|\Psi|^2}, \\ &\text{and } \mathbf{v_s} = \frac{1}{m}\left(-i\hbar\nabla - 2e\mathbf{A}\right). \end{aligned} \tag{2.16}$$

Using the basic definition of current $\mathbf{j} = en\mathbf{v}$, the supercurrent can be expressed as

$$\mathbf{j}_{\mathrm{s}} = en_{\mathrm{s}}\mathbf{v_s} = \frac{e|\Psi|^2}{m}\left(-i\hbar\nabla - 2e\mathbf{A}\right). \tag{2.17}$$

In equation (2.15), the electrons that contribute to superconductivity are proposed to form a superfluid, $|\Psi|^2$ indicates the fraction of electrons that have condensed into a superfluid. This can explain the zero resistance given by the GL theory. Equation (2.17) can be used to explain the Meissner effect. By assuming the wave function amplitude being fixed near the equilibrium value, combining the Maxwell-Ampère equation for static conditions ($\nabla\times\vec{B} = \mu_0\vec{j}$), the expression of the field can be described as

$$\begin{aligned} \nabla^2\mathbf{B} &= \mathrm{grad}(\mathrm{div}\,\mathbf{B}) - rot(rot\mathbf{B}) \overset{\mathrm{div}\,\mathbf{B}=0}{=\!=\!=} -\nabla\times(\nabla\times\mathbf{B}) \\ &= \mu_0\nabla\times\mathbf{j}_{\mathrm{s}} = \nabla\times\left(\frac{e|\Psi|^2}{m}(\hbar\nabla\phi - 2e\mathbf{A})\right) \\ &\overset{\nabla^2\phi=0}{=\!=\!=} \frac{\mu_0 e^2 n_{\mathrm{s}}}{m}\nabla\times\mathbf{A} \overset{\nabla\times\mathbf{A}=\mathbf{B}}{=\!=\!=} \frac{\mu_0 e^2 n_{\mathrm{s}}}{m}\mathbf{B} = \frac{1}{\lambda^2}\mathbf{B}, \\ &\text{with } \lambda = \sqrt{\frac{m}{\mu_0 n_{\mathrm{s}} e^2}}, \end{aligned} \tag{2.18}$$

which is the same as the result shown in the London theory (equation (2.8)).

2.2.3 BCS theory

In 1957, Bardeen, Cooper, and Schrieffer proposed the first microscopic theory of superconductivity (the BCS theory). It gave a proper explanation of the superconductivity of conventional superconductors (pure metal and alloys). Furthermore, the BCS theory provided a microscopic interpretation of the GL theory and helped with the development from a phenomenological model to a quantum mechanical model. There are three major insights of the BCS theory:

1. The effective forces between electrons in a solid body can sometimes be attractive rather than repulsive.
2. Two electrons outside of an occupied Fermi surface form a stable paired bound state, this is also called the 'Cooper problem'.
3. Schrieffer constructed a many-particle wave function in which all electrons near the Fermi surface are paired up.

The breakthrough of the BCS theory is that it proposed a model based on the electron pair, which is called 'Cooper pair'. As shown in Fig. 2.3, when an electron passes through a superconductor, it will attract nearby positive charges, leading to a deformation of the lattice. Then a second electron with opposite spin moves to the site with higher positive charge density. It becomes correlated with the former electron. That is how a Cooper pair forms. The deformation of the lattice results in the creation of phonons and provides a set of harmonic quantum oscillators to the system. Thus, the interaction in a Cooper pair is actually the electron-phonon interaction. The interaction of electrons originates from the exchange of phonons. For a normal conductor,

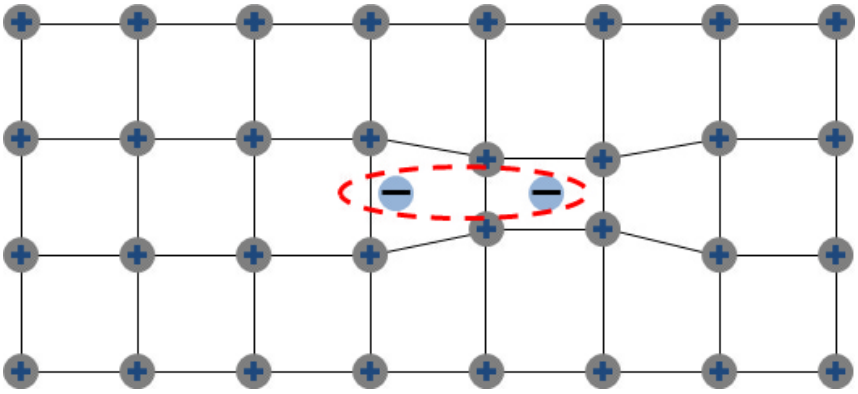

Figure 2.3: Cooper pair in lattice.

the electrons are fermions. However, in superconductors, the electrons in the Cooper pair are with opposite spins, leading to the electron pair being bosonic. According to the Drude model [12], electrical conductivity can be treated in terms of electrons colliding (or scattering) with atoms, electrons, or impurities. In a superconductor, there are numerous Cooper pairs. They overlap with each other and form a macroscopic coherent quantum state similar to a Bose-Einstein condensate. At $T = 0$ K, all 'bosons' are in the ground state. Therefore, they

all behave like one superparticle. No scattering or energy dissipation occurs during the movement of the Cooper pair inside a superconductor.
The 'size' of the Cooper pair is defined as the coherence length ξ (only in the limit of weak-coupling BCS environment, this is the characteristic exponent of the variations of the density of superconducting components). ξ can be derived from the first GL equation (2.15) in the absence of an external field, it describes the scale, in which the wave amplitude varies in space. Therefore, the equation (2.15) needs to be rearranged to [8]

$$\Psi + \frac{\beta}{|\alpha|}\Psi n_\mathrm{s} + \frac{\hbar^2}{2m|\alpha|}\nabla^2\Psi = 0, \tag{2.19}$$

here the fraction $\hbar^2/2m|\alpha|$ is the coherence length ξ. It decribes the size of thermodynamic fluctuations in the superconducting phase and ξ depends on temperature, with $\xi(T) = \xi(0)/\sqrt{1 - T/T_\mathrm{c}}$.
Such coherence among the Cooper pairs increases the energy barrier of the system. In order to break the superconducting state, the energy has to overcome the energy gap created by this barrier. The BCS theory proposed that this energy gap relates to the T_c, as $\Delta E = 1.76 k_\mathrm{B} T_\mathrm{c}$, where k_B is the Boltzmann constant.
Most of the elemental superconductors cannot be penetrated by a magnetic field until the external field reaches the critical value H_c, these superconductors are defined as Type I superconductors. In another type of superconductor magnetic vortices are formed, when the external magnetic field reaches a critical value $H_{\mathrm{c}1}$. The magnetic field is 'trapped' inside these vortices. The superconductor can be pinned in space above a magnet, this phenomenon is called 'flux pinning' and the superconductor, then, is in the state called 'vortex state'. When the external field reaches a higher critical value $H_{\mathrm{c}2}$, the 'vortex state' breaks and the superconductor converts to the normal state. This type of superconductor is called Type II superconductor. A criterion for the classification of Type I and Type II superconductors was proposed by Landau with the definition $\kappa = \lambda/\xi$. It is called the GL parameter, and the classification can be expressed as follows [7]:

$$\begin{cases} 0 < \kappa < \frac{1}{\sqrt{2}}, & \text{Type I superconductor,} \\ \kappa > \frac{1}{\sqrt{2}}, & \text{Type II superconductor.} \end{cases} \tag{2.20}$$

Type II superconductors are usually made of metal alloys or complex oxide ceramics. All high-temperature superconductors are Type II superconductors.

2.3 Josephson junctions

The Josephson junction is a connection of two superconductors separated by a thin non-superconducting barrier. The barrier can be an insulator, a metal or even just a physical constriction which weakens the superconductivity at

the contact interface. The requirement for the barrier is that it can block a normal conducting electron from passing through the interface while permitting electron tunneling between the two superconductors. Thus, the barrier should be sufficiently thin. This idea was proposed by B. D. Josephson in 1962. The Josephson junction has an abundance of macroscopic quantum mechanical properties, meanwhile, it inspires numerous potential applications. Furthermore, it can be applied to a microscopic system rather than simply being a macroscopic model.
In order to describe the properties of the Josephson junction, a simplified derivation of the equations for Josephson tunneling was given by Feynman in his famous lectures. Considering a system as shown in Fig. 2.4, Ψ_1 and Ψ_2 are

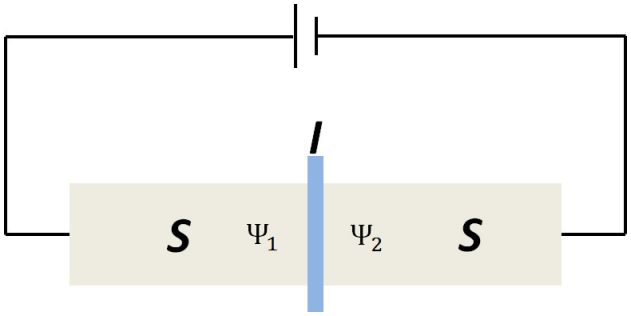

Figure 2.4: Schematic drawing of a Josephson junction consisting of two superconductors marked with 'S' and an insulator marked with 'I'.

defined as the quantum mechanical wave function of the superconducting state in the left and the right superconductor, respectively. The dynamics of the two wave functions are then determined by coupled Schrödinger equations [43]:

$$\begin{aligned} i\hbar\frac{\partial\Psi_1}{\partial t} &= \mu_1\psi_1 + K\Psi_2, \\ i\hbar\frac{\partial\Psi_2}{\partial t} &= \mu_2\psi_2 + K\Psi_1, \end{aligned} \tag{2.21}$$

where K is a coupling constant representing the interaction strength of the two superconductors across the barrier, μ_1, μ_1 are the lowest energy state of the two superconductors. Considering that the solution of the Schrödinger equation can always be written as an exponential expression, and according to GL theory, $|\Psi|^2 = n_\mathrm{s}$, an ansatz of two wave functions can be given as [43]:

$$\Psi_1 = \sqrt{n_1}e^{i\theta_1}, \qquad \Psi_2 = \sqrt{n_2}e^{i\theta_2}, \tag{2.22}$$

where n_1, n_2 are the densities of Cooper pairs from two sides and θ_1, θ_1 are their corresponding phases. Substituted by equation (2.22), equation (2.21) can

be expressed as

$$\begin{aligned} \hbar\frac{\partial n_1}{\partial t} = -\hbar\frac{\partial n_2}{\partial t} = 2K\sqrt{n_1 n_2}sin(\theta_2 - \theta_1), \\ -\hbar\frac{\partial}{\partial t}(\theta_2 - \theta_1) = \mu_2 - \mu_1. \end{aligned} \tag{2.23}$$

The current is a charge transportation, here it can be treated as the time derivative of the density of Cooper pairs, so $I = \partial n_s/\partial t$. If a voltage V is applied between the junction, the energy levels will shift according to $\mu_2 - \mu_1 = 2eV$. By defining $I_0 = 2K\sqrt{n_1 n_2}/\hbar$ and $\delta = \theta_1 - \theta_2$, the Josephson equations can be presented as follows:

$$I = I_0 \sin\delta, \tag{2.24}$$

$$\frac{\partial\delta}{\partial t} = 2e\frac{V}{\hbar}. \tag{2.25}$$

From equation (2.24) and (2.25), it is clear that a DC current can be drawn through the junction without any voltage drop as long as the current is not above I_0. For a Josephson junction with similar types of superconductors on both sides, I_0 is the I_c of the superconductor. If the DC current is larger than I_0, the current can be written as

$$I = I_0 \sin\left(2e\frac{V_0}{\hbar}t\right). \tag{2.26}$$

Here V_0 is the applied voltage. As it can be seen from equation (2.26), the Josephson current will oscillate at a frequency $f = 2eV_0/h$, and $2e/h = 483.6$ GHz/mV. Therefore, the Josephson junction performs capacitive and resistive properties. A resistively and capacitively shunted junction model (RCSJ model) is proposed to describe these features, as shown in Fig. 2.5.

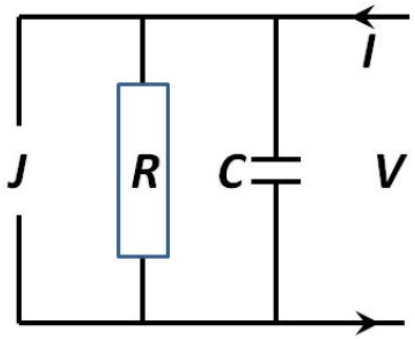

Figure 2.5: Equivalent circuit of a Josephson junction.

The current can be rewritten as an expression as follows [44]:

$$I = I_0 \sin\delta + C\frac{dV}{dt} + \frac{V}{R}. \tag{2.27}$$

Substituting the V by δ from equation (2.25), the current can be expressed as

$$I = I_0 \sin\delta + \frac{\hbar C}{2e}\frac{d^2\delta}{dt^2} + \frac{\hbar}{2eR}\frac{d\delta}{dt}. \tag{2.28}$$

Defining the dimensionless variables as

$$\begin{aligned} \tau &= 2\pi f_c t = \frac{2e}{\hbar} I_0 R t, \\ \beta_c &= 2\pi f_c RC = \frac{2e}{\hbar} I_0 R^2 C, \end{aligned} \tag{2.29}$$

then the current expression can be written as [44]

$$I = I_0 \sin\delta + \beta_c \frac{d^2\delta}{d\tau^2} + \frac{d\delta}{d\tau}. \tag{2.30}$$

The parameter β_c is called the Stewart-McCumber parameter. Generally equation (2.30) is unsolvable. However, if the capacitance can be neglected, $\beta_c = 0$, the $I - V$ behavior can be obtained by integrating equation (2.30) and taking the time average of V. This results in the solutions of V as follows [45]:

$$V = \begin{cases} 0, & \text{for } |I| < I_0, \\ I_0 R\sqrt{\left(\frac{I}{I_0}\right)^2 - 1}, & \text{for } |I| > I_0. \end{cases} \tag{2.31}$$

Further analyzing equation (2.30) it can be found out that as long as $\beta_c < 1$, the $I - V$ behavior is similar to expression (2.31). When $\beta_c > 1$, the junction can be described as a hysteresis.
According to equation (2.25), when the external field changes, the variation of the magnetic flux passing through the Josephson junction leads to a phase change of the superconductor, such variation directly becomes apparent in voltage oscillations. Counting the oscillations allows the evaluation of the flux change. This is why Josephson junctions can be applied to high accuracy magnetometers. The superconducting quantum interference device (SQUID) is the most well-known application of Josephson junctions.

2.4 Phase slips

For a superconducting wire connected with normal leads, there should be no voltage or potential difference between the two connected ends. According to the idea of Josephson, the relative phase ϕ_{12} of the two ends retains constant. To compensate the Johnson noise of the normal current, the supercurrent keeps fluctuating. Thus, actually ϕ_{12} fluctuates around a constant mean value. The zero DC resistivity property in the superconducting state should be interpreted as the meaning that the voltage has no measurable average value proportional to the applied DC current. When an external fluctuation appears, a self-

modification from the supercurrent fluctuation occurs to restore the equilibrium state of the system. For a bulk superconductor, such a modification induces no measurable dissipation. However, for a system with a dimensional limit, for example, a 1D superconductor, the fluctuation of supercurrent after modification cannot be completely average out, leading to a variation of ϕ_{12}. According to the Josephson equation [44], a non-zero resistance is induced to the system below T_c. This is the basic mechanism of phase slips.
Assuming the diameter of the superconducting wire is smaller than the coherence length, the variation of the wave function of the system Ψ will be confined in one direction, then Ψ is a 1D wave function of the coordinate x, along the axis of the wire. Based on the GL theory, the wave function of the 1D superconductor can be written as

$$\Psi(x) = |\Psi(x)|e^{i\phi(x)}. \tag{2.32}$$

For a supercurrent flowing at zero voltage, the solution of the wave function Ψ has a form $\psi_0 e^{iqx}$, where q is the charge of the applied current. The shape of this wave function can be presented by a helix with pitch $2\pi/q$ and radius ψ_0, as shown in Fig. 2.6a.

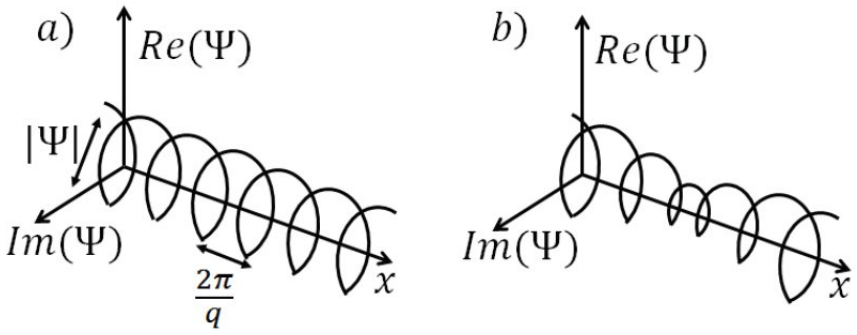

Figure 2.6: Diagram of the wave function in a 1D superconductor. a) before phase slip; b) single phase slip appears at the saddle position along the axis of the superconducting wire.

When a voltage appears, according to the Josephson equation (2.25), the relative phase ϕ_{12} will increase by time. To become consistent with a steady-state, compensation in the phase is necessary. The phase steadily shrinks from one end of the wire until somewhere, where $|\Psi| = 0$, while the other end is fixed. This can be visualized in Fig. 2.6b. This process is called 'phase slip'. If V is constant, ϕ_{12} increases steadily at the rate of $2eV/\hbar$ but instantaneously snaps back by 2π when a phase slip occurs.
The first study of this phenomenon was made by Little [13, 20, 29] in 1967, who attributed the gradual drop in resistance around T_c to the occurrence of thermodynamic fluctuations of the order parameters in the nanowire. The fluctuations appear with an Arrhenius-type activation with a possibility of $e^{-F(\Psi)}/k_B T$. Here F is the free energy of the system. A quantitative perspective of phase slips was proposed by Langer and Ambegaokar [15], which is well-known as the LA theory. Further improvement was made by McCumber and

Halperin [16] resulting in the LAMH theory. By definition the GL free energy remains constant with respect to small changes in Ψ at the saddle point in the barrier shown in Fig. 2.6b. Thus Ψ should satisfy the usual GL equations which were derived variationally by setting $\delta F = 0$. According to the LAMH theory, the free energy increment at the saddle point is given by

$$\triangle F_0 = \frac{8\sqrt{2}}{3}\frac{H_c^2}{8\pi}A\xi, \tag{2.33}$$

where A is the cross-section area of the wire and ξ is the coherence length. In the LAMH theory, one important aspect is the definition of anti-phase slips (APS), naming the process where the phase winds up. Then a net slippage rate is defined as $\Gamma_{\text{net}} = \Gamma_{\text{PS}} - \Gamma_{\text{APS}}$, representing the number of effectively appearing phase slips with a change of phase of $2\pi\Gamma_{\text{net}}$. The total average phase difference can then be defined by the equation

$$\frac{d\langle\delta\varphi\rangle}{dt} = \frac{2eV}{\hbar} + 2\pi\Gamma_{\text{net}}, \tag{2.34}$$

which is equal to zero for the dynamic equilibrium with a constant phase difference over time. Then the equilibrium condition can be obtained as

$$2\pi\Gamma_{\text{net}} = -\frac{2eV}{\hbar}. \tag{2.35}$$

The different slippage rates arise from the free energy difference δF in the energy barrier for the phase jumps in two opposite directions and this difference stems from the electrical work $\int IVdt$. For a phase slip of 2π, the energy difference can be written as [30]

$$\delta F = \triangle F_+ - \triangle F_- = \frac{\pi\hbar}{e}I. \tag{2.36}$$

A frequency Ω is introduced to describe the phase slip behavior with a free energy and an energy barrier. The mean net phase slip rate is expressed as

$$\begin{aligned}\frac{d\psi_{12}}{dt} &= \Omega\left[\exp\left(-\frac{\triangle F_0 - \delta F/2}{k_{\text{B}}T}\right) - \exp\left(-\frac{\triangle F_0 + \delta F/2}{k_{\text{B}}T}\right)\right] \\ &= 2\Omega e^{-\triangle F_0/k_{\text{B}}T}\sinh\frac{\delta F}{2k_{\text{B}}T}.\end{aligned} \tag{2.37}$$

By substituting equation (2.37) with (2.36) for δF and combining the voltage description in equation (2.25), the voltage can be expressed as

$$V = \frac{\hbar\Omega}{e}e^{-\delta F_0/k_{\text{B}}T}\sinh\frac{\pi\hbar I}{2ek_{\text{B}}T}. \tag{2.38}$$

The value of Ω should be proportional to the length of the wire since the phase

slip is expected to be able to occur independently at any site along the wire. Therefore, the voltage drop is proportional to the length of the wire for a given current, to ensure the resistance is variable. It was first proposed by Langer and Ambegaokar, with a rather arbitrary expression as nAL/τ, where τ is the electronic relaxation time in the normal state and n is the electron density. A more precise expression was derived by McCumber and Halperin by using the time-dependent GL theory. They found a temperature dependent form of Ω [16]:

$$\Omega = \frac{\sqrt{3}}{2\pi^{3/2}} \frac{L}{\xi(T)} \left(\frac{\triangle F_0}{k_\mathrm{B} T} \right)^{\frac{1}{2}} \frac{1}{\tau_s}, \tag{2.39}$$

where $1/\tau_s = 8k_\mathrm{B}(T_\mathrm{c} - T)/\pi\hbar$ is the characteristic relaxation rate of the superconductor in the time-dependent GL theory. $L/\xi(T)$ is the number of nonoverlapping locations in which the fluctuations might occur.
In the condition of zero bias $V = 0$, an equilibrium is achieved. If $\Gamma_\mathrm{PS} = \Gamma_\mathrm{APS}$ due to the same energy barriers for their activation, then the Arrhenius activation produces only TAPS with zero supercurrent by average. Then the slippage rate proposed by Little can be written as [29]

$$\Gamma_\mathrm{TAPS} = \Omega \exp\left(-\frac{\triangle F(T)}{k_\mathrm{B} T} \right). \tag{2.40}$$

By the hypothesis of a small bias current, equation (2.38) can be simplified by the expression from equation (2.40):

$$V = I \left(\frac{\pi^2 \hbar^2}{e^2 k_\mathrm{B} T} \right) \Omega \exp\left(-\frac{\triangle F}{k_\mathrm{B} T} \right) = I \left(\frac{\pi^2 \hbar^2}{e^2 k_\mathrm{B} T} \right) \Gamma_{TAPS}. \tag{2.41}$$

Applying Ohm's law as a consequence of the time average values of current and voltage, the phase slip resistance of a superconducting nanowire can be expressed as

$$R_\mathrm{LAMH} = \sqrt{\frac{3}{\pi}} \frac{1}{\tau} \frac{L}{\xi(T)} \sqrt{\frac{\triangle F}{k_\mathrm{B} T}} \left(\frac{\pi \hbar^2}{2e^2 k_\mathrm{B} T} \right) \exp\left(-\frac{\triangle F}{k_\mathrm{B} T} \right). \tag{2.42}$$

The LAMH theory does not take normal electrons into account. Tinkham proposed that the phase slip resistance R_LAMH and the normal resistance R_n behave as being shunted together, therefore the measurable resistance with thermal phase slips becomes [18]

$$R_\mathrm{total} = \left(\frac{1}{R_\mathrm{n}} + \frac{1}{R_\mathrm{LAMH}} \right)^{-1}. \tag{2.43}$$

Any model involving only thermally activated processes would inevitably give a $R(T)$ dependence that R drops faster and faster as T is lowered. These models could not fit the data of thinner wires. As it can be seen in equation

(2.42), when $T/T_c < 0.3$, R_{LAMH} becomes unmeasurably small. The QPS provides another possible source of resistance below T_c. The first idea of a non-zero resistance from quantum fluctuation was reported in 1970 [17]. During decades of investigation, it was proposed that the mechanism for such phase slippage is known as macroscopic quantum tunneling (MQT) [31]. Then the experimental evidence and the first phenomenal model was given by Giordano. Since there is no quantitative theory of macroscopic quantum tunneling for 1D superconductors, Giordano used a similar model, the motion of a damped particle moving in a tilted washboard potential. Assuming that the particle can be treated as a simple harmonic oscillator in a well, with a small oscillation frequency ω_0, the tunneling rate can be written as [32]

$$\Gamma_{\mathrm{MQT}} = B\sqrt{\frac{V_0\omega_0}{\hbar}}\exp\left(-\frac{aV_0}{\hbar\omega_0}\right), \tag{2.44}$$

where B and a are non-unit constants and V_0 is the barrier height, which can be identified with the free energy barrier ΔF in the LAMH theory. Since τ_{GL} is the only time scale in the time-dependent GL theory, it is natural to identify ω_0 with τ_{GL}, then equation (2.44) can be expressed as

$$\Gamma_{\mathrm{MQT}} = B\sqrt{\frac{\Delta F}{\hbar\tau_{\mathrm{GL}}}}\exp\left(-\frac{a\Delta F\tau_{\mathrm{GL}}}{\hbar}\right). \tag{2.45}$$

Following a similar procedure as the former one, obtaining the resistance from the phase slip rate and inserting the factor L/ξ, an expression of the resistance induced by MQT can be written as

$$R_{\mathrm{MQT}} = B\frac{L}{\xi}R_{\mathrm{q}}\sqrt{\frac{\Delta F}{\hbar\tau_{\mathrm{GL}}}}\exp\left(-\frac{a\Delta F\tau_{\mathrm{GL}}}{\hbar}\right). \tag{2.46}$$

The expression above can be obtained by replacing $k_{\mathrm{B}}T$ with $\hbar\tau_{\mathrm{GL}}$ from equation (2.42). This implies that after a quantum modification, the LAMH theory is still valid to QPS. Eventually, the resistance induced by QPS is expressed as

$$R_{\mathrm{QPS}} = b_{\mathrm{G}}\sqrt{\frac{3}{\pi}}\frac{L}{\tau_{\mathrm{r}}}\frac{1}{\xi(T)}\sqrt{\frac{\Delta F\tau_{\mathrm{r}}}{\hbar}}\left(\frac{\pi\hbar^2}{2e^2k_{\mathrm{B}}T}\right)\exp\left(-\frac{\Delta F\tau_{\mathrm{r}}}{\hbar}\right), \tag{2.47}$$

where b_{G} is a prefactor for the uncertainty of the phase slippage event frequency estimation. Considering all the possible resistances induced by phase slip, the total resistance can be expressed as

$$\frac{1}{R_{\mathrm{total}}} = \left(\frac{1}{R_{\mathrm{n}}} + \frac{1}{R_{\mathrm{TAPS}} + R_{\mathrm{QPS}}}\right). \tag{2.48}$$

Experimentally the TAPS was discovered on a tin whisker with a diameter of $\sim 5\,\mu\mathrm{m}$ [18], while the QPS was found in the ultra-thin MoGe alloy fiber with

a diameter of less than 10 nm. It can be predicted that a non-zero resistance below T_c will be induced to the electric behavior of the nanowire system due to the TAPS. Because the average diameter of the nanowires is around 300 nm. The discussion above does not take the grain boundaries or lattice defects into account. For the polycrystalline Type II superconductors, the grain boundaries and the lattice defects can serve as 'pinning centers'. When the free energy of a superconducting material in the mixed state is considered as an energy landscape, the pinning centers produce sites with lower energy, where the flux lines locate inside the material. It can be seen as a washboard potential, where the favorable states are isolated by areas with an activation energy of the magnitude of the pinning potential U. The thermal activation of flux lines is theorized in the model of Anderson and Kim, where thermal energy promotes the motion of flux lines from site to site, similarly to the thermal activation of phase slips. The rate of this flux line oscillation is given by the expression [34]

$$\Gamma = \Omega_0 \exp\left(-\frac{U}{k_B T}\right), \tag{2.49}$$

where Ω_0 is the oscillation frequency of the flux lines inside the average pinning potential and U is the pinning potential. This means that flux creeps take place in the temperature regions, where the pinning energy is in the order of $k_B T$. When an electrical current is applied to the superconductor, the potential is tilted and the activation energy changes to lower values in one direction. This results in a preferred direction for the movement of flux lines, which produces a measurable resistance for the 1D superconductor as well. The resistance is non-zero due to the dissipative mechanism.

2.5 Critical state model (CSM) and extended critical state model (ECSM)

It has been well known that Type II superconductors exhibit significant differences from Type I superconductor in their magnetic properties. If the external magnetic field is increased, Type II superconductors convert from a state where the entire external field is expelled at the surface, to a mixed state, where the magnetic field is pinned in the vortices within the superconductor. Such vortices are called Abrikosov vortices [46]. When the external magnetic field increases beyond the second critical value, the whole superconducting state is completely broken. Thus, the Type II superconductor has two critical magnetic fields H_{c1} and H_{c2}. Some important superconducting parameters, e. g. J_c, can be estimated via the analysis of the magnetic properties of Type II superconductors.
Bean proposed a model describing the magnetic behavior of the ideal Type II superconductor [47]. Considering a cylindrically shaped superconductor with a radius R experiencing an increasing magnetic field parallel to the cylinder axis,

then currents which counteract the change in the external field are induced in the sample. When the field H is lower than H_{c1}, the currents are constricted at the sample surface. As the field increases above H_{c1}, the induced currents diffuse to the interior of the sample, reaching a critical state. According to Ampere's law, in an external magnetic field H, the currents flow to a depth $\Delta = 10(H - H_{c1})/4\pi J_c$. Then the internal field H_i of the sample can be expressed as follows [47]:

$$H_i = \begin{cases} 0, & 0 \leqslant r \leqslant R[1 - (H - H_{c1})/H^*], \\ H - H^*(1 - r/R), & R[1 - (H - H_{c1})/H^* \leqslant r \leqslant R, \end{cases} \tag{2.50}$$

where $H^* = 4\pi J_c R/10$. When $H > H^* + H_{c1}$, the superconducting state is broken. And the magnetization of the sample in the external field H can be summarized as

$$4\pi M = \begin{cases} -H, & 0 \leqslant H \leqslant H_{c1}, \\ -H + \dfrac{(H^2 - H_{c1}^2)}{H^*} + \dfrac{H_{c1}^2(3H - 2H_{c1}) - H^3}{3H^{*2}}, & H_{c1} \leqslant H \leqslant H^* + H_{c1}, \\ -H^*/3, & H \geqslant H^* + H_{c1}. \end{cases} \tag{2.51}$$

This was the first model describing the magnetization of the superconductor depending on the macroscopic dimension of the sample. Since it relates to the critical state of the superconductor, it is called the Bean model or critical state model (CSM). Based on this model, Freiz and Webb derived the relationship between the magnetization and critical current density. They proposed that a cylindrical Type II superconductor in a uniform external field H_a parallel to its cylinder axis should show uniform magnetic induction [49]

$$B(H_a) = H_a + 4\pi M_e(H_a), \tag{2.52}$$

where M_e is the equilibrium magnetization of the sample. However, the induction is generally not uniform due to the existence of flux pinning. If B can be specified for all values of the applied field H_a within the surface, then the induction B is an irreversible but well-defined function of the magnetic history. Using $B_0 = H_a + 4\pi M_e(H_a)$ as the boundary condition, the critical state is defined by $J_c(B,T)$, and its value can be obtained by varying B_0 over a suitable range. Considering a hysteresis magnetization loop, there are always two critical currents $J_+(B_+)$ and $J_-(B_-)$ on the positive and negative branches, respectively. The current density at position r can be described in a Taylor series

$$J_\pm(r) = J_\pm(R) + J'_\pm(R)(r - R) + J''_\pm(R)\frac{(r - R)^2}{2!} + ... \tag{2.53}$$

The induction $B(r)$ can be expressed as $B(r) = kJ(r)$ in Gauss units, where

$k = 4\pi/10$. Then, the Taylor series expression can be written as

$$B_{\pm}(r) = B_0 + k[J_{\pm}(R)(r-R) + J'_{\pm}(R)\frac{(r-R)^2}{2!} + ... \tag{2.54}$$

For the magnetic moment, the average magnetization $\bar{M}$ is obtained by performing the integration

$$4\pi\bar{M} = \frac{1}{\pi R^2}\int_0^{2\pi} \mathrm{d}\theta \int_0^{2\pi} [B(r) - H_\mathrm{a}] r \mathrm{d}r, \tag{2.55}$$

with the boundary condition $B_0 = H_\mathrm{a} + 4\pi M_\mathrm{e}(H_\mathrm{a})$, the magnetization can be expressed as a Taylor series

$$4\pi\bar{M}_{\pm} = 4\pi M_\mathrm{e} + 2k\left(\frac{J_{\pm}R}{3!} - \frac{J'_{\pm}R}{4!} + \frac{J''_{\pm}R}{5!} - ...\right), \tag{2.56}$$

The critical state model assumes a relationship between the magnitude of the critical current density and the local field, hence when $r = R$,

$$|J_\mathrm{c}(B)| = |J_+(B)| = |J_-(B)|, \tag{2.57}$$

$$\partial^n J_+/\partial r^n = (-1)^n \partial^n J_-/\partial r^n. \tag{2.58}$$

By calculating the difference and the sum of $\bar{M}_+$ and $\bar{M}_-$, two expressions can be obtained:

$$4\pi(\bar{M}_+ - \bar{M}_-) = \frac{2kJ_+R}{3} + \frac{4kJ''_+R^3}{5!} + ..., \tag{2.59}$$

and

$$4\pi(\bar{M}_+ + \bar{M}_-) = 2(4\pi M_\mathrm{e}) - \frac{kJ_+R^2}{3!} + ..., \tag{2.60}$$

In the regions, where the series converges rapidly, an approximation can be applied to the results above

$$4\pi(\bar{M}_+ - \bar{M}_-) = \frac{2}{3}kJ_\mathrm{c}R, \tag{2.61}$$

$$4\pi(\bar{M}_+ + \bar{M}_-) = 2(4\pi M_\mathrm{e}). \tag{2.62}$$

The most popular used Bean equation can be obtained from equation (2.61)

$$J_\mathrm{c} = 30(\bar{M}_+ - \bar{M}_-)/2R. \tag{2.63}$$

For the rectangle shaped sample, if the field is perpendicular to a plane with a width a and a length b ($a \leqslant b$), a geometric factor G is applied, then the expression of critical current density becomes

$$J_{\mathrm{c,Bean}} = G\Delta M/a, \tag{2.64}$$

where $\Delta M = |\bar{M}_+ - \bar{M}_-|$ and $G = 3b/(3b - a)$.
The critical state model provides a conventional indirect method of J_c estimation via the measurement of hysteretic dependencies of magnetization. However, for many superconducting materials, magnetization loops have a pronounced axial asymmetry with respect to the H axis ($M = 0$), which is beyond the consideration of this symmetric model. The asymmetry of the dependence $M(H)$ increases with rising temperature. For high-temperature superconductors, the asymmetry of magnetization loops can manifest itself after an increase of temperature up to ∼10–30 K [50, 51, 53]. Taking the asymmetric factors into account, an extended model is required.
The critical state model manages to describe symmetric $M(H)$ dependencies in high magnetic fields. It includes several points as follows [54]:

1. The material consists of numerous cylindrical granules. The magnetization loop is described by the expression as follows:

$$M(H) = -H + (1 - P)\mu_n H + \frac{2}{\mu_0 R_0^2}\int_0^{\infty}\phi(R)\int_0^{R} rB(r)\mathrm{d}r\mathrm{d}R, \quad (2.65)$$

   where P is the fraction of the material concentrated in the superconducting granules, μ_n is the magnetic permeability of the intergranular material, $\phi(R)$ is the distribution density of the superconducting granules while $B(r)$ is the magnetic induction in the sample. For a homogeneous sample, equation (2.65) is restated with $P = 0$ and $R_0 = R$. For an infinitely long cylindrical sample with radius R, which is coaxial to the external magnetic field, the magnetization is determined by the following expression:

$$M(H) = -H + \frac{2}{\mu_0 R_0^2}\int_0^{R} rB(r)\mathrm{d}r. \quad (2.66)$$

2. According to Ampere's circuital law:

$$\frac{\mathrm{d}B(r)}{\mathrm{d}r} = \pm\mu_0 j_c(B). \quad (2.67)$$

   Following the idea from Forsthuber [56], a nondecreasing function is induced here:

$$\Phi(B) = \int_0^{B}\frac{j_{c0}}{j_c(B')}\mathrm{d}B', \quad (2.68)$$

   here j_{c0} is the critical current density at $H = 0$. In the deviation expression, it can be found out that $\mathrm{d}\Phi(B)/\mathrm{d}B = [j_c(B)/j_{c0}]^{-1}$. Combining equation (2.67) with (2.68), the numerical solution of the critical current density distribution is obtained as

$$\pm\,\mu_0 j_{c0}(R - r) = \Phi(B) - \Phi(\mu_0 H). \quad (2.69)$$

Then the magnetic induction distribution $B(r)$ can be described in three major parts in a whole $M(H)$ hysteresis:

1. Increasing the initial field from 0 to the maximum value H_m, $B(r)$ is determined by equation:

$$\Phi(B) - \Phi(\mu_n H) = -\mu_0 j_{\mathrm{c}0}(R - r). \tag{2.70}$$

2. When the field decreases from H_m to 0, $B(r)$ consists of two branches, which are described by two equations:

$$\begin{aligned} \Phi(B) - \Phi(\mu_n H) &= \mu_0 j_{\mathrm{c}0}(R - r), \\ \Phi(B) - \Phi(\mu_n H_\mathrm{m}) &= -\mu_0 j_{\mathrm{c}0}(R - r). \end{aligned} \tag{2.71}$$

3. From 0 to $-H_\mathrm{m}$, $B(r)$ consists of three parts, which are described by these equations:

$$\begin{aligned} \Phi(-B) - \Phi(-\mu_n H) &= -\mu_0 j_{\mathrm{c}0}(R - r), \\ \Phi(B) + \Phi(-\mu_n H) &= \mu_0 j_{\mathrm{c}0}(R - r), \\ \Phi(B) - \Phi(\mu_n H_\mathrm{m}) &= -\mu_0 j_{\mathrm{c}0}(R - r). \end{aligned} \tag{2.72}$$

The critical state model originated from a macroscopic model which did not take the pinning force distribution $F_\mathrm{p}(r)$ into account. Actually, at higher temperature and external fields, the pinning force is very weak near the granule surface. In the thermal equilibrium model, the vortices are only pinned in the granule core and the magnetization is created by surface supercurrent circulating in the region where vortices are not pinned. This model coincides better with reality than the original critical state model.
Considering the equilibrium magnetization, Gokhfeld [53, 55] proposed an extended critical state model by introducing a new characteristic size parameter l_s. It represents the depth from the surface where the vortices are not pinned. When a cylindrical sample experiences an external field H, the induction distribution can be described as in Fig. 2.7. The magnetization of the sample first leads to the penetration of the surface layer by the magnetic flux (plot AB). Defining $B_s(H)$ as the induction at the depth l_s from the surface, the magnetic flux begins to penetrate the central region as $B_s(H) > 0$ (plot BC). Defining H_p as the field of the complete penetration by the magnetic flux, then $R = \Phi(\mu_0 H_p)/(\mu_0 j_{\mathrm{c}0})$. The magnetic flux reaches the center of the sample when the external field increase to H_p. The induction at the center of the sample increases (point E) until the external field reaches the maximum value of H_m, then it decreases. The frozen flux remains in the center of the sample (plot BDE) and decreases to zero in the field H. As a result, a hysteretic dependence $M(H)$ is observed. When the external field increases from the opposite direction to $-H_\mathrm{m}$, the frozen flux behavior is shown in section CFG. Similar to the description in CSM by equations (2.70)-(2.72), the induction dependence in the central region has different profiles for each branch of the magnetization loop:

1. The branch of the initial magnetization with an increase in the external field from 0 to H_m described in plot BC:

$$\Phi(B) - \Phi(B_s(H)) = -\mu_0 j_{\mathrm{c}0}(R - r - l_\mathrm{s}). \tag{2.73}$$

2. The branch $M^+(H)$ with a decrease in external field from H_m to 0 described in plot BD:

$$\Phi(B) - \Phi(B_s(H)) = \mu_0 j_{\mathrm{c}0}(R - r - l_\mathrm{s}), \tag{2.74}$$

and in plot DE:

$$\Phi(B) - \Phi(B_s(H_\mathrm{m})) = -\mu_0 j_{\mathrm{c}0}(R - r - l_\mathrm{s}). \tag{2.75}$$

3. The branch $M(H)$ with a field decrease from $-H_\mathrm{m}$ to 0 described in plot FG:

$$\Phi(-B) - \Phi(B_s(H_\mathrm{m})) = -\mu_0 j_{\mathrm{c}0}(R - r - l_\mathrm{s}), \tag{2.76}$$

and in plot CF:

$$\Phi(-B) + \Phi(B_s(H)) = \mu_0 j_{\mathrm{c}0}(R - r - l_\mathrm{s}). \tag{2.77}$$

4. The branch $M(H)$ with an increase in H from 0 to H_m after the circulation is described again in plot BC.

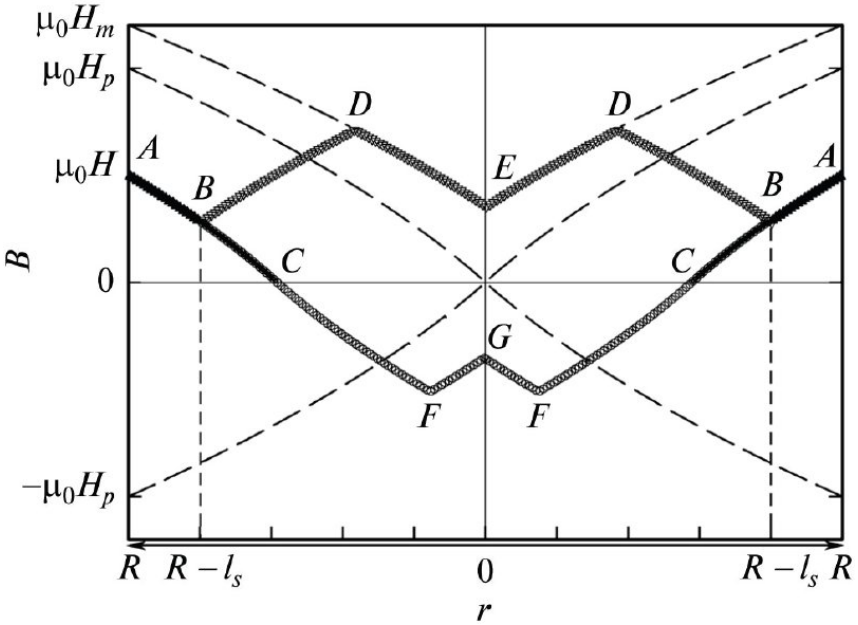

Figure 2.7: Dependence of induction B on r. ABC line shows the penetration of the magnetic flux into the sample, ABDE shows the frozen flux with a decrease in the external field from H_m to H, ABCFG shows the frozen flux with variations in the external field from $-H_\mathrm{m}$ to H [55].

In the former model, the dependence of the critical current density on the magnetic induction has been described in different ways, like in the Bean model (j_c = const) [48], which is only applicable for the symmetric magnetization loop with respect to H axis. The Anderson-Kim relationship ($j_c \sim 1/B$) [34] provides a good description of $M(H)$ dependence for $H \ll H_{c2}$. The exponential dependence proposed by Chen [52] is in good agreement with the magnetization behavior near H_{c2}. Gokhfeld proposed a new dependence which is proportional to $1/B$ in weak fields and decreases exponentially in strong fields:

$$j_c(B) = \frac{j_{c0}}{(|B|/B_1)^\gamma + \exp(|B|/B_2)}, \tag{2.78}$$

here B_1 and B_2 are the parameters which determine the characteristic scales and $\gamma \approx 1$.
According to the definition in equation (2.68), $\Phi(B)$ can be expressed as

$$\Phi(B) = \frac{|B|^{\gamma+1}}{(\gamma+1)B_1} + B_2 \exp\left(\frac{|B|}{B_2}\right) - B_2. \tag{2.79}$$

When $l_s > R$, the dependence of $M(H)$ is reversible. In HTScs, the magnetization loop becomes reversible when the magnetic field H exceeds the irreversibility field H_{irr}, while $H_{irr} \ll H_{c2}$. Gokhfeld proposed a simple expression describing the $l_s(H)$ dependence for HTScs:

$$l_s(H) = l_{s0} + (R - l_{s0})H/H_{irr}, \tag{2.80}$$

where l_{s0} is the value of l_s at $H = 0$. l_s is believed to be about the London penetration depth λ [50]. For simplicity, the surface layer depth l_s is assumed to be equal to λ, thus in the initial state, $l_{s0} \approx \lambda_0$.
Now the distributions of $B(H)$ dependence on magnetization reversal historically are described via equations (2.73) to (2.80). The magnetization loops can be calculated via the integration formula (2.66). For $H = 0$, the width of magnetization loops along the M axis and their asymmetry with respect to the H axis are determined by the parameters $P_w = j_{c0}R$ and $P_a = l_{s0}/R$, respectively. $J_{cm}(H)$ is obtained by replacing B with $\mu_0 H$ in equation (2.78) and by choosing the fitting parameters for the experimental data. For symmetric loops, $J_{cm}(H)$ dependence obtained from equation (2.78) corresponds to the one obtained from formula (2.63) (cylindrical model) or (2.64) (rectangular model) in the critical state model. For an asymmetric magnetization loop, the values of J_{cm} obtained from equation (2.78) are much larger than the values obtained from the critical state model. In this case, the region where the vortices are not pinned cannot be ignored anymore, which means l_s is comparable to R. Furthermore, this region is not involved in the supercurrent transportation. When estimating the average critical current density, the effective cross section for the supercurrent flow should be smaller. Therefore, the effective critical

current density should be expressed as

$$J_{\mathrm{cm}}(H) = j_{\mathrm{c}}(H) S_{\mathrm{kern}}(H)/S. \tag{2.81}$$

Here $j_{\mathrm{c}}(H)$ is obtained via replacing B with $\mu_0 H$ in equation (2.78), S is the cross area of the sample perpendicular to the field, S_{kern} is the area of the central region with pinned vortices. For a sample with regular geometric structure, this expression can be described as following when l_{s} is comparable to R:

$$J_{\mathrm{cm}}(H) = \begin{cases} J_{\mathrm{c}}(H)(1 - l_{\mathrm{s}}(H)/R)^n, & l_{\mathrm{s}} < R, \\ 0, & l_{\mathrm{s}} \geq R, \end{cases} \tag{2.82}$$

here $n = 2$ for a cylindrical sample and $n = 1$ for a thin plate. Taking the equilibrium magnetization of the surface layer into account, this ECSM has an advantage in solving different types of asymmetric magnetization dependences on the external field. Especially for polycrystalline HTScs, in which grain boundaries dominate the sample, the consideration of the effective vortices pinning region becomes significantly necessary.

3 Experimental setups

This chapter describes the experimental setups which are used for the preparation and characterization of the samples. Section 3.1 introduces the electrospinning instrument used for the fabrication of the nanowires; section 3.2 introduces the cryostat which provides the low temperature and magnetic field environment for the electric measurements; section 3.3 demonstrates the sample holder used for fixing the nanowire sample during the electric measurement.

3.1 Electrospinning instrument

The electrospinning instrument used in this work is a commercial MECC nanofiber electrospinner. It can provide voltages in the range from 0.5 kV to 30 kV. The syringe can move horizontally with a traverse speed up to 300 mm/s. The distance between the needle and the collector is adjustable from 50 to 150 mm. The microspeed boost pump can push the syringe with velocities from 0.1 to 60 ml/hr. The rectangle collection area is well-grounded, and it can be replaced by a collection drum with a rotation speed up to 3000 rpm.
The main advantage of the instrument is that it can provide a relatively sealed environment for the electrospinning process with the relative humidity being lower than 60 %, which is important for the standard electrospinning process.

3.2 Cryostat

The electric measurements were carried out in a cryostat from Oxford Instruments (OI). It can provide a magnetic field up to 10 T parallel to the cylinder axis of the cryostat and a maximum field of 12 T via cooling the superconducting magnet coil to 2.2 K with liquid helium just above its Lambda point. The cryostat consists of a helium chamber, a sample chamber and two chambers to isolate the helium chamber from the sample chamber and from the outer environment respectively. The helium chamber is connected to the sample chamber via a needle valve, and a rotary pump is connected to the sample chamber, providing the necessary vacuum ($\leq$ 20 mbar) for drawing the helium from the helium chamber via the needle valve.
The magnet coil is made of superconducting Nb_3Sn, with a T_c of 18.3 K. During operation, the magnetic coil should be activated when its temperature is around 4.2 K to ensure that the Nb_3Sn is superconducting. Similar to other magnetic coils, the applied field decays at the edge of the coil. This used Nb_3Sn coil

has a regime of over 10 cm along the coil axis where the applied field has a uniform distribution. Such a regime is sufficiently large to provide an uniform and stable magnetic field to the whole sample during the electric measurement. In the sample chamber, there is a thermally insulated interstitial space around the sample holder position, called variable temperature insert (VTI). It is controlled by the outer intelligent temperature controller (ITC), through which it is possible to control the temperature of the sample chamber continuously in the range from 3.5 K to 300 K, accompanied by helium cooling. Therefore the electric measurement can be performed in a temperature range from 3.5 K to 300 K.

3.3 Sample holder

The sample was fixed on printed circuit boards (PCBs) which were designed for the system at the University of Lorraine in Nancy. The PCBs enable us to exchange samples and reuse the device. As shown in Fig. 3.1 (a), the PCB has an area of 18 × 18 mm^2 with a 10 × 10 mm^2 square regime in the middle for sample fixing. There are in total 16 holes for electrode pins with 35 µm Cu and Au plating, which are added as conducting connections. Figures. 3.1b and 3.1c demonstrate the nanowire network and single fiber sample fixed on the PCB with a four-probe connection, respectively.

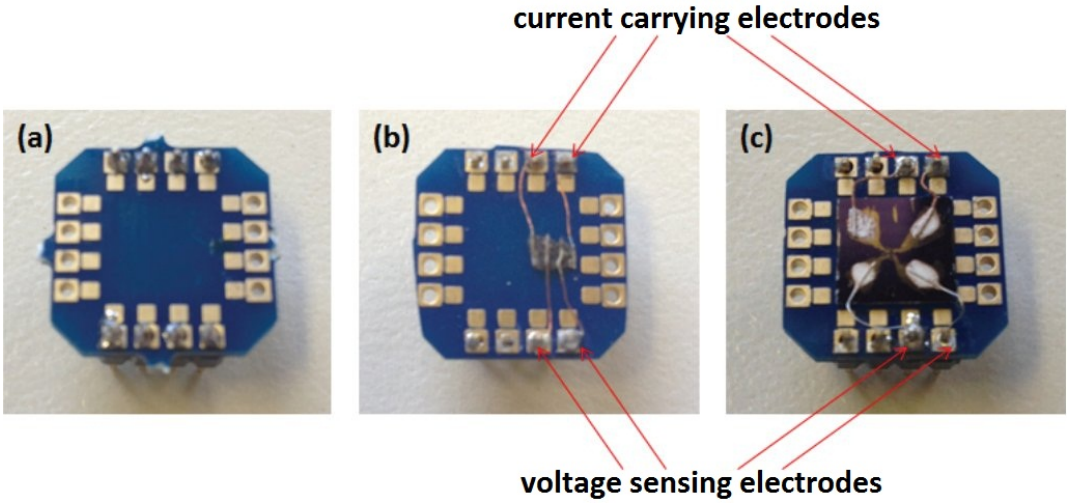

Figure 3.1: (a) Empty PCB holder with electrode pins; (b) Nanowire network sample fixed on a PCB with four-probe connections; (c) Single fiber sample fixed on a PCB with four-probe connections, the fiber is directly connected with the Au electrode pattern, then connected to the copper electrode wires with silver paint. The current carrying and voltage sensing electrodes for four-probe connection have been marked by red arrows.

The sample on the PCB was placed in a cylindrical holder with a temperature sensor and wires for the electrical transportation measurement. This cylindrical holder is made from Macor^{TM}. The material of the main body is sintered glass

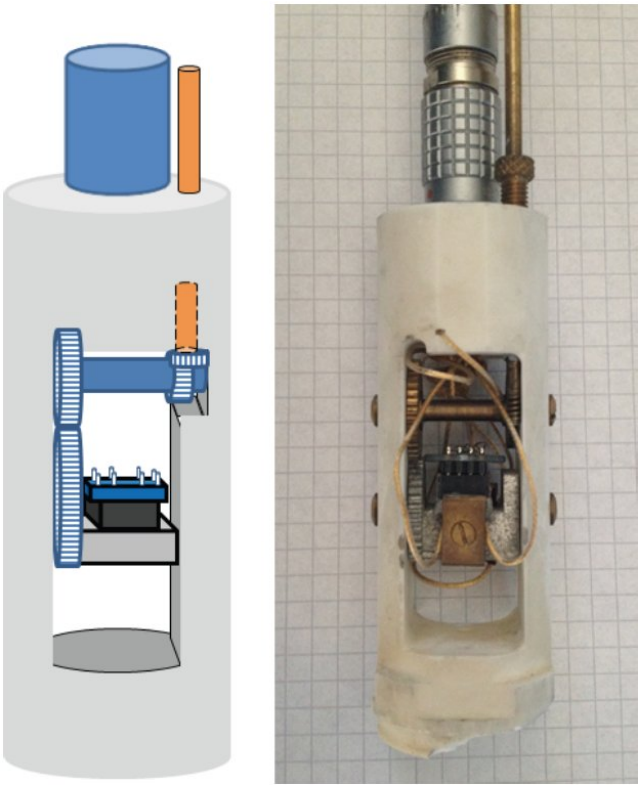

Figure 3.2: Sample holder fixed inside the cryostat. The left image is the designed model and the right image is the real sample holder.

ceramic consisting of mica distributed in a borosilicate matrix. This material provides the holder with a low heat conductivity, a low thermal expansion coefficient, and high electrically insulating properties. The holder for the PCB is connected to an outer rod via a gear connection system shown in Fig. 3.2. With this design, the sample holder can rotate up to 90° via rotating the outer rod. With this setup, angular resolved magnetic field measurements can be performed. The temperature sensor is attached to the bottom of the PCB holder. Since the sample is also attached to the PCB on top, it is expected that the temperature sensor rapidly responses to the variations in temperature surrounding the sample.
The wiring inside the cylinder holder is equipped with five coaxial and two triaxial cables (LEMO, no. 017820 and Oxford Instruments, no.PAB0001). The triaxial cables are used for the supply of the current carrying electrodes in the four-probe setup. They allow low current flowing into the sample without loss in the form of transverse currents to the shielding layer between the grounding line and the signal line. The coaxial cables are used for the connections of the voltage sensing electrodes and for temperature sensing. They are insulated with PTFE (Teflon).

4 Sample preparation

The samples in this work include two types of materials: cuprate HTScs and La-based manganite CMR materials. The samples are synthesized from sol-gel precursors, which are mixtures of large molecular weight polymer and acetates solution. The fiber structure is fabricated by electrospinning and the organic component is removed via thermal treatment in the box furnace in ambient conditions. For the HTSc samples, additional thermal treatment in the pure oxygen is applied to compensate for the previous oxygen loss.
All the fibers are fabricated electrospinning method. The electrospinning instrument allows tuning the environment in such a way that humidity and temperature can be kept constant during operation. Thus the quality of the samples is stable. Table 4.1 shows the basic parameters used in the electrospinning process.

Parameter	
Applied voltage (kV)	20-26
Flying distance (mm)	190
Pump rate (mL h^{-1})	0.1-0.2
Travel speed (mm s^{-1})	50
Travel distance (mm)	100
Temperature (°C)	22-28
Relative humidity (%)	30-45

Table 4.1: Electrospinning parameters for fiber fabrication.

The obtained electrospun fibers form an organic fiber network. After thermal treatment, the fibers form the expected inorganic phases, the diameter of the fibers decreases, as a result of the removal of organic components and the network structure maintains. This result indicates that the conventional electrospinning method provides samples with a nanowire network structure.
In the following sections, details about the sol-gel precursors of different samples are given. Special designs for the fiber structure and the alignment modification are also introduced. At the end of this chapter, a discussion on the phase formation and the thermal treatment is presented.

4.1 Electrospinning precursors

For the precursor of the LSCO nanofibers, lanthanum acetate (purity 99.99 %), strontium acetate (purity 99.99 %), and copper acetate (purity 99.95 %)

powders were weighed according to a molar ratio of 1.85 : 0.15 : 1 respectively and dissolved in deionized water. Then the polymer was slowly added to the acetate solution with a mass ratio of 2.5 : 1.5. The chosen polymer is polyvinyl alcohol 17-88 (PVA), which means that the polymerization degree is 1700∼1800, and the alcoholysis degree is 88-89 %. Thus the average molecular weight of PVA 1788 is 44.05 × 1750 = 77088. In order to dissolve PVA, the mixture was stirred at 80 °C for 2 hours, then naturally cooled down and then stirred again at room temperature for 15 hours.
For the CMR materials $La_{1-x}Sr_xMnO_4$ nanofibers, the precursors are similar to the one above, only the copper acetate was replaced by manganese(II) acetate (purity 99.999 %).
For the precursor of the Bi-2212 nanowires, bismuth acetate (purity of 99.999 %), strontium acetate hydrate (purity of 99.99 %), calcium acetate hydrate (purity of 99.9965 %) and copper acetate monohydrate (purity of 99.99 %) powders were weighed with a molar ratio of Bi : Sr : Ca : Cu = 1 : 1 : 1 : 2 (this precursor is called 1112 precursor, and the sample synthesized from this precursor is named non-doped Bi-2212 sample hereafter) and dissolved in propionic acid (bismuth acetate does not dissolve in water). The excess of calcium and copper acetates serve to suppress the impurity formation according to the reaction $Bi_2Sr_2CaCu_2O_8 \rightarrow Bi_2Sr_2CuO_6 + CaCuO_2$ during the thermal treatment [57].
For the sample with a Li-containing precursor, the overall ratio of the target elements is Bi : Sr : Ca : Li : Cu = 2 : 2 : 2 : 1.2 : 2.8. The ratio between Li and Cu is 0.3 : 0.7 corresponding to the Li doping level of 30 %, and the excess of Ca and Cu is applied to suppress the formation of $Bi_2Sr_2CuO_6$ (Bi-2201) with the same reason as mentioned above.
For the Pb-doped sample, Pb acetate trihydrate (ACS purity) was added. The acetate molar ratio was adjusted to Bi : Pb : Sr : Ca : Cu = 1.9 : 0.1 : 2 : 1 : 2 (this precursor is called Pb-doped precursor, the sample synthesized from this precursor is named Pb-doped Bi-2212 sample). This means 5 % of Bi is replaced by Pb. The addition of Pb contributes to the formation of the Bi-2212

	Acetates (g)			Polymer (g)
A	$La(Ac)_3 \bullet 1.5H_2O$	$Sr(Ac)_2 \bullet xH_20$	$Cu(Ac)_2 \bullet H_2O$	
	1.1004	0.0535	0.3461	
B	$La(Ac)_3 \bullet 1.5H_2O$	$Sr(Ac)_2 \bullet xH_20$	$Mn(Ac)_3 \bullet 4H_2O$	
	0.7342	0.1101	0.6557	PVA
C	$La(Ac)_3 \bullet 1.5H_2O$	$Sr(Ac)_2 \bullet xH_20$	$Mn(Ac)_3 \bullet 4H_2O$	2.5
	0.6586	0.1693	0.6722	
D	$La(Ac)_3 \bullet 1.5H_2O$	$Sr(Ac)_2 \bullet xH_20$	$Mn(Ac)_3 \bullet 4H_2O$	
	0.5790	0.2315	0.6895	

Table 4.2: Precursor recipes of La-based samples: A) $La_{1.85}Sr_{0.15}CuO_4$; B) $La_{0.8}Sr_{0.2}MnO_3$; C) $La_{0.7}Sr_{0.3}MnO_3$; D) $La_{0.6}Sr_{0.4}MnO_3$.

	Dopant	Acetates (g)				Polymer (g)
A	-	Bi*	Sr*	Ca*	Cu*	
	-	0.4386	0.2337	0.1797	0.4536	
B	Pb*	Bi*	Sr*	Ca*	Cu*	PVP
	0.0292	0.5657	0.1586	0.2439	0.3079	1.0444
C	Li*	Bi*	Sr*	Ca*	Cu*	
	0.0483	0.4715	0.2512	0.1931	0.3413	

Table 4.3: Precursor recipes of BSCCO samples: A) non-doped Bi-2212; B) Pb-doped Bi-2212; C) Li-doped Bi-2212. Here Pb*, Li*, Bi*, Sr*, Ca* and Cu* represent the corresponding acetates $Pb(Ac)_2 \bullet 4H_2O$, $Li(Ac) \bullet xH_2O$, $Bi(Ac)_3$, $Sr(Ac)_2 \bullet xH_20$, $Ca(Ac)_2 \bullet xH_2O$, $Cu(Ac)_2 \bullet H_2O$, respectively.

phase according to references [58, 59], no excess of Ca and Cu are applied in this case.
Variation of the solvent made it necessary to change the polymer from PVA to polyvinylpyrrolidone (M.W. 1,300,000) (PVP). The PVP was mixed into the solutions to enhance the viscosity of the precursor with a mass ratio of PVP : acetates = 4 : 5. All the chemical compounds were completely dissolved by stirring at room temperature for 15 hours.
Tables 4.2 and 4.3 present the summary of the recipes of all samples.

4.2 Nanoribbons

In chapter 2, it has been mentioned that with a certain condition, it is possible to fabricate nanoribbons via electrospinning. According to the equation (2.6), the electrospinning jet intents to form a hollow tube structure during the rapid evaporation under the following conditions:

1. high diffusivity of the solvent;
2. steep concentration gradient along the surface of the jet to the center;
3. low concentration-dependent mobility of the polymer.

With the help of outer atmospheric pressure and residual charge redistribution, the tube collapses and forms a ribbon.
Experimentally, with higher solution concentration, the solution will be less mobile. Thus, the diffusive activity ratio is higher than the advective activity. As a result, the diffusivity of the solvent from 'skin' to air is higher, leading to a steep concentration gradient from the jet surface to the center. Therefore, it is possible to tailor the electrospinning fiber structure by simply controlling the concentration of the precursor.
Shivkumar et al. investigated electrospinning fibers of PVA with various polymer molecular weights and solution concentrations [60], they reported a mapping on the morphological regimes of the electrospinning PVA as shown in Fig. 4.1. According to their result, for the electrospinning fiber of pure PVA with molecular weight about 77,000 g/mol, when the solution concentration is

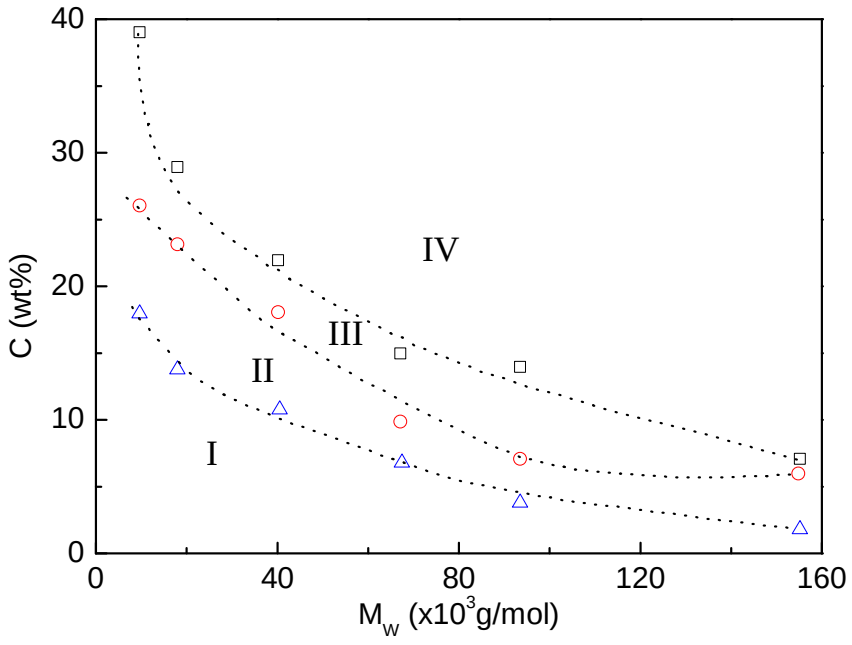

Figure 4.1: Regimes for various morphologies observed in the electrospun polymer. I: Beads, II: beaded fibers, III: complete fibers and IV: flat fibers. The symbols and the accompanying lines correspond to the transition point from one structure to the other.

above 14.6 wt%, the system starts to form flat fibers. In other words, ribbons are formed.
In this work, one of the topics is the comparison of the superconductivity between LSCO nanowires and nanoribbons. Three types of precursors with different concentrations were prepared. They are shown in table 4.4:

Type	Acetates (g)	PVA (g)	Water (ml)	Concentration (wt %)
A			5	44.4
B	1.5	2.5	8	33.3
C			12.5	24.2

Table 4.4: Composition of the type A, B, and C samples employed for the study of structure distribution.

Via a scanning electron microscope (SEM) observation as shown in Fig. 4.2, LSCO nanowires and nanoribbons can be found in samples with relatively low and high concentrations, respectively.
However, even when the sample is dominated by nanoribbons, nanowires are still mixed into the network. For further investigation, a structure distribution of those different types of precursors was carried out, the nanowire and nanoribbon areas were mapped.
Since the widths of the nanoribbons are much larger than the diameters of the

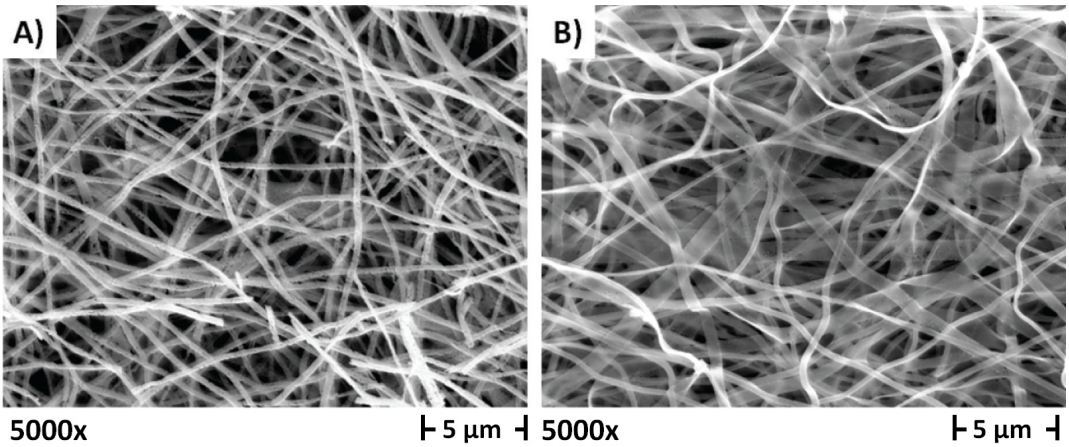

Figure 4.2: SEM images of the LSCO fibers: A) nanowire dominated; B) nanoribbon dominated.

nanowires, it is straightforward to distinguish these two structures and to create statistical data of their spatial distribution. These results are presented in Fig. 4.3. The upper row presents the data of the nanowires, while the lower row gives that of the nanoribbons. From Fig. 4.3, two regularities can be deduced:

1. The quantity of nanoribbons increases with a higher sol-gel precursor concentration corresponding to the theoretical prediction [40] and the

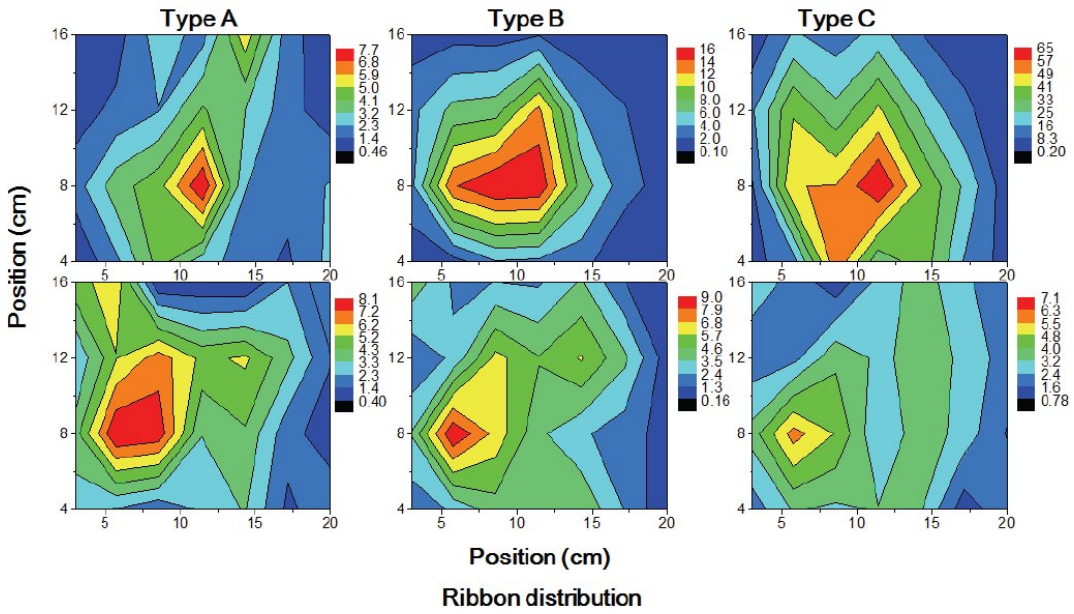

Figure 4.3: Spatial distribution of the nanowire/nanoribbon, obtained from a thorough analysis of a variety of SEM images. The upper row shows the spatial distribution of the nanowires in the collection area for the three types of samples (A, B and C, see table 4.4), while the lower row of graphs gives the distribution of the nanoribbons.

experimental result of the PVA electrospinning fibers [60]. However, all the concentrations of the precursor here are higher than the estimated value from Shivkumar for pure PVA (the lowest concentration from type C precursor is 24.2 wt%, still higher than the estimated value of 14.6 wt%). One possible explanation is that with the addition of acetates, the entanglement molecular weight of the precursor is higher than it is for the pure PVA, therefore the ribbon only appears at higher concentrations.

2. The nanowires are mainly located close to the center of the collection area, while the nanoribbons are found at the outer perimeter. This result matches the assumption from above that in order to form the nanoribbon structure, the area at the outer perimeter of the collection area with weaker electric field supplies sufficient time for the formation of nanoribbons as compared to the high field region around the projection area of the needle.

In order to prepare a pure ribbon sample, one may consider a further increase of the precursor concentration. However, this idea is limited by the viscosity of the precursor constriction of electrospinning. When the viscosity of the precursor is too high, the required voltage of the jet formation becomes dramatically high. For the present instrument, the maximum applied voltage is 30 kV. In this case, the concentration of type A precursor, 44.4 wt% is nearly the highest value which can be achieved. In the following experiments, the ribbon sample is based on the type A precursor presented in table 4.4.

4.3 Parallel nanowires

In order to investigate the electric properties of the nanowire samples, the straightforward approach is applying a four-probe measurement on a single nanowire. Another approach is applying a measurement on parallel nanowires, as the parallel nanowires system can be viewed as a shunt circuit, the electric behavior is similar to a single nanowire.

In the conventional electrospinning process, the electrospun nanowire is randomly aligned on a collector due to electric instability. To prepare the parallel nanowires, one of the possible approaches is using a spinning collector. The spinning direction is perpendicular to the spinneret, in other words, perpendicular to the direction of the initial jet. When the fiber forming from the jet begins to locate at the collector, the adhesive force drives the fiber to accumulate along the rotation direction of the collector. When the rotation speed is fast enough, the spinning collector can effectively collect the fibers in uniform alignment, which results in parallel fibers.

Considering the formation of the fiber, the precursor is charged when it comes out of the spinneret, transforming to a cone shape as the Coulomb force overcomes the surface tension. The charge attached to the jet redistributes all over the surface when the jet elongates to a fiber. It is obvious that the fiber is charged before locating onto the collector, the charge density on its surface decreases when the fiber elongates. If the electric field between the spinneret

and the collector is not uniform, the alignment of the fiber can be controlled by the electric field force. Such an idea is reported by Xia and Li [61]. By using a collector with a split by a void gap (with the width of the split ranging from millimeter to centimeter scale), the electric field is redistributed as shown in Fig. 4.4a, and the charged fiber is driven to align between the gap by the electric field force (Fig. 4.4b).

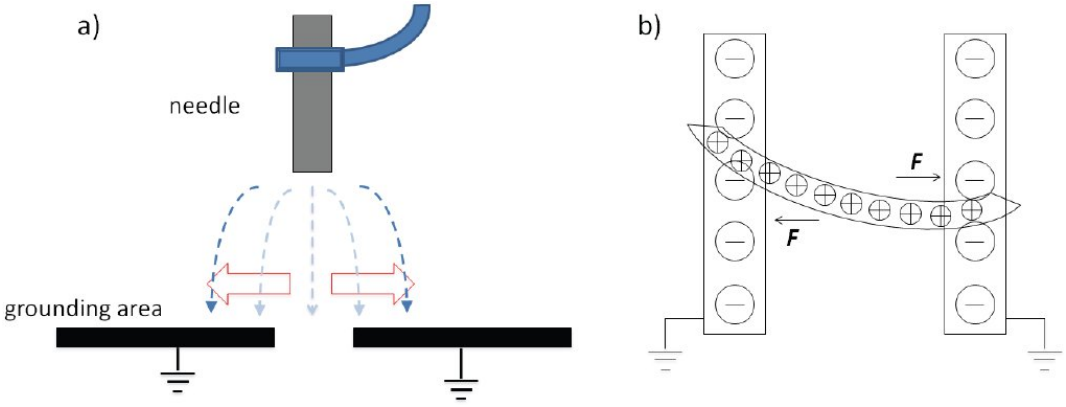

Figure 4.4: Design of the parallel nanowire collector: a) lateral view and b) vertical view of the collection area.

It turns out that a split collector provides much higher efficiency in the collection of parallel nanowires.
The next step is investigating if the parallel nanowires can survive after the high temperature annealing. For the La-based sample, the removal of the organic component and the inorganic phase formation require a final treatment temperature above 600 °C. While for the Bi-2212 nanowires, it requires annealing at 800 °C to obtain the superconducting phase.
An annealing test was applied to the as-prepared Bi-2212 nanowires (synthesized from the type A precursor presented in table 4.3). The fiber was collected on a silicon wafer with 300 nm silicon dioxide on the surface, as pure silicon would react chemically with the sample above 700 °C. Some additional gaps were added to the wafer, with widths of around 600 µm. Then the sample was annealed step by step from room temperature to a maximum of 800 °C. Figure 4.5 demonstrates a collection of fiber on one gap after different annealing steps. Up to 384 °C, there was no obvious change of the nanowires. Almost all the nanowires were spanning over the gap. When the treatment temperature reached 600 °C, parts of the nanowire shrank and fell into the gap, only major nanowires survived. However, as the temperature reached 800 °C, nearly no fiber was left around the gap, which is different compared to the case of the nanowire network. This indicates that the crossover network structure helps to keep the wires from breaking into small pieces.
According to the result, parallel nanowires survive at the annealing up to 600 °C. Similar results occurred for other precursors mentioned in tables 4.2 and 4.3. That means that the idea of fabricating parallel nanowires is only suitable for

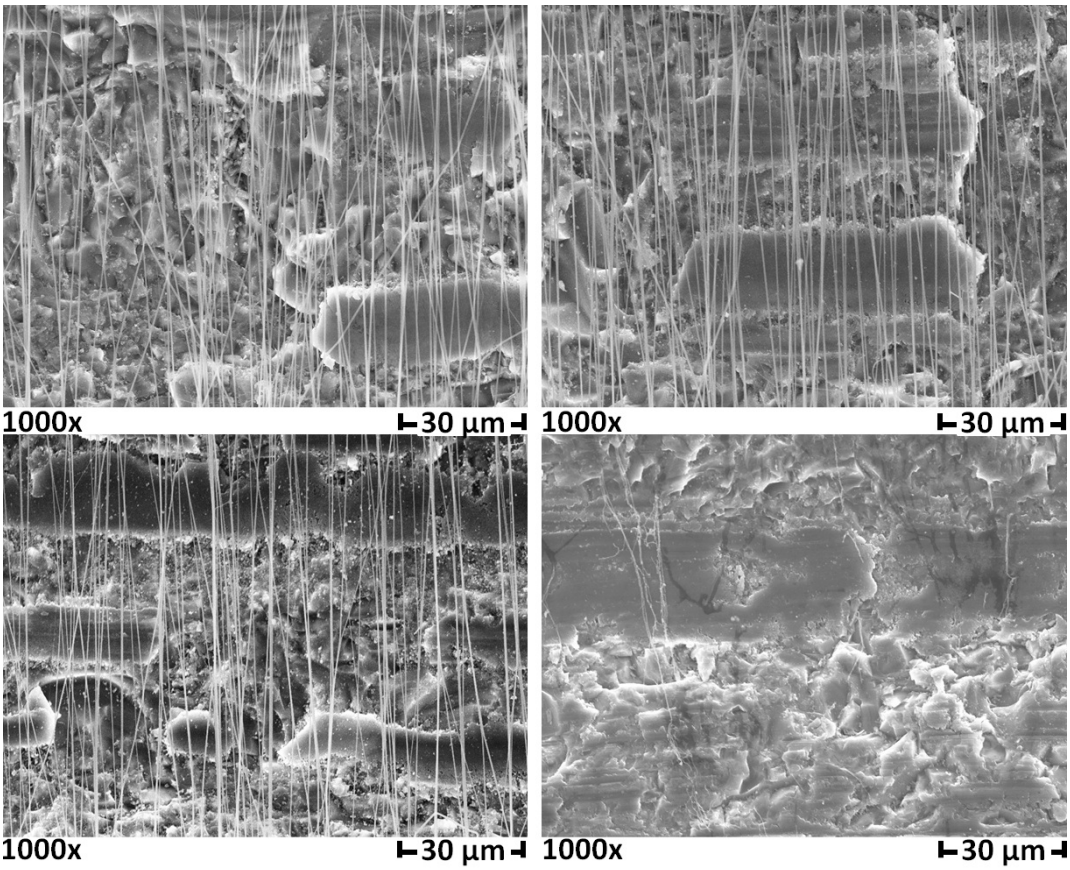

Figure 4.5: Parallel nanowires annealed at different temperatures: A) As-prepared; B) 384 °C 1 hour; C) 600 °C 1 hour; D) 800 °C 1 hour.

the La-based nanofibers, but not the Bi-2212 nanowires, unless the treatment temperature of the Bi-2212 nanowires can be reduced to below 600 °C.

4.4 Single nanowire

The purpose of preparing a single nanowire sample has been mentioned in the previous section. The main task is to transport a single nanowire to the electrode pattern.

A mask of the electrode pattern was prepared via e-beam lithography technique on a silicon wafer (with a 300 nm silicon dioxide layer on the surface). The resist poly(methyl methacrylate) (PMMA) was spin-coated onto the wafer with the recipe given in table 4.5. The first three steps provide sufficient thickness of resist for the target pattern (around 200 nm for each layer, 600 nm in total), the last step, the thin layer of PMMA 950k helps to sharpen the mask structure. During the lithography process, the pattern was written by an electron beam at 10 kV with a dose of 100 µC/cm^2. The pattern consists of four large square electrodes with widths of 300 µm, two tapering lines with widths of 3 µm as current carrying electrodes and two with a width of 1 µm as voltage sensing

Step	Resist	Rotation speed	Baking at	Baking time
1	PMMA 600k	2000 rpm	150 °C	5 min
2	PMMA 600k	2000 rpm	150 °C	5 min
3	PMMA 600k	2000 rpm	150 °C	5 min
4	PMMA 950k	5000 rpm	150 °C	30 min

Table 4.5: Recipe of spin coating on silicon for the use in electron beam lithography.

electrodes. Then it was developed in a mixture of isopropanol and methyl-isobutyl-ketone (MIBK) with a volume ratio of 3 : 1 for 1 min. The resulting sample was used as the mask of the electrode pattern. 10 nm of titanium was sputtered on the mask onto enhance the adhesive force between metal and silicon dioxide, then 300 nm Au was sputtered as a pattern material. After sputtering, the structure was treated in acetone to remove the PMMA mask (lift-off process). Figure 4.6 shows the SEM images of the complete Au electrode pattern.

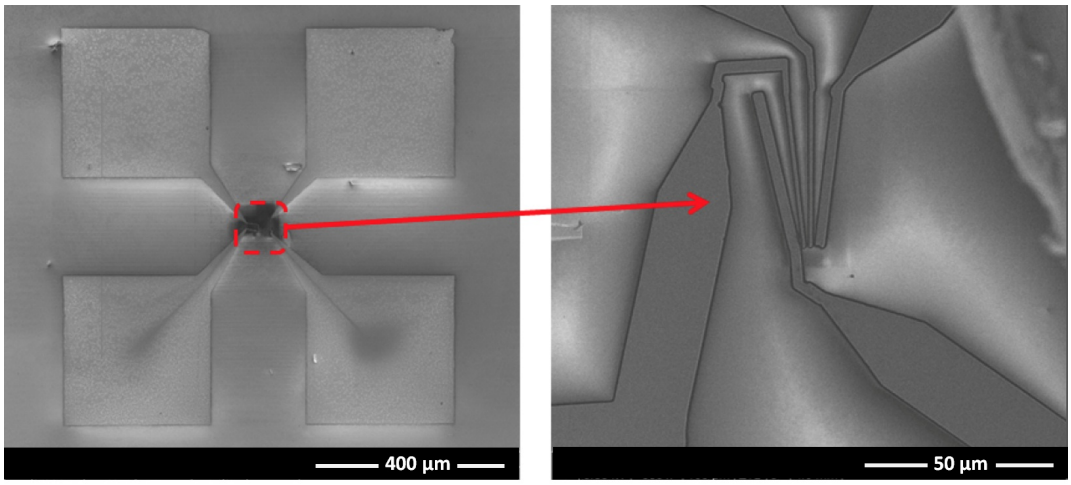

Figure 4.6: Electrode pattern made by e-beam lithography. The right image is the zoom-in view of the center area [115].

The focused ion beam (FIB) technique provides a possibility of transportation of a single nanowire and a method for fixing the nanowire onto the pattern. However, it is nearly impossible to pick a single nanowire directly from the nanowire network. The connections between the individual wires prohibit taking out a nanowire which is long enough for the measurement setup.
The parallel nanowire sample is a good option for nanowire transportation, because there is no connection between the nanowires. As mentioned earlier in section 4.3, only La-based nanowires could be synthesized parallelly. For this reason, another approach to extract a single nanowire from a network was developed. By controlling the electrospinning time, a layered network sample with controllable thickness can be produced. Furthermore, with a certain

thickness, the sample shrinks and curves after annealing. The edge of the sample tilts up, providing an option for the manipulator to pick up a nanowire from the edge of the sample.
In the electric measurement of the single nanowire sample, the junction resistances between the nanowire and the electrodes play a significant role. If the

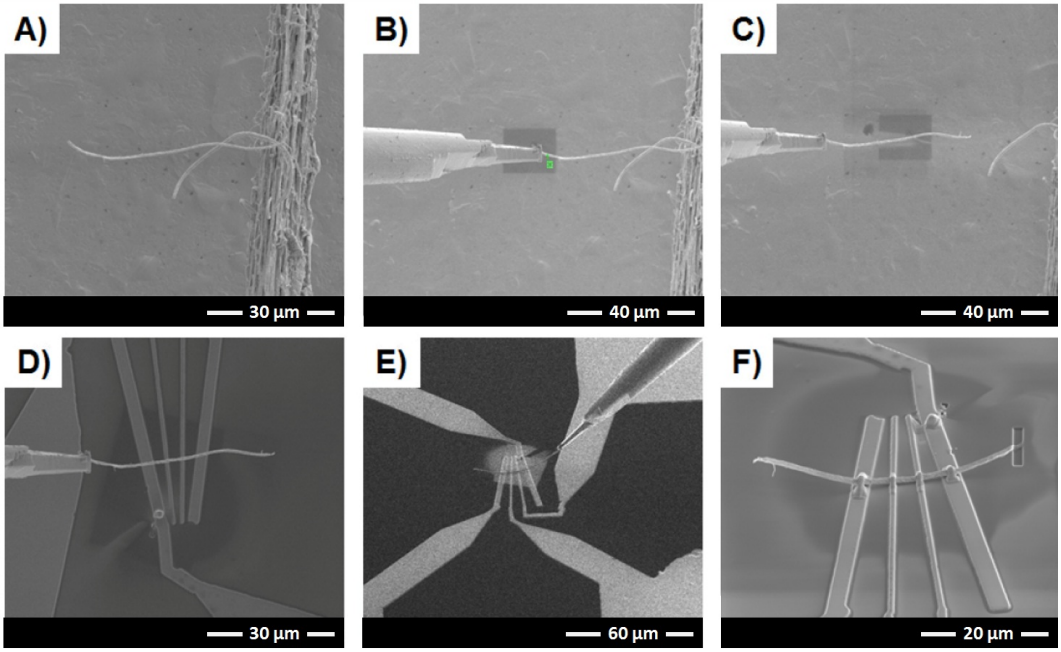

Figure 4.7: Transportation process of a single fiber in FIB: A) Single fiber hanging at the edge of the network; B) Fixing the manipulator and the fiber by platinum deposition; C) Cutting the fiber from the network by silicon cutting mode; D) Approaching the electrode pattern; E) Fixing the fiber by platinum deposition; F) 45° view of the sample [115].

conductivity of the connection between the nanowire and the electrode is not good enough, the semiconducting behavior of the Schottky contact will suppress the electric behavior of the nanowire sample. Therefore, the nanowire sample has to be in full contact with the electrodes instead of connecting the gap by metal deposition. For the deposition mode in FIB, it has to be the electron mode instead of the conventional ion mode. This mode can effectively reduce the influence of the platinum contamination ions in the chamber diffusing to the connection junction. Figure 4.7 demonstrates the whole process of single fiber transportation and connection to the electrode pattern in the FIB.

4.5 Thermal treatment and phase formation

For the removal of the organic component and obtaining the targeted phase of the sample, thermal treatment is indispensable. Meanwhile, in order to avoid an intense chemical reaction ruining the fiber structure, the treatment steps have to be well arranged. Thermal gravity analysis (TGA) and differential

scanning calorimetry (DSC) provide useful hints for the thermal treatment. The thermal treatment processes of the La-based samples (relative low temperature treatment) and the Bi-based samples (high temperature treatment) are described in the following two sections.

4.5.1 Thermal treatment of La-based nanofibers

Figure 4.8 shows the TGA-DSC result of the as-prepared LSCO/PVA fiber, which is fabricated with the type A precursor listed in table 4.2.

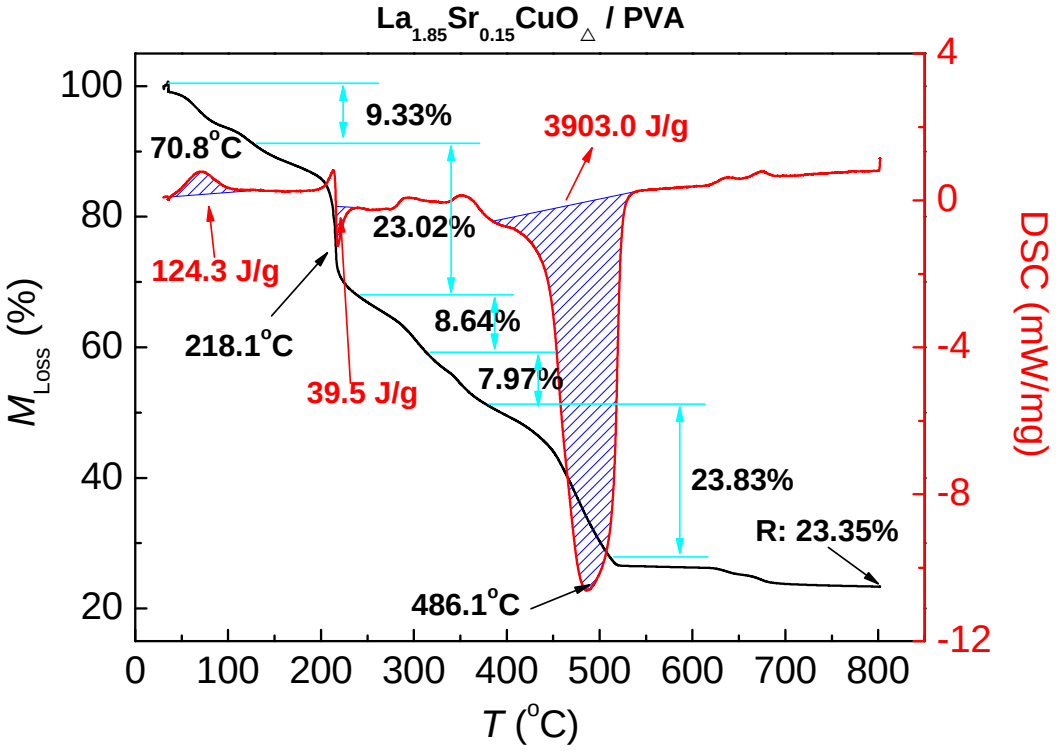

Figure 4.8: TGA-DSC measurement of the LSCO/PVA as-prepared fiber.

According to the result, three obvious reactions occur at 70.8 °C, 218.1 °C and 486.1 °C. Here is a brief analysis of what happens at these temperatures: The average molecular weight of PVA 1788 has been mentioned to be 77088 g/mol in section 4.1, combined with the information in table 4.2 (type A precursor), the molar quantities of the acetates can be calculated as follows:

$$\begin{aligned} M(\text{Acetates}) &= \frac{W(Cu(Ac)_2 \cdot H_2O}{M_w(Cu(Ac)_2 \cdot H_2O)} \\ &= \frac{0.3461\,g}{199.64\,g/mol} \approx 1.7336 \times 10^{-3}\,mol, \end{aligned} \tag{4.1}$$

The value of x from $\mathrm{Sr(Ac)_2 \cdot xH_2O}$ can be deduced as follows:

$$\begin{aligned} x &= \frac{x \times W_w(H_2O)}{M_w(H_2O)} = \frac{M_w(Sr(Ac)_2 \cdot xH_2O) - M_w(Sr) - M_w(Ac) \times 2}{M_w(H_2O)} \\ &= \frac{205.71 - 87.62 - 59.04 \times 2}{18.01} \approx 0, \end{aligned} \tag{4.2}$$

The molar quantities of the crystallized water can be deduced from the molar quantities of acetates and the element ratio between acetates and water:

$$\begin{aligned} M(H_2O_{cyrstal}) &= M(Acetates) \times (M(H_2O)_{La(Ac)_3 \cdot 1.5H_2O} + x \times M(H_2O)_{Sr(Ac)_2 \cdot xH_2O}) \\ &= 1.7336 \times 10^{-3} \times (1.5 \times 1.85 + x \times 0.15 + 1)\, mol \\ &\overset{x=0}{=\!=} 6.5443 \times 10^{-3}\, mol. \end{aligned} \tag{4.3}$$

With the percentage of mass loss from the TGA data, the mass loss ratio around the temperatures of the three peaks can be estimated as follows:

$$\begin{aligned} &\mathrm{Massloss(Peak1) : Massloss(Peak2 + Peak3)} \\ &= 9.33 : [(23.02)_{\mathrm{Peak2}} + (8.64 + 7.97 + 23.83)_{\mathrm{Peak3}}] \approx 1 : 6.8. \end{aligned} \tag{4.4}$$

While the weight ratio between the crystallized water and the acetates can be calculated as follows:

$$\begin{aligned} W(H_2O) : W(Ac) &= M(H_2O_{crystal}) \times M_w(H_2O_{crystal}) : M(Ac) \times M_w(Ac) \\ &= 6.5443 \times 10^{-3} \times 18.01 : 13.6087 \times 10^{-3} \times 59.04 \\ &\approx 1 : 6.82. \end{aligned} \tag{4.5}$$

The ratio between mass loss at the first peak and the summarized mass loss of the second and the third peaks is similar to the mass loss ratio between the crystallized water and the ions of acetates. This means that the reaction around the temperature of the first peak is the removal of the crystallized water, while the process at the second and third peaks have a strong relationship with the decomposition of the ions of acetates, accompanied with the decomposition and evaporation of the organic component.

The purpose of TGA-DSC measurement is to decide the thermal treatment temperatures. The fiber structure may be destroyed after too many dramatic reactions. Therefore, not more than one obvious reaction (removal of crystallized water is not included here) occurring in each step of thermal treatment would be helpful to maintain the fiber structure. Based on the analysis above, the as-prepared LSCO/PVA fibers were treated in three-step thermal treatment, at the temperatures 218 °C, 486 °C and 700 °C for 1 hour respectively. The final temperature step is chosen at 700 °C, because in the TGA data, there is no obvious mass variation after 700 °C. This indicates that the removal of organic components ends at this temperature.

A similar analysis was applied to the $\mathrm{La_{1-x}Sr_xMnO_3}$ as-prepared samples.

Figure 4.9 shows the TGA-DSC measurement of the $La_{0.8}Sr_{0.2}MnO_3$/PVA as-prepared fiber.

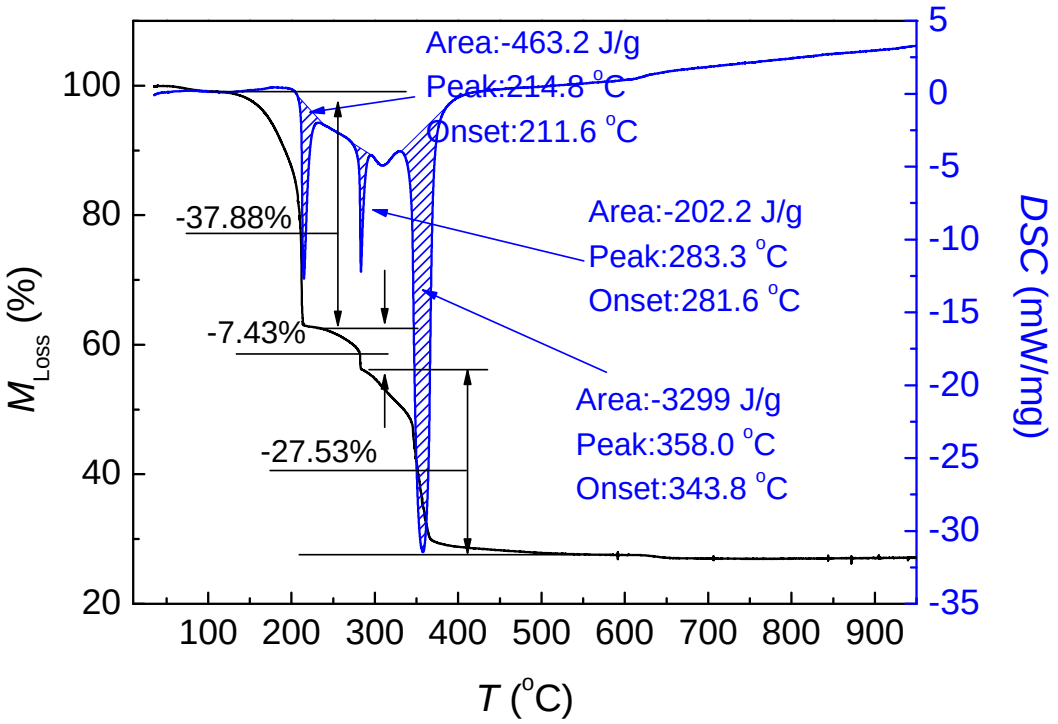

Figure 4.9: TGA-DSC measurement of the $La_{0.8}Sr_{0.2}MnO_3$/PVA as-prepared fiber.

Analogically, the treatment temperatures of the $La_{0.8}Sr_{0.2}MnO_3$/PVA as-prepared fibers were chosen to be the peak temperatures of the DSC curves shown in Fig. 4.9. The sample was annealed at 212 °C, 282 °C, and 344 °C for 1 hour, respectively. Eventually, the sample was annealed at 650 °C for 1 hour to ensure the removal of all organic components.

4.5.2 Thermal treatment of the $Bi_2Sr_2CaCu_2O_8$ nanowires

For the BiSrCaCuO (BSCCO) samples, the purpose of thermal treatment is not only the removal of all organic components but also the formation of the superconducting phase. The BSCCO system has abundant phases forming at different temperatures. For bulk materials, the Bi-2212 phase is obtained when the materials are melted above 825 °C. On the other hand, except for some special materials like carbon fiber, most of the electrospun nanowire cannot survive at such a high temperature. Thus conquering the opposition between targeted phase formation at a higher temperature and maintaining the fiber structure at a lower temperature is the main challenge of annealing Bi-2212 samples.

The first problem of the formation of Bi-2201 impurities has been solved by two approaches: 1. applying additional Cu and Ca elements; 2. Pb doping. Both

approaches ensure that the sample forms the Bi-2212 phase after annealing the sample at 800 °C. This has been confirmed by X-ray diffraction (XRD) measurement as shown in Fig. 4.10.

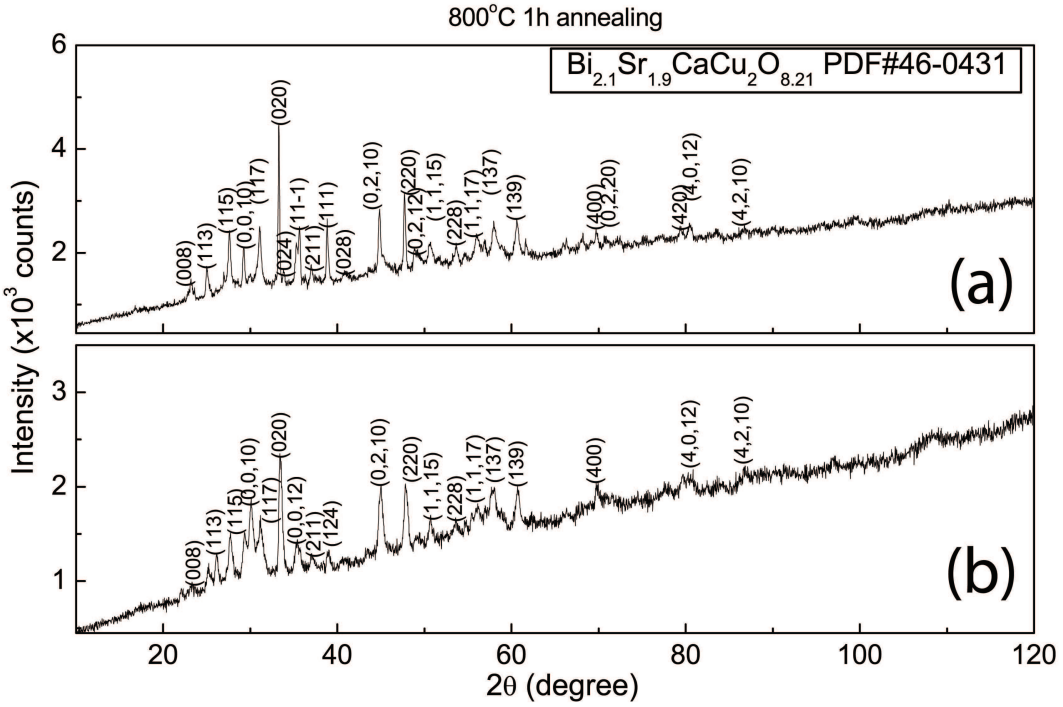

Figure 4.10: XRD results of nanowires synthesized from (a) 1112 precursor and (b) Pb-doped precursor after 800 °C annealing.

According to the analysis of the peaks, the average grain size of the non-doped Bi-2212 sample is about 46 nm. The Pb-doped sample presents a worse crystallinity than the non-doped Bi-2212 sample, as the peaks of the spectrum have a larger full width at half maximum (FWHM), and the average grain size is also found to be smaller (39 nm). This can be attributed to the influence of the addition of Pb, because Pb doping facilitates the formation of the Bi-2212 phase, but it also induces a lattice distortion.

The next issue is how to maintain the fiber structure after 800 °C annealing. The solution is hidden in the TGA-DSC result of the sample as shown in Fig. 4.11. With similar analysis compared to the La-based samples, the first mass drop appears at around 60 °C, which originates from the removal of the crystallized water from the acetates. At around 160 °C, an onset of mass drop appears, which relates to the decomposition of calcium acetate from $Ca(Ac)_2$ to $CaCO_3$. It is followed by a dramatic mass loss accompanied by an intense exothermal reaction. An exothermal peak appears at 211 °C. It can be attributed to the degradation of the polymer polyvinylpyrrolidone. Meanwhile, the Bi^{3+} ions separate from the bismuth acetate and degenerate to Bi^{+} ions at the same temperature range. The second exothermal reaction, visible as a peak at 301.8 °C relates to the deoxidization of $Cu(Ac)_2$ to element Cu. The third exothermal

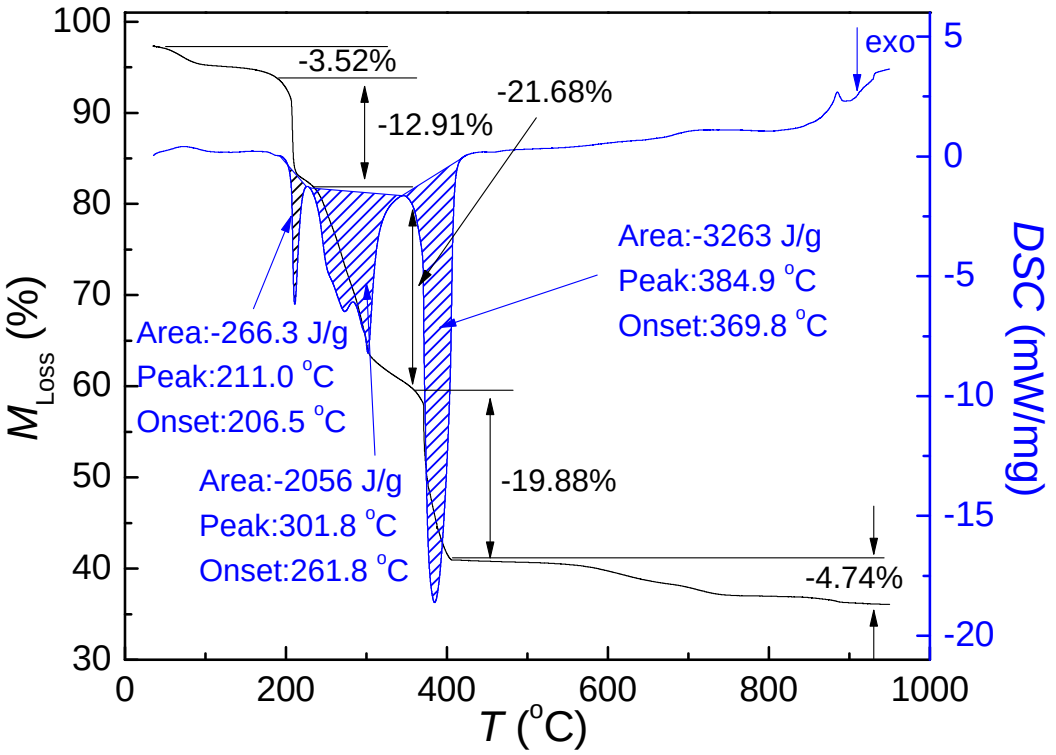

Figure 4.11: TGA-DSC measurement of the as-prepared fiber synthesized from 1112 precursor.

reaction is the most intense one during the whole heating process. It contains three reactions: the deoxidisation of Bi^+ ions to element Bi between 280 °C and 320 °C, then a following oxidisation of Bi to Bi_2O_3 at around 370 °C [62], and the decomposition of $Sr(Ac)_2$ to $SrCO_3$. The decomposition of the polymer proceeds during these reactions. Above 400 °C, Bi_2O_3, $SrCO_3$, $CaCO_3$ and CuO obtained from the former process melt and mix together forming the BiSrCuCaO phase or the BiSrCuO phase, which is determined by the final treatment temperature. The mass loss above 800 °C comes from further melting and evaporation of the BSCCO compound, which would ruin the Bi-2212 phase and form some other phases. Majewski summarised the phase-temperature regimes of the Bi_2O_3-SrO-CaO-CuO system as shown in Fig. 4.12 [63]. The first crystallization of Bi-2212 from a glass state with composition $Bi_2Sr_2CaCu_2O_x$ starts between 600 – 660 °C. Above 650 °C, both the Raveau phase (Bi-2201) and the Bi-2212 phase exist. At 895 °C the Bi-2201 phase reaches its melting point, while the Bi-2212 phase stabilizes and dominates the main phase of the system. In this work, the addition of element Cu, Ca and Pb doping help the samples form a stable Bi-2212 phase at 800 °C.

It turns out that during the thermal treatment, the step at around 380 °C is most important for maintaining the fiber structure, as it consists of at least three chemical reactions. According to the experiment, the fibers synthesized from the 1112 precursor and the Pb-doped precursor can survive the thermal

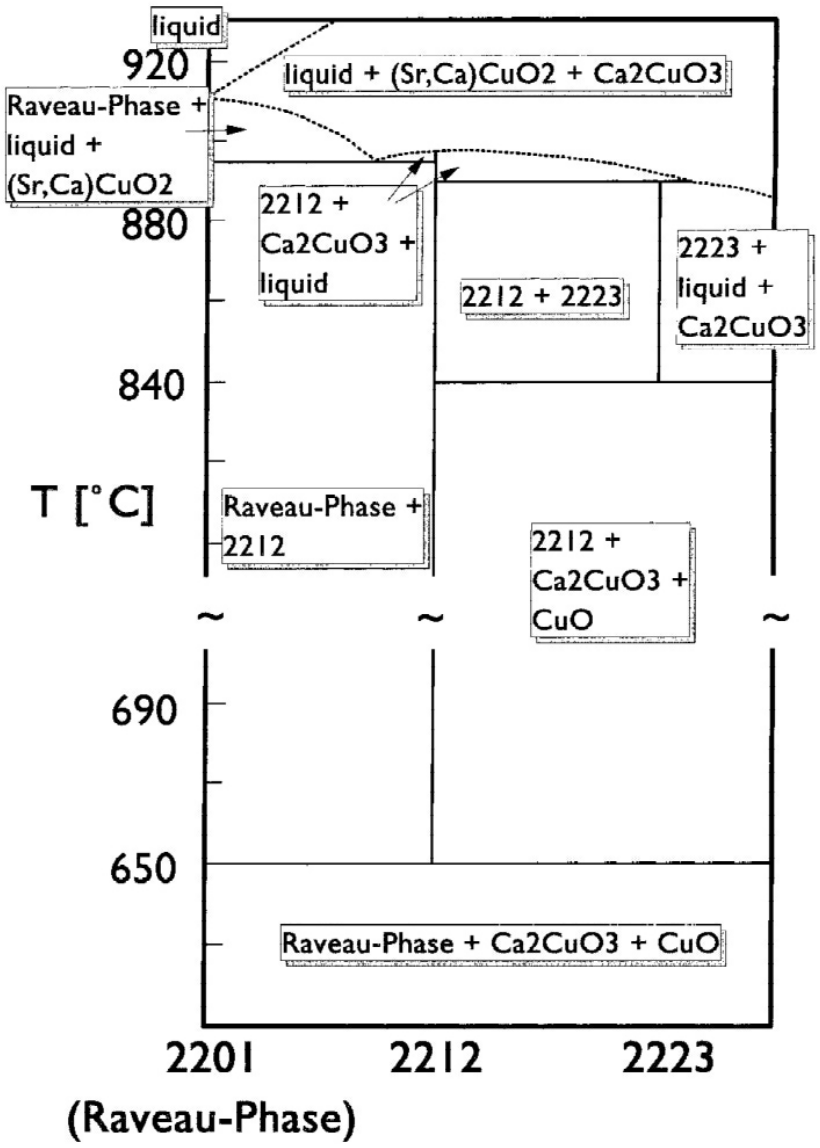

Figure 4.12: Phase diagram of BaSraCuO system [63].

treatment at 384 °C [72]. For the samples electrospun from the Li-doped precursor, this treatment has to be split into two steps: at 360 °C and 400 °C respectively.

Table 4.6 shows the whole thermal treatment steps for the sample synthesized from the 1112 precursor and the Pb-doped precursor. The temperature step at 800 °C was applied to help the samples form the Bi-2212 phase.

By means of thermal treatment, the superconducting Bi-2212 nanowire network sample is obtained. However, there is always a high possibility of the nanowires breaking or melting during the thermal treatment step at 800 °C. In order to increase the production quantity of long Bi-2212 nanowires, a reduction of the final treatment temperature is necessary. A solution to this problem can

Temperature (°C)	Heating rate (°C/min)	Annealing time (hour)
211	3	1
302	3	1
384	3	1
800	3	1

Table 4.6: Thermal treatment steps for non-doped and Pb-doped Bi-2212 samples.

be found in the literature. At the beginning of the HTSc preparation several approaches were described using doping by alkali metals [64, 65, 66], which leads to a reduction of the reaction temperature. It has been reported that the Bi-2212 phase can be obtained at 710 - 720 °C by Li doping [65].
A similar idea was attempted in this work. Here the 1112 precursor was chosen as the basic precursor, as it can form a pure Bi-2212 phase with a better crystalline structure at 800 °C. According to reference [65], the Li is supposed to occupy Cu sites as a dopant. After several attempts, the type C precursor recipe listed in table 4.3 was found to be the optimal recipe. As a result of Li doping, the final treatment temperature of the sample was reduced to 750 °C. Figure 4.13 shows the comparison of the XRD results between the samples

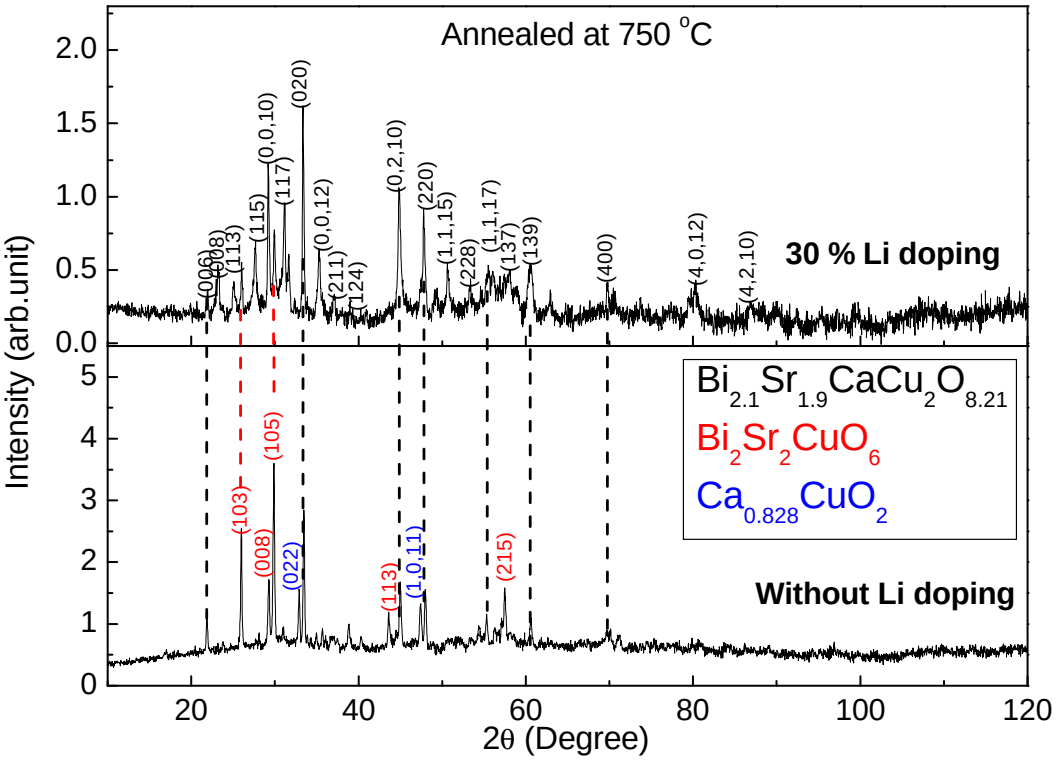

Figure 4.13: XRD of result the Bi-based nanowires synthesized from with-/without Li-containing precursor after 750 °C annealing.

Temperature (°C)	Heating rate (°C/min)	Annealing time (hour)
211	3	1
302	3	1
360	3	2
400	3	1
750	3	1

Table 4.7: Thermal treatment steps for Li-doped Bi-2212 samples.

synthesized from Li-containing precursor and 1112 precursor annealed at 750 °C.
Without Li doping, the major phase of the sample is Bi-2201. As a comparison, the Bi-2212 phase dominates the 30 %-Li-doped sample, even though the Bi-2201 phase still exists. Using the areas under the (006)2201 and (008)2212 peaks, the amount of the Bi-2201 phase can be estimated as ∼30 wt.% relative to the Bi-2212 phase [67]. No Li impurity phase is found in the pattern. It indicates that 30 % Li doping helps the Bi-2201 phase to convert to the Bi-2212 phase at a lower temperature. However, this conversion is not complete.

5 Results and discussion

5.1 $La_{1.85}Sr_{0.15}CuO_4$ nanoribbons

LSCO nanowires were successfully fabricated by the electrospinning technique and subsequent thermal treatment [28]. These samples are superconducting as expected. This verifies that the combination of electrospinning and thermal treatment is a promising method for the synthesis of superconducting nanofibers. In order to investigate whether the geometric structure of the nanofiber influences its superconductivity or not, LSCO nanoribbons with an asymmetric cross-section were prepared for comparison.

5.1.1 Basic characterization of $La_{1.85}Sr_{0.15}CuO_4$ nanoribbons

According to the discussion in section 4.2, the quantity of nanoribbons increases with higher sol-gel precursor concentration. The result in this section is mainly based on the sample synthesized via the type A precursor (the one with the highest precursor concentration) shown in table 4.4.

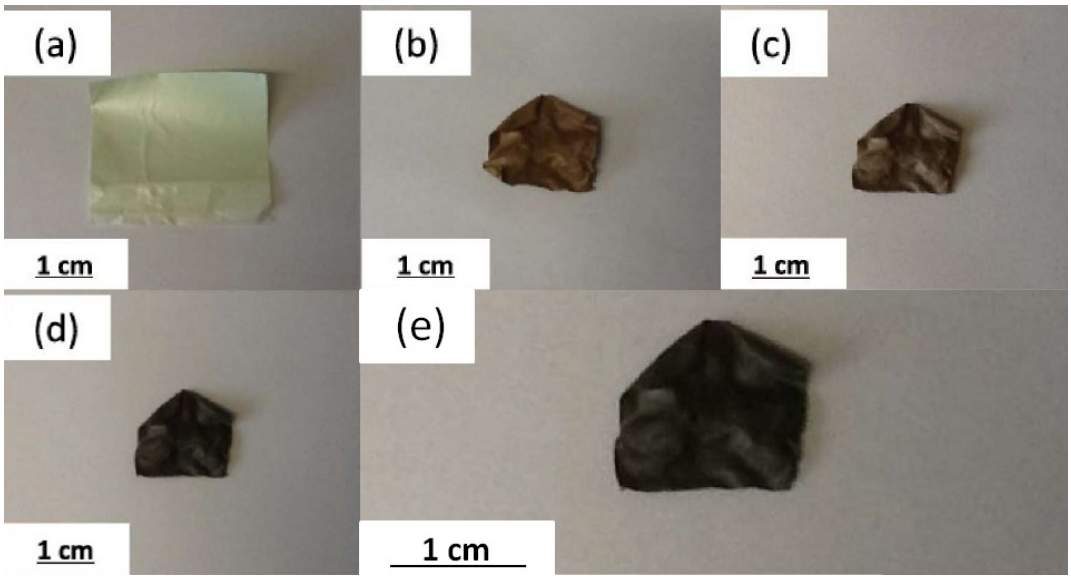

Figure 5.1: Optical images of the sample in different steps of the thermal treatment: (a) As-prepared, (b) 218 °C, (c) 486 °C, (d) 700 °C, (e) 500 °C; (a)-(d) the sample is treated in the air, while (e) the sample is treated in pure O_2 environment [68]. The scale bar is marked as black line in each image.

Figure 5.1 presents optical images of the sample at different steps of the thermal treatment. In the beginning, the sample looked nearly white with a light green color. The green color results from the Cu^{2+} ions and the white background is the result of the fibers crossing each other (Fig. 5.1a). After the heat treatment at 218 °C, the sample appeared brown (Fig. 5.1b) because the PVA started to decompose and engages the browning process. During the heating process up to 486 °C, the sample went through an intense polymer decomposition process, where parts of the organic component turned into carbon dioxide and water vapor. They were removed from the sample during the annealing process. Furthermore, the LSCO phase started to form. Thus, the sample got slightly dark blue (Fig. 5.1c). Then, after the 700 °C thermal treatment, all the organic components had been removed as there is nearly no mass loss above 700 °C in the TGA spectrum (shown in Fig. 4.8). The sample looked completely dark blue (Fig. 5.1d), which is the same color as the bulk LSCO materials have. All the treatments above were carried out in the air. Since the oxygen loss during the thermal treatment is common in LSCO material, additional thermal treatment was applied to the sample with a pure oxygen flow at 500 °C. There was no obvious change in the appearance of the sample after the treatment (Fig. 5.1e), but this treatment avoids the reduction of superconductivity due to oxygen loss.
Figure 5.2 presents a series of SEM images of the LSCO nanofibers at various thermal treatment steps. The observed regions are not directly in the red region as shown in Fig. 4.3, thus both nanowires and nanoribbons can be found. As

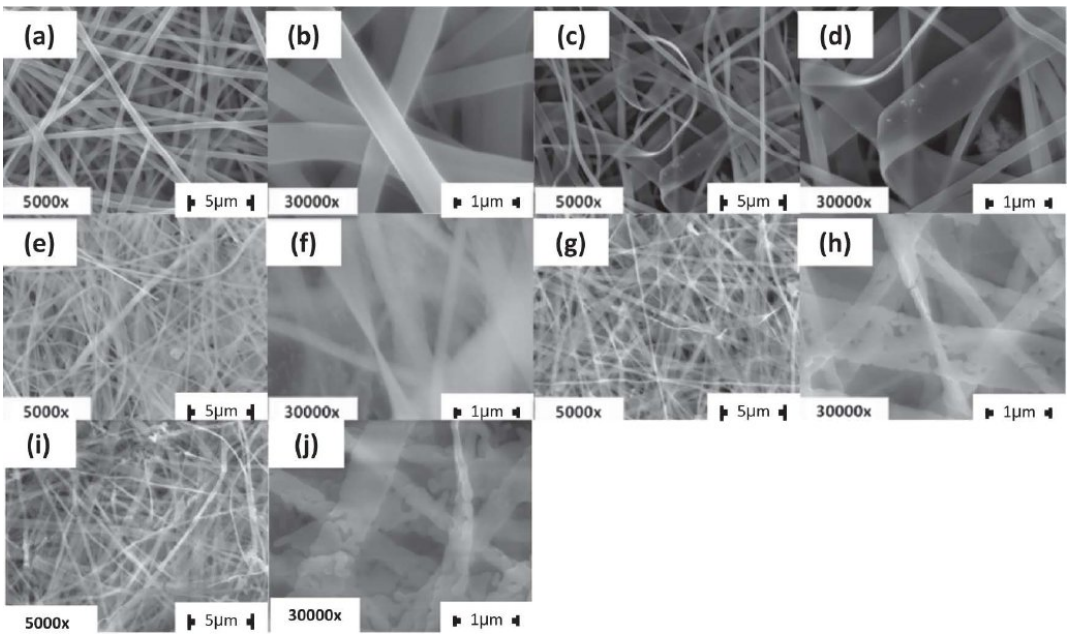

Figure 5.2: SEM images of the nanowires and nanoribbons observed after steps of the thermal treatment: (a) and (b) as- prepared, (c) and (d) 218 °C, (e) and (f) 486 °C, (g) and (h) 700 °C, (i) and (j) 500 °C in O_2 [68].

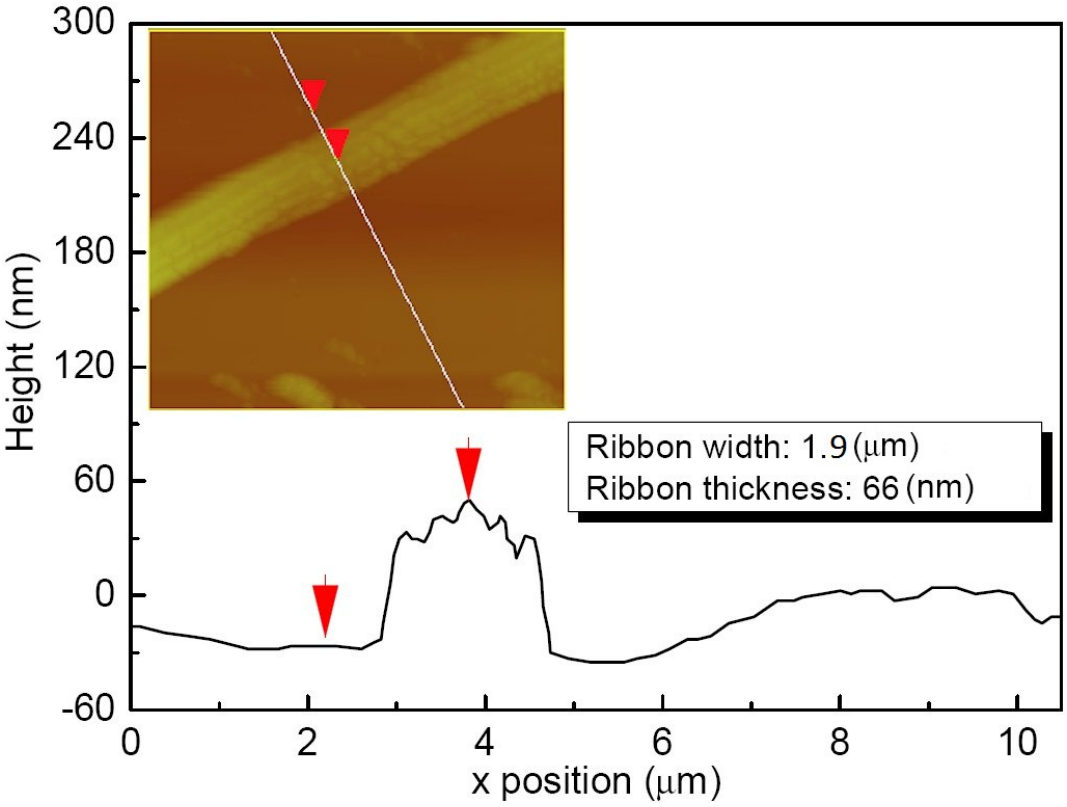

Figure 5.3: AFM analysis of a LSCO ribbon on a silicon wafer. The inset graph presents the AFM scanning of the chosen ribbon, the spectrum is the section analysis of the cross-section area marked on the ribbon with a line.

shown in Figs. 5.2(g)–(j), these nanoribbons are thin and transparent to the electron beam. The resulting width of the ribbon reaches up to 1 µm, but the thickness is in the order of 60 to 80 nm. A more straightforward estimation of the width and the thickness of the ribbon is given by atomic force microscopy (AFM). As shown in Fig. 5.3, the width of the chosen ribbon is about 1.9 µm and the thickness is 66 nm. According to the statics from SEM images, most of the fibers are found in the range of about 100 µm.

Figure 5.4 presents the transmission electron microscope (TEM) observation of the nanoribbons with the electron diffraction pattern shown in Fig. 5.4c. The circular diffraction rings consist of discontinuous spots. This feature can be found in polycrystalline nanomaterials. In this work, the ribbons are formed by single crystal grains. Various orientations of the grains lead to the polycrystalline character of the whole nanoribbon. However, compared to bulk materials, the quantity of grains in nanoribbons is too less to present continuous polycrystalline rings in the electron diffraction observation.

Statistics of the grain size are applied to the TEM images, as shown in Fig. 5.5. The distribution of the grain size has a wide range, from 50 nm up to 250 nm and the average grain size is about 110 nm. Considering the thicknesses of the ribbons are between 60 to 80 nm, it can be concluded that the shapes of the

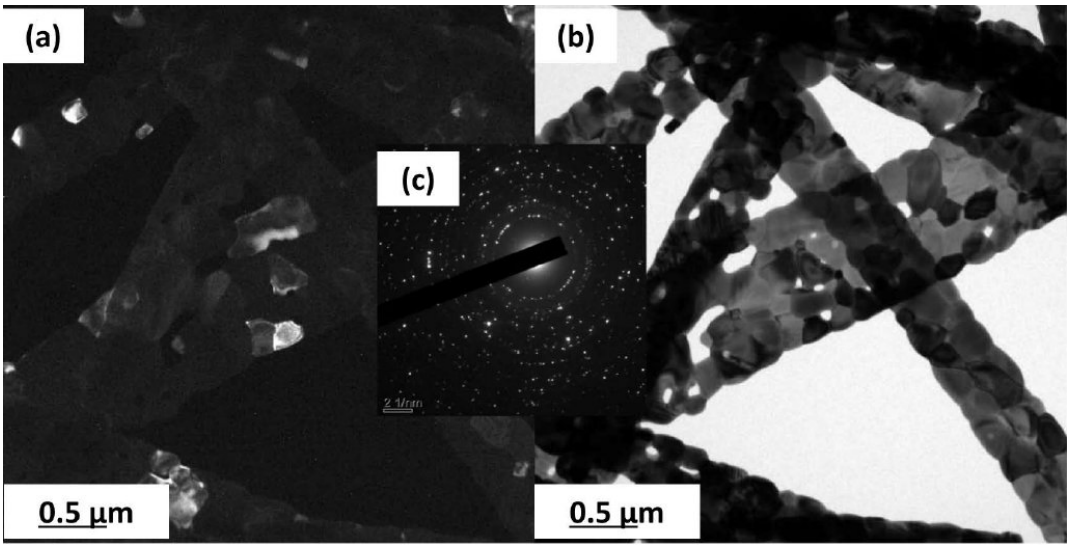

Figure 5.4: TEM images of LSCO nanoribbons. (a) Darkfield image. (b) Brightfield image. (c) Diffraction pattern indicating the polycrystalline character of the nanoribbons [68].

grains are not regular spherical. Furthermore, the ribbons are formed by the grains chained with each other in the single layer. That's why the ribbons are transparent as they are just 'one-layer' thick.
The phase of the nanoribbons has been confirmed by XRD as shown in Fig. 5.6, the peaks are defined by the reference data [74]. A full spectrum refinement

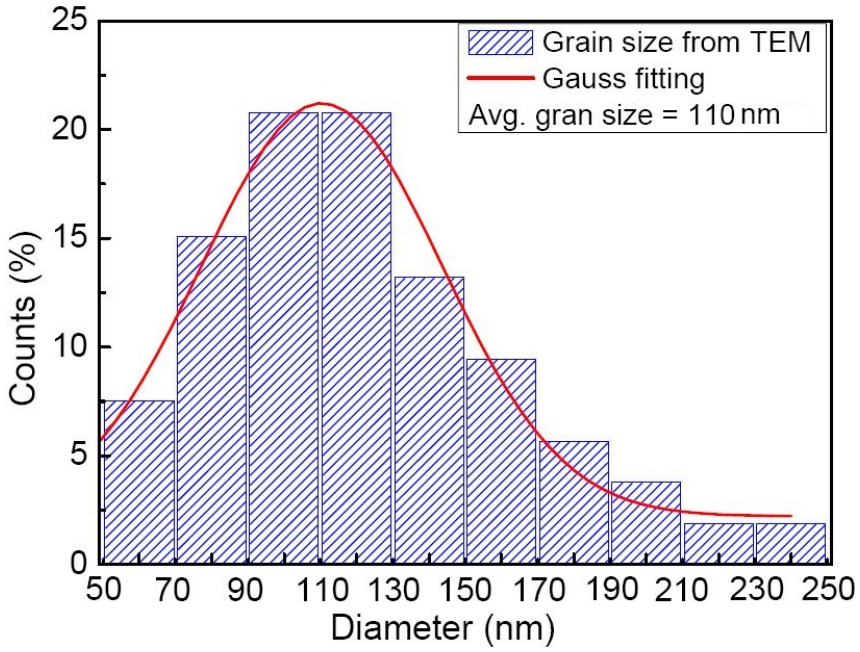

Figure 5.5: Distribution of grain sizes of the LSCO ribbons based on the TEM observation [68].

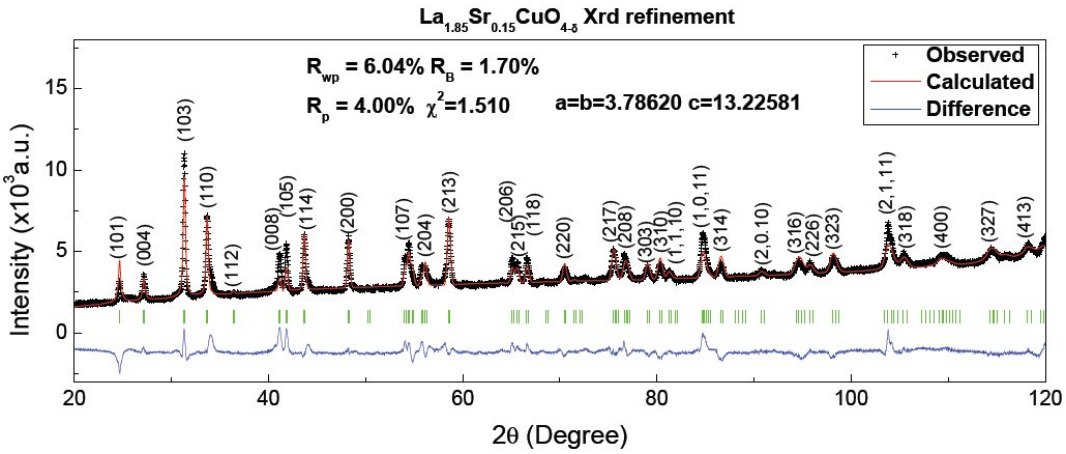

Figure 5.6: XRD result of the LSCO nanoribbons, with a full spectrum refinement. The black dots are the experimental data, the red line denotes the calculation, the green bars are the peak positions and the blue line represents the differences [68].

is applied to the data, as shown by the red fitting line in the figure. The lattice constants determined from the refinement are $a = b = 3.7862$ Å and $c = 13.226$ Å, which are slightly larger than those of the standard bulk materials ($a = b = 3.7749$ Å, and $c = 13.2231$ Å).

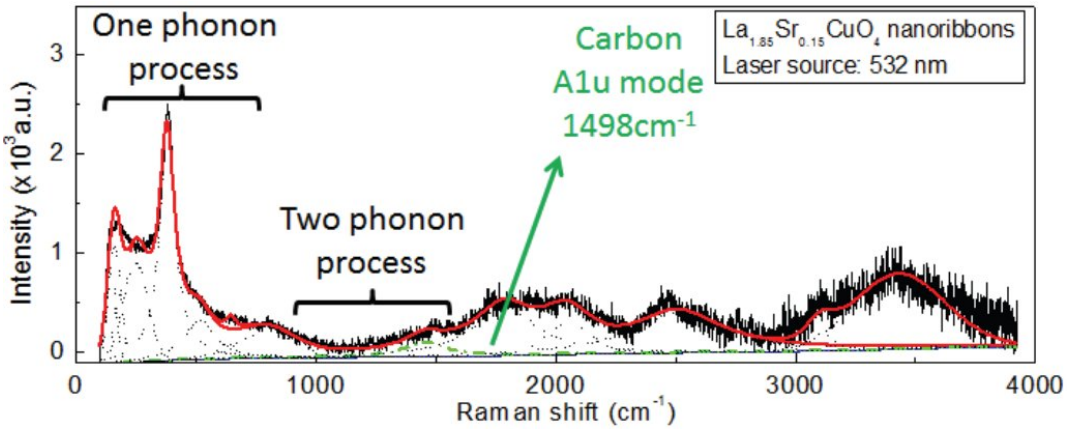

Figure 5.7: Raman spectrum of the LSCO nanoribbons.

Figure 5.7 presents the Raman spectrum of the LSCO nanoribbons. Generally, the spectrum can be separated into three regions:

1. The region from 100 cm^{-1} to 800 cm^{-1}, the peaks in this range can be attributed to the one phonon process. There are several vibration modes in this range:
   a) A_{1g} mode representing the vibrations of the La and the apex O atoms (∼150 cm^{-1}, 429 cm^{-1}) [75];
   b) B_{3g} mode representing the vibration of O (516 cm^{-1}) [76];
   c) E_g mode representing the CuO intrinsic vibration mode (235 cm^{-1})

[77];

d) B_{1g} mode representing the vibrations of the La atoms along with the b axis ($\sim$370 cm^{-1}) [76];
e) B_{2g} mode representing the tilting octahedral vibrations along the two diagonal axes of the CuO_2 plane ($\sim$670 cm^{-1}) [76];
f) the single phonon scattering mode ($\sim$782 cm^{-1}) [78].

2. The region from 800 cm^{-1} to 1100 cm^{-1}, the broad peak can be attributed to the two-phonon process, like the multiple phonon scattering mode [78].
3. The region from 1100 cm^{-1} to 4000 cm^{-1}, the humps can be attributed to the high energy electron dispersion of the B_{1g} and the B_{2g} mode [79].

Similar to the case in the nanowires, the A_{1g} mode at 429 cm^{-1} decreases while the B_{1g} mode at 370 cm^{-1} increases compared to the bulk material [75]. Such symmetry breaking can be ascribed to the weakened electron-phonon coupling [28, 80].

5.1.2 Superconductivity of $La_{1.85}Sr_{0.15}CuO_4$ nanowires and nanoribbons

The coherence length of the cuprate superconductors is about 3 to 5 nm. The London penetration depth is about 100 – 500 nm. The thickness of the LSCO nanoribbons is about 60 to 80 nm. That means the nanofibers are large enough for the existence of Copper pairs and the sizes are comparable to their penetration depth.

The superconductivity of the nanofibers was confirmed by magnetic measurement in SQUID. Figure 5.8 presents the zero-field cooling (ZFC) $m(T)$ curves of the nanowires and nanoribbons with detection field of 2 mT. The turnings of the $m-T$ behavior can be found in both curves of the nanowires and nanoribbons. In the $m(T)$ curve of the nanowires, the onset of the turning appears at 19.2 K [28], while in the curve of the nanoribbons, two onsets appear at 29.3 K and 13.9 K respectively. Defining the first onset temperature as T_c, the T_cs of the nanowires and the nanoribbons are 19.2 K and 29.3 K, respectively. Both T_cs are lower than the one in the bulk materials (37 K).

Considering the preparation process of the nanowires and nanoribbons, all the synthesis parameters are the same except the precursor concentration. As a result, the average grain size of the nanowires ($\sim$20 nm [28]) is much smaller than the nanoribbons ($\sim$110 nm). The T_c of the nanowires is lower than the T_c of the nanoribbons. Therefore, the lower T_c of the nanowire can be attributed to the smaller grain size of the nanowire. The magnetic field occupies a certain depth below the surface of each grain, only the unoccupied region in the center presents the Meissner effect. In other words, it is the size-effect resulting in a decrease of T_c.

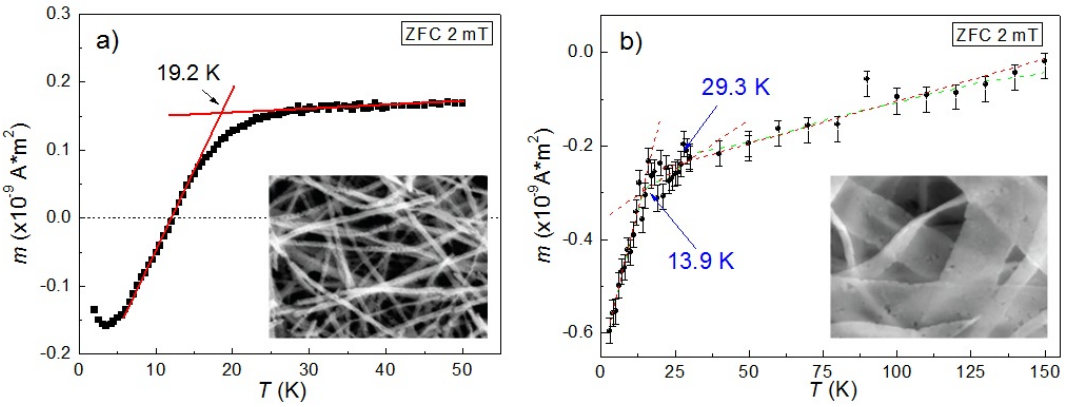

Figure 5.8: ZFC $m(T)$ curves of the LSCO (a) nanowires and (b) nanoribbons with a detection field of 2 mT [28, 68].

5.2 $Bi_2Sr_2CaCu_2O_8$ nanowires

An attempt of electric measurement on the LSCO nanowires and nanoribbons ended up with no discovery of a resistance drop in the $R(T)$ measurements. Due to the non-superconducting grain boundaries, the weak superconductivity of the LSCO nanofibers is suppressed by the strong non-zero resistance background. In order to have a better investigation of the electric properties of the superconducting nanofibers, the famous HTSc BSCCO system was chosen to be the subject of investigation. In the BSCCO family, there are two popular superconducting phases: Bi-2212 and Bi-2223 ($Bi_2Sr_2Ca_2Cu_3O_{10}$). For bulk materials, Bi-2212 has a T_c about 84 to 92 K and the Bi-2223 has a higher T_c up to 106 K. However, the Bi-2223 phase can be obtained only at high pressure and high melting temperatures, which is not suitable for the synthesis by electrospinning. Therefore, Bi-2212 is a better option. Three types of Bi-2212 (non-doped Bi-2212, Pb-doped Bi-2212, and Li-doped Bi-2212) nanowires are investigated in the following sections.

Figure 5.9 presents the microstructure of the non-doped Bi-2212 and the Pb-doped Bi-2212 nanowires at different thermal treatment steps. When treated at higher temperatures, the organic compound is gradually removed and the wire structure starts to bend. With the crystallization process, the grains grow larger. After the thermal treatment, the nanowires are not as smooth as the as-prepared ones. The junctions between the grains become the main connections and maintain the wires' structure, replacing the polymer binding. Since the fibers are randomly aligned and cross each other, the whole sample can be treated as a polycrystalline nanowire network system. The distribution of the diameter was obtained from SEM images of the non-doped Bi-2212 nanowires and the Pb-doped Bi-2212 nanowires, as shown in Fig. 5.10. The diameters of both types of nanowires range between 140 and 580 nm. The average diameter of the non-doped Bi-2211 nanowires is 318 nm while the Pb-doped one is 328 nm.

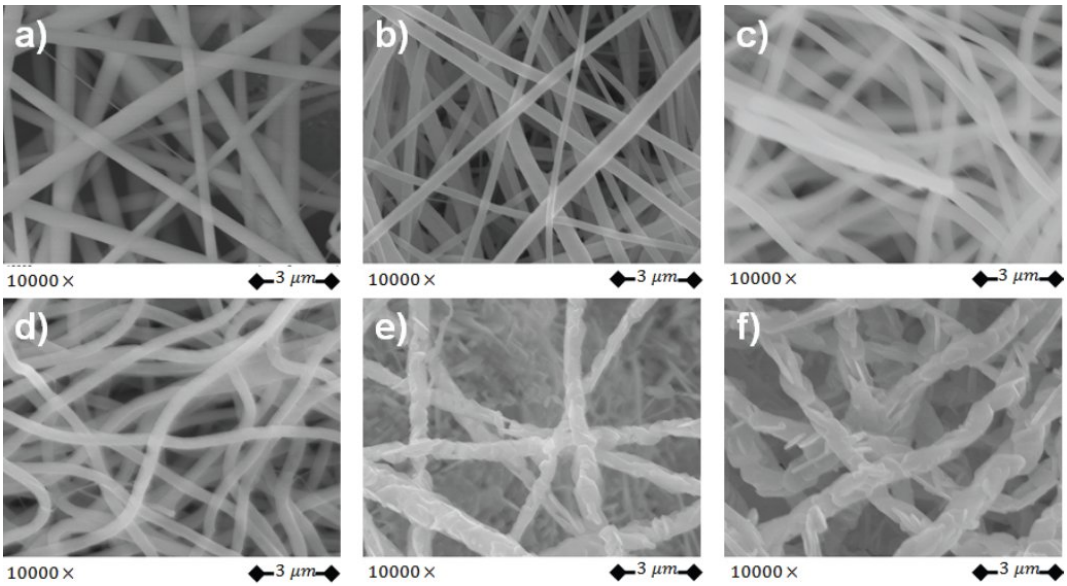

Figure 5.9: SEM images of the non-doped Bi-2212 nanowires (a)–(e) and the Pb-doped Bi-2212 nanowires (f) at a magnification of 10000× at different temperatures. (a) as-prepared, (b) 211 °C, (c) 302 °C, (d) 384 °C, and images (e) and (f) present the microstructures after the treatment at 800 °C in air and at 500 °C in an O_2 environment, respectively [72].

average parameters	non-doped	Pb-doped
Length (µm)	104	88
Diameter (nm)	318	328
Grain size$_{\mathrm{TEM}}$ (nm)	120	101
Grain size$_{\mathrm{XRD}}$ (nm)	46	39

Table 5.1: Structure comparison of the non-doped Bi-2212 nanowires and the Pb-doped Bi-2212 nanowires [72].

A further structure comparison is shown in table 5.1. Both nanowires have an average length of 100 µm, and an average grain size of 120 nm and 101 nm, respectively. These values are much larger than the grain sizes estimated from the XRD peaks. Certain deviations stem from the shape of the grains. In XRD, the grains are assumed to be spherical, and the data is estimated using a projection plane of the surface, which loses the stereo information. However, according to SEM and TEM observation, the shape of the grains is an oblate ellipse. These grains are ∼300 nm long, ∼100 nm wide, but just ∼40 nm thick. Such an anisotropic structure leads to the misjudgement of the XRD estimation. The superconductivity of the nanowires is proven by their magnetic and electric properties. According to section 4.5.2, the non-doped Bi-2212 nanowires and the Pb-doped Bi-2212 nanowires experienced the same thermal treatment. The comparison between the properties of these two types of Bi-2212 nanowires demonstrates the difference between the nanowires due to the deviation of their

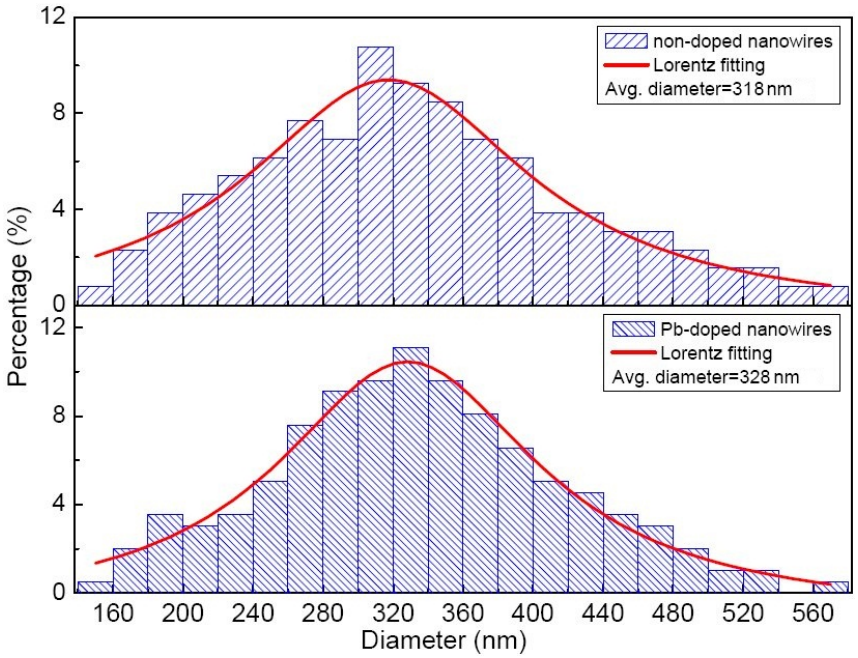

Figure 5.10: Diameter statistics of the non-doped Bi-2212 nanowires and the Pb-doped Bi-2212 nanowires [72].

components. Li-doped Bi-2212 nanowires were produced with the purpose of optimizing the preparation process, the final treatment temperature of these nanowires is lower than the final treatment temperatures of the other two. This type of Bi-2212 nanowires is introduced in a separated section.

5.2.1 Magnetic properties of $Bi_2Sr_2CaCu_2O_8$ nanowires

The magnetic properties of the Bi-2212 nanowires were measured by SQUID. Figure 5.11 presents the $m(T)$ curves of the two types of Bi-2212 nanowires. There are two kinks in the $m(T)$ curves. The first kink appearing at higher temperature can be defined as the T_c at which the samples change from normal state to superconducting state, because the samples become diamagnetic below this temperature. The second kink is related to the magnetic irreversibility, where at values below that temperature the magnetic behavior becomes irreversible [69]. T_c is obtained around 76 K for the non-doped nanowires, while it is around 84 K for the Pb-doped nanowires. The FC curves start to deviate from the ZFC curves at around 70.2 K and 62.7 K in the non-doped nanowires and Pb-doped nanowires respectively. It denotes that below these temperatures the samples become field irreversible respectively. For the non-doped nanowires with a diameter comparable to the penetration depth, the lower T_c may be attributed to thermal fluctuations induced by the decreasing size of the sample [21]. On the other hand, the Pb-doped Bi-2212 nanowires show a higher T_c. The influence of Pb doping on the superconductivity of Bi-2212 bulk and thin-film materials has been investigated for a decade [21, 58, 59, 82, 83]. It is

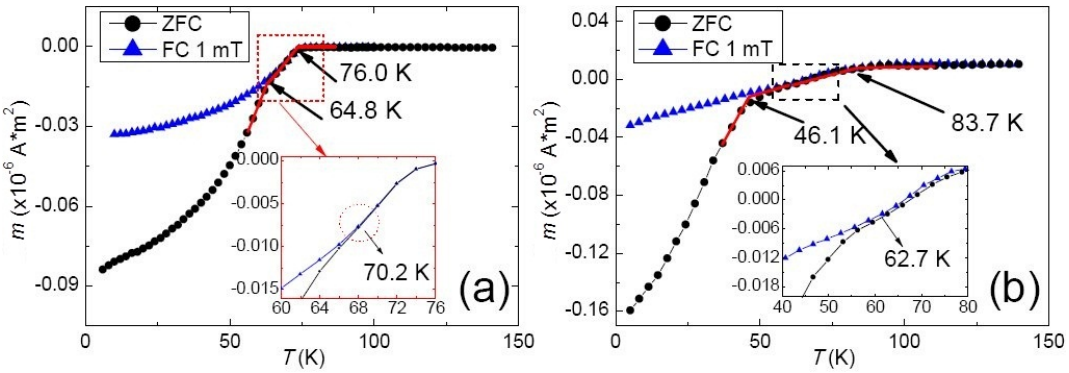

Figure 5.11: ZFC and FC (at 1 mT) $m(T)$ curves of Bi-2212 nanowires: (a) non-doped Bi-2212; (b) Pb-doped Bi-2212. The inset graphs demonstrate the initial temperatures of the irreversibility field [72].

well known that the additional Pb substitutes Bi in the lattice structure. Pb doping can increase the volume fraction of the superconducting phase [21] and reduce the electronic anisotropy of Bi-2212 [82]. Therefore, a certain amount of Pb can enhance the superconductivity of Bi-2212. However, with increasing doping level, the lattice distortion due to the Pb substitution will suppress the superconductivity [83].

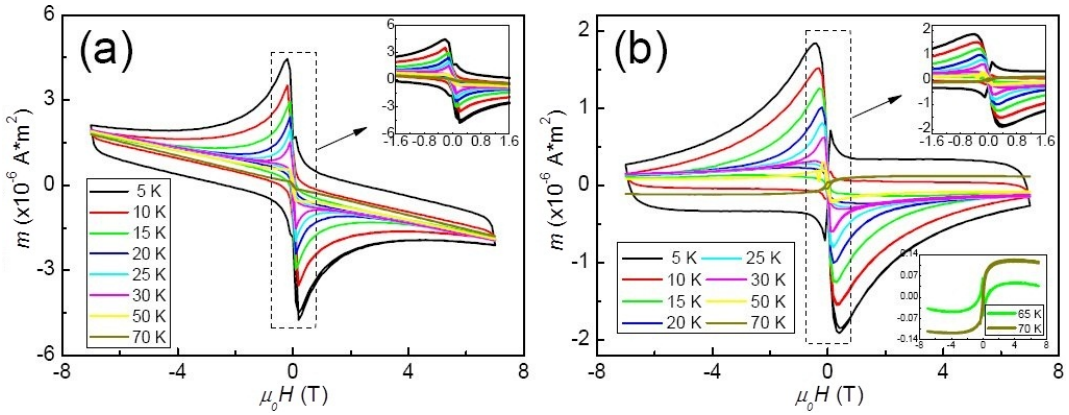

Figure 5.12: $m(H)$ curves of two types of Bi-2212 nanowires ranged from 5 K to 70 K: (a) non-doped Bi-2212; (b) Pb-doped Bi-2212. The upper insets in (a) and (b) present details at low fields, and the lower inset in (b) shows the magnetization loops at 65 K and 70 K in detail [72].

Figure 5.12 demonstrates the magnetization loops of the non-doped nanowires and the Pb-doped nanowires in a magnetic field up to ± 7 T in the temperature range between 5 K and 70 K. Starting from 5 K, all the loops are fully asymmetric with respect to the $m = 0$ axis. The so-called fishtail effect [84] in the magnetization loops can be seen in the form of double peaks appearing close to zero field, as shown in the upper insets of Fig. 5.12. A minimum of the magnetic moment can be seen close to the full penetration field. The magnetization loops of the Bi-2212 nanowire networks are different from the

typical symmetric loop of the bulk cuprate superconductors [85]. This indicates that there is more than one pinning regime inside the nanowires [86], which is in good agreement with their polycrystalline character.

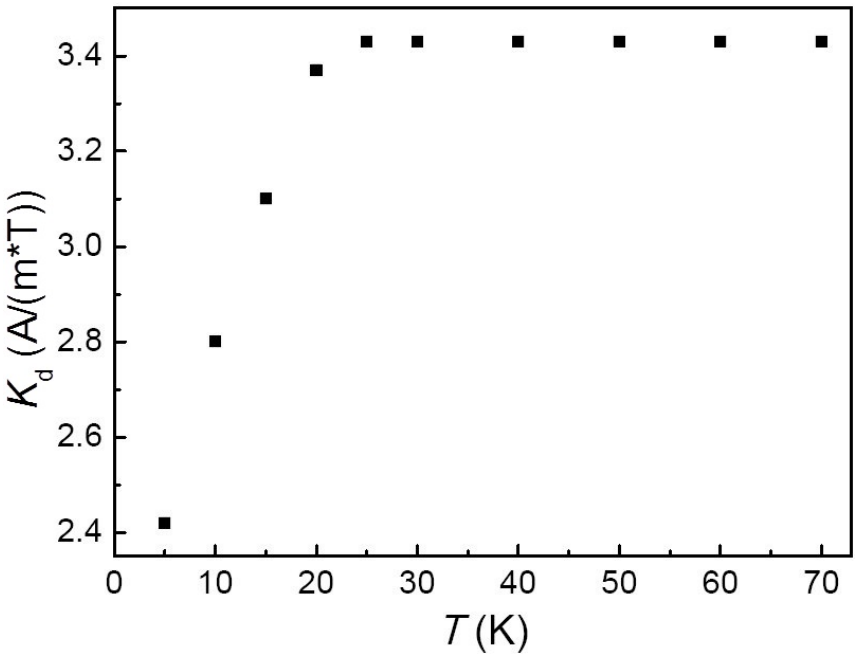

Figure 5.13: Temperature dependence of K_D for the non-doped Bi-2212 nanowires.

In the case of the non-doped nanowires, the irreversible superconducting loop is maintained up to 70 K, corresponding to the result obtained from the $M(T)$ curve that T_c is about 76 K. In the case of the Pb-doped nanowires, the irreversible superconducting loop vanishes above 65 K, and a reversible paramagnetic curve is observed. This demonstrates that above this temperature the irreversibility disappears due to no flux pinning and no pinned vortices in the nanowire network. This result is in good agreement with the initial point of irreversibility at around 63 K shown in the inset of Fig. 5.11b. It can be concluded that the pinning landscape of the Pb-doped nanowires is worse than that of the non-doped nanowires, especially at high temperatures. Furthermore, the $M(H)$ loops of the non-doped nanowires demonstrate the presence of an additional diamagnetic contribution, which can be expressed as $M_D = -K_D H$. The temperature dependence of the coefficient K_D is shown in Fig. 5.13. K_D appears to increase rapidly with rising temperature. This is untypical for diamagnetic atoms. There are several possible explanations for this behavior, e.g., one can interpret this feature as self-diamagnetism of the normal cores of Abrikosov vortices [46, 87]. The diameters of the Abrikosov vortices increase with temperature, similar to the coherence length $\xi(T)$. In this case, it follows that $K_D(H,T) \sim \xi(H,T)^2$ and M_D is a complex function of H. If the diamagnetic background originates from Abrikosov vortices, then it should also appear in the Pb-doped nanowires, which is not the case presented

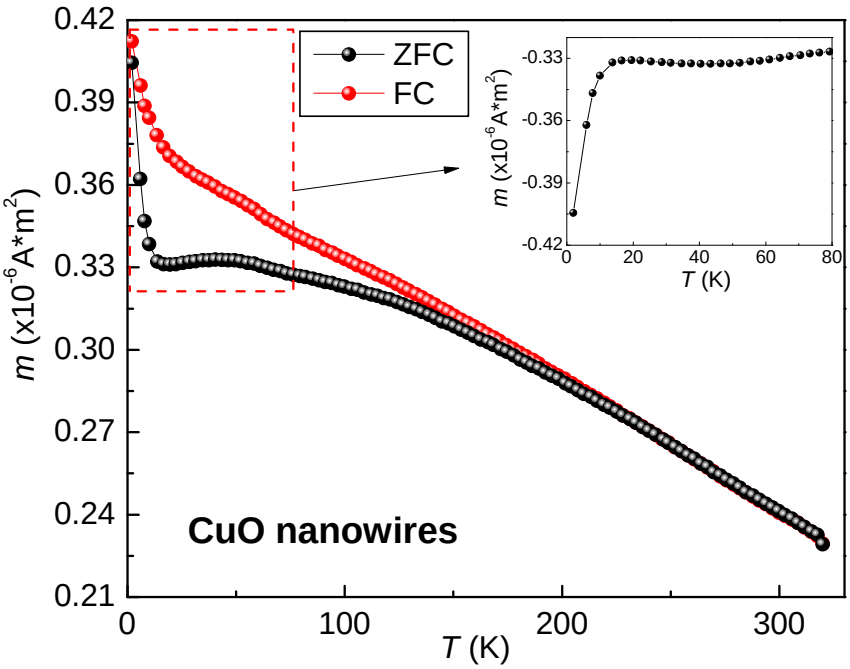

Figure 5.14: ZFC and FC (at 0.1 T) $m(T)$ of CuO nanowires, the inset graph demonstrates the $-m$ expression of the chosen area of the ZFC $m(T)$ curve.

in Fig. 5.12b. Recalling the preparation of the precursors explained in section 4.1, in order to suppress the impurity formation, excess of Ca and Cu elements were induced to the precursor of the non-doped nanowires. It can be predicted that the CuO phase exists in the non-doped nanowires. Figure 5.14 presents the $m(T)$ curves of the CuO nanowires with detection field of 0.1 T. There are three regions in the ZFC $m(T)$ curve throughout the observed temperature range:

1. In the region above 100 K, the magnetic moment decreases significantly with increasing temperature, and eventually merges with the FC $m(T)$ curve.
2. From 20 K to 100 K, the variation of the magnetic moment with temperature is not as obvious as it was the case in the former region, especially in the range from 20 K to 50 K, the curve is nearly horizontal in respect to the temperature axis.
3. Below 20 K, the magnetic moment dramatically increases with decreasing temperature.

The K_{D} behavior turns out to be similar to the $-m$ behavior of the CuO nanowires as shown in the inset of Fig. 5.14. This proves the assumption that the diamagnetic background in the $m(H)$ loops of the non-doped nanowires can be attributed to CuO impurity. It originated from an excess of Cu in the precursor. In the case of Pb-doped nanowires, there is no excessive Ca or Cu, thus no diamagnetic background appears in Pb-doped nanowires.

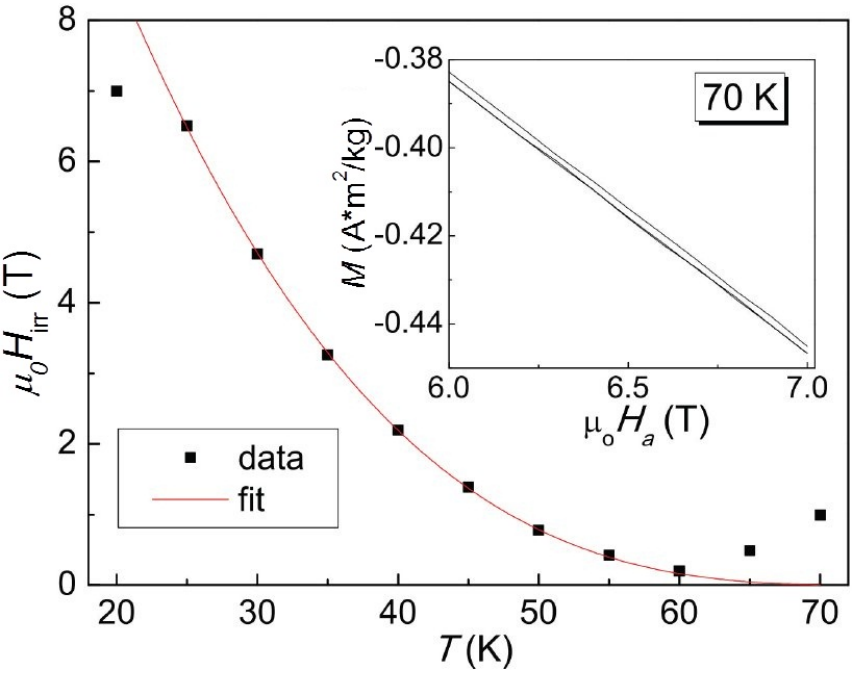

Figure 5.15: Field irreversible behavior $H_{\mathrm{irr}}(T)$ of the nanowire network between 20 K and 70 K. The red line is a fit using equation (5.1) [69]. The inset graph is the high field regime of the $M(H)$ loop at 70 K.

In HTScs, the temperature dependence of the irreversibility field $H_{\mathrm{irr}}(T)$ is an important parameter. Figure 5.15 presents the $H_{\mathrm{irr}}(T)$ behavior of the non-doped Bi-2212 nanowires. From the $M(H)$ loops, H_{irr} is determined directly from the magnetization without invoking a current criterion. This procedure works well within the temperature range between 20 K to 60 K. It can be seen that the irreversibility field decreases monotonously with rising temperature. The data can be fitted well by the function [88]:

$$H_{\mathrm{irr}} = A \times (1 - T/T_{\mathrm{c}})^3. \tag{5.1}$$

This behavior has been observed by various authors in Bi-2223 and Bi-2212 samples [88]. By means of the fitting, the factor $A = H_{\mathrm{irr}}(0)$ is determined to be 22.1 T while the T_{c} is determined to be at 74.4 K, it nearly corresponds to the value of 76 K obtained from the $M(T)$ curve. This certifies the validity of the fitting. When the temperature is lower than 20 K, the available magnetic field of 7 T is not strong enough to determine the H_{irr}. Above 60 K, it is difficult to determine the closing of the loops as the $M(H)$ data run practically parallel to each other, which is illustrated in the inset of Fig. 5.15.
Due to the asymmetric behavior of the $M(H)$ loops with respect to axis $M = 0$, it is not possible to apply the common Bean formalism for the estimation of J_{c} from the magnetization data. For the first attempt, the approach of a three-current model from Senoussi [89] was employed. This model considers the current contributions from Josephson contacts between grains and the shielding

of the entire sample. These features also appear in the present polycrystalline nanowire network system.

The estimation of the critical current density J_m is achieved by fitting the $M(H)$ loops based on the assumption that the critical current density behaves exponentially in an external field, and the magnetic moment can be described by the critical current density J_m, the external field H, an effective radius R, and some characteristic parameters H_0, R_0, which are determined by the magnetic behavior of the sample. In the field sweep process, the grains of the sample start to decouple when the external field is higher than H_0. The characteristic length R_0 is always of the order of the Josephson penetration depth. Then M can be expressed by the two equations below [89]:

$$M = \frac{J_m(H)R}{30}\left(1 - \frac{e^{-h}}{4r_0} + \frac{e^{-2h}}{10r_0^2}\right), \tag{5.2}$$

$$\begin{aligned} M &= \frac{H_{c1}}{4\pi}\frac{\ln(H_{c1}/H)}{\ln(\lambda/\xi)}, \\ \text{with} \quad H_{c1}(T) &= H_{c1}(0)\left[1 - \left(\frac{T}{T_c}\right)^m\right]. \end{aligned} \tag{5.3}$$

where $h = H/H_0$, $r_0 = R_0/R$, λ and ξ are the penetration depth and the coherence length, respectively. The first and third quadrants of $M(H)$ curve can be then fitted by equation (5.2), the second and forth quadrants can be fitted by equation (5.3) as shown in Fig. 5.16a. The fitting parameters to the

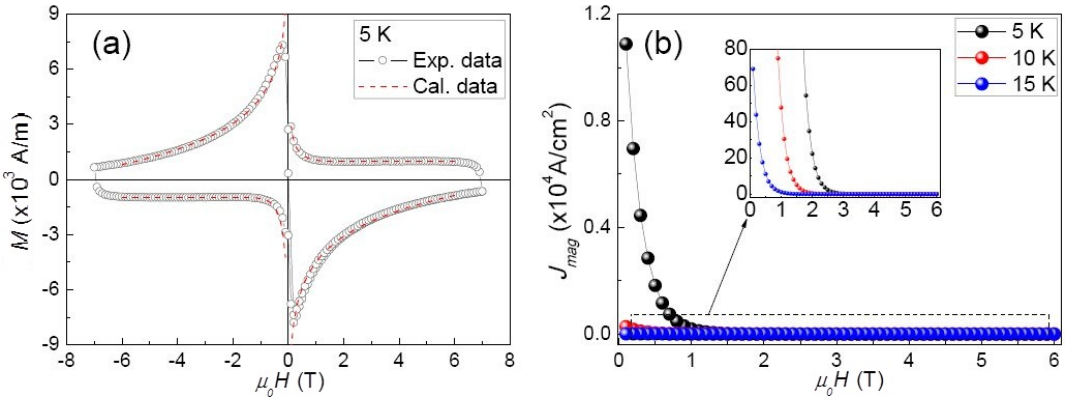

Figure 5.16: (a) Magnetization M as a function of the applied field at T = 5 K and the calculated loops using the three-current model, (b) the estimated J_m dependence on the external field at 5 K, 10 K, and 15 K [69].

data at 5 K are $H_0 = 3.11$ T, $H_{c1}(0) = 16.9$ T, $R = 940$ µm, and $R_0 = 233$ µm. The constant m is usually 2.2 for weakly coupled grains [89]. The estimated critical current densities at various temperatures are presented in Fig. 5.16b. According to Fig. 5.16, the fitting matches the experimental data. However, the fitting value of R_0 is in the micrometer scale. It is much larger than the coherence length, which is in the nanometer scale. Certain irrationality comes

from the fundamental hypothesis of the model. The model is based on the Bean model and it is assumed that the vortices are pinning the whole sample. Whereas the nanowires are polycrystalline, they contain a large number of grain boundaries, which are non-superconducting. That means there are regions where no vortices are pinned. An accurate estimation of the critical current density from the magnetization data requires a model taking the vortex pinning distribution into account. Therefore, ECSM is employed for the estimation of the critical current density.

5.2.2 Superconducting parameters estimated by ECSM

Figure 5.9 presents the SEM images of the nanowires. It demonstrates that the nanowires form a nanowire network system. Figure 5.17 presents the TEM brightfield image of the non-doped Bi-2212 nanowires, revealing the polycrystalline character of the individual nanowires. It clearly demonstrates that the nanowires are formed by elongated grains chained to each other. The grain boundaries are highlighted by red lines, which are supposed to be non-superconducting and the interconnections between the nanowires provide weak-links to the network system. The density of the nanowire network is found to be 0.0459 g/cm^3. This is considerably lower than the theoretical density of bulk Bi-2212 (6.4 g/cm^3) [90]. According to the observation from SEM and TEM, the nanowire network is a highly porous system.
The three-current model is a suitable model for the nanowire network system, even though it did not provide a correct estimation of the critical current density in the former section. The main problem originates from the misestimation of the vortex pinning distribution. Therefore, this model is still being used in the following fitting procedure. The current flows in the nanowire network are separated into three types: a high-field component related to the current inside grains (in-grain current), the other two low-field components related to the current passing through the grains (intergrain current) and the current between individual nanowires in the network (weak-link current). Figure 5.18 shows a schematic view of the current behavior inside a polycrystalline nanowire and a nanowire network system. In Fig. 5.18a, the arrows represent the in-grain currents inside the individual grains while the dashed lines refer to the intergrain currents passing through the grains over several grain boundaries. In Fig. 5.18b, the red arrows represent the weak-link current flows among the nanowires. As it can be seen in Fig. 5.17, there are interconnections between the individual nanowires, forming weak-links in the network system. These weak-links help the main current pass through the whole network system. The in-grain currents can be treated as local currents within superconducting grains, the intergrain current and weak-link current contribute to the main current flow in the whole nanowire network system. According to the discussion above, the estimation of the critical current density can be separated into two parts: a high field component for the local current density and a low field component for the average current density.

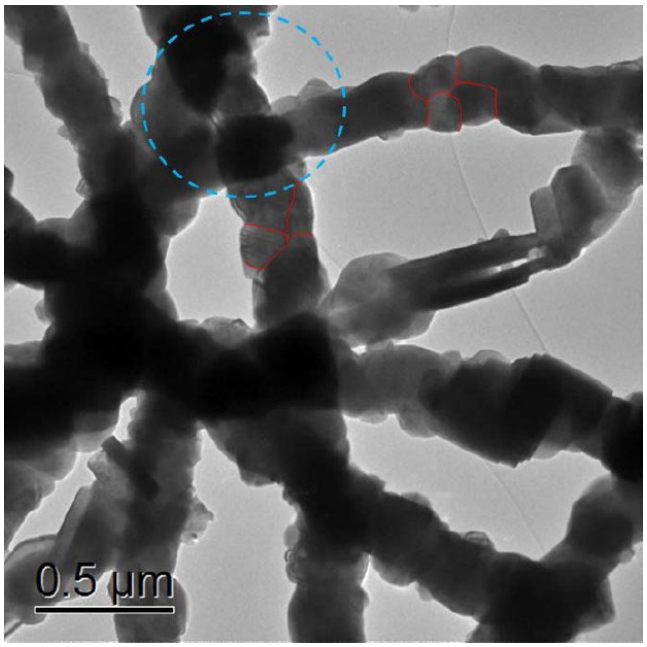

Figure 5.17: TEM bright-field image of the non-doped Bi-2212 nanowires. The red lines highlight the grain boundaries within the nanowires, while the blue circle indicates an interconnection between nanowires [71].

For the non-doped Bi-2212 nanowire network sample, the $M(H)$ loop below T_c is a superposition of a hysteresis loop $M_s(H)$ of superconducting nanowires and an additional diamagnetic magnetization $M_D(H)$ as shown in Fig. 5.12. This diamagnetic magnetization originates from the excessive Cu, which forms the CuO phase. To extract the superconducting magnetization loop $M_s(H)$, the diamagnetic magnetization $M_D(H) = \chi_m H$ is subtracted from the measured $M(H)$ loop. It is plausible to observe the high-field portion of $M(H)$ curves above H_{c2}, where $M_s(H) = 0$. The value of χ_m is selected to obtain $|dM_s^+/dH| \approx |dM_s^-/dH|$ at high H, where $M_s^{\pm}$ denotes the branch of the $M_s(H)$ loop during an increase (decrease) of H. After this procedure, the obtained $M_s(H)$ loop is not tilted in high H as shown in Fig. 5.19. This means that the diamagnetic background has been successfully removed.
In ECSM, the magnetization is defined by $M(H) = -H + \bar{B}(H)/\mu_0$, where $\bar{B}$ is the average magnetic field in the sample and μ_0 is the vacuum permeability [53]. The average magnetic field results from integration of the local magnetic field $B(\mathbf{r})$, where $\mathbf{r}$ is the position vector. For a polycrystalline nanowire network system, the magnetic field penetration is influenced by the porosity and the grain distribution [91]. The magnetic properties of the polycrystalline sample at high fields can be reduced to the characteristics of a single average grain, then the magnetization of the superconducting phase is determined by $M(H) = -H + P_s\bar{B}(H)/\mu_0$, where P_s is the volume content of superconducting phase in the sample [55]. Here the value of P_s is obtained from the comparison between the sample density and the theoretical density of the Bi-2212. For the non-

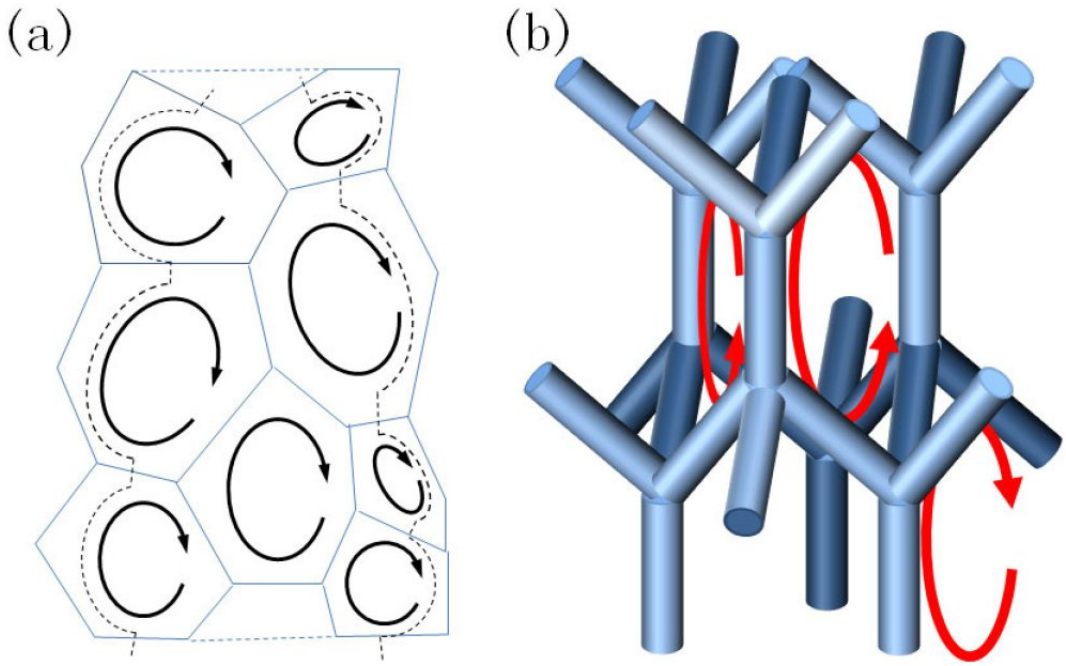

Figure 5.18: (a) Model of the current flow through an individual nanowire. The bold circular arrows represent the in-grain currents. The dashed lines indicate the intergrain currents passing through the grain boundaries. (b) Scheme of the nanowire network. The red arrows indicate the weak-link currents between the individual nanowires [71, 100].

doped Bi-2212 superconducting nanowire network, the relative superconducting content P_s is only 0.72 %.
The advantage of ECSM in comparison to the former model is the introduction of the concept of vortex distribution and the depth of the surface region with equilibrium magnetization l_s. This is the depth for which region no vortices are pinned. The magnetic field dependence of l_s is defined by the superconducting class as it is the case for $\lambda(H)$. Quadratic dependence of $\lambda(H)$ is usual for conventional superconductors and a linearly increasing dependence of $\lambda(H)$ has been found in Bi-2212 superconductors [92]. Consequently, the dependence of l_s on H can be written as [71]:

$$l_s(H) = l_{s0} + (R - l_{s0})(H/H_{irr})^{\beta}, \tag{5.4}$$

l_{s0} is the value of l_s at $H = 0$ and H_{irr} is the irreversibility field. β is a positive dimensionless coefficient, with $\beta \geq 1$. When $\beta = 1$, equation (5.4) can be simplified to equation (2.80). The surface layer depth l_s is assumed to be equal to λ, thus $l_{s0} \approx \lambda_0$. Averaging over the sample area, the J_c dependence on the depth of surface layer l_s has been described in equation (2.82). For the porous nanowire network, the effective superconducting region are taken into account,

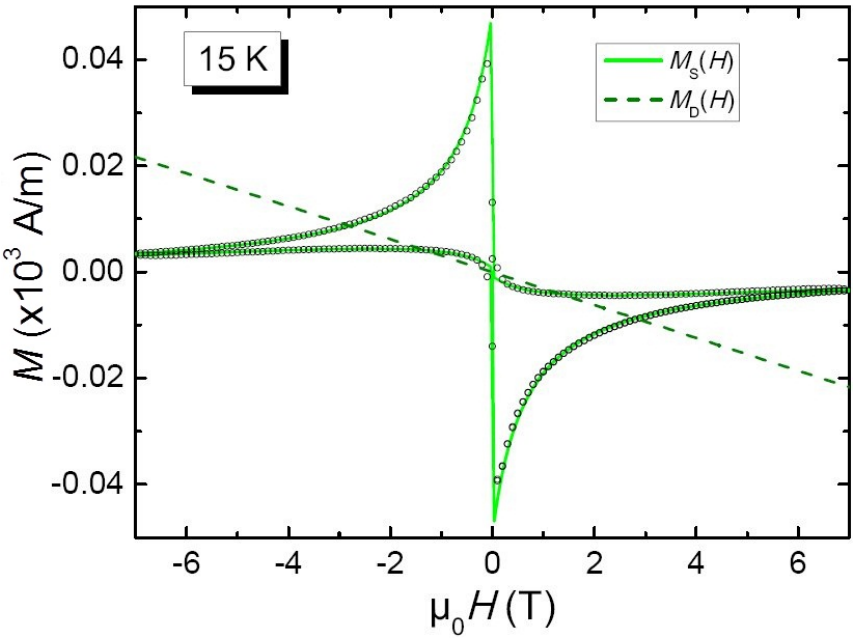

Figure 5.19: Superconducting M_s and diamagnetic M_D magnetizations of the non-doped Bi-2212 nanowires network at 15 K. The dash line represents diamagnetic background M_D; the circular spots represent the experimental data, after a subtraction of background M_D. The line represents the computed curve M_s [71].

then the expression is modified to [71]:

$$J_c(H) = P_s j_c(H)[1 - l_s(H)/R]^n, \tag{5.5}$$

here $j_c(H)$ is the local critical current density, which can be obtained from equation (2.78), n is an index defined by the geometry of the grain, with $n = 3$ for long cylindrical grains. In combination with equation (5.4), equation (2.78) can be rewritten as

$$j_c(H) = \frac{j_{c0}\left[1 - (H/H_{irr})^{\beta}\right]^3}{(\mu_0 H/B_1)^{\gamma} + \exp(\mu_0 H/B_2)}. \tag{5.6}$$

The definition of B_1, B_2 and γ are given in the description of equation (2.78). In this work, the measurements are accomplished in the condition $H \ll H_{c2}$. The critical current density dependence is in good agreement with the Anderson-Kim relationship ($j_c \sim 1/B$) [34]. Therefore, it can be reckoned that $B_2 \gg \mu_0 H$. Furthermore, the fitting parameters for the $M_s(H)$ loops should satisfy the following requirements:

1. The $j_c(B)$ dependence decreases from j_{c0} at $B = 0$ to 0 at $B \geq B_{c2} = \mu_0 H_{c2}$;
2. The $l_s(H)$ dependence increases from l_{s0} at $H = 0$ to R at $H \geq H_{irr}$, where the magnetization loops become field reversible. R is the radius of

the current circulation at high H.

With certain conditions, the expression of the critical current density dependence can be rewritten as [71]

$$j_c(B) = j_{c0}\frac{1-|B/B_{c2}|^{\alpha}}{1+|B/(h_1 B_{c2})|^{\alpha}}, \tag{5.7}$$

where α and h_1 are positive dimensionless coefficients with $\alpha \leq 1$, while $h_1 \ll 1$.

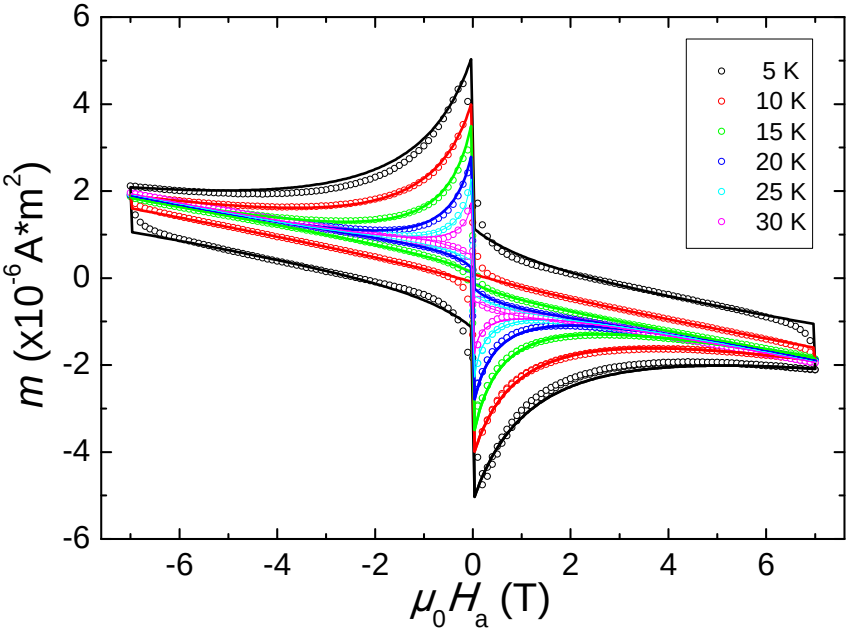

Figure 5.20: $m(H)$ loops of the non-doped Bi-2212 nanowire network. The points represent the experimental data, and the solid lines are computed curves by ECSM [71].

The $m(H)$ at different temperatures are computed by ECSM for the case of a long cylindrical sample with radius R, as shown in Fig. 5.20. Widths of the loops were fitted by $j_{c0} \times R$ and the asymmetry with respect to the $m = 0$ axis is fitted by l_{s0}/R. The average nanowire radius of ∼160 nm obtained from SEM images was used as the R value. This value is smaller than the known λ of Bi-2212 (∼ 269 nm [93]). On the other hand, the polycrystalline characteristics results to a high asymmetry of the $M_s(H)$ loops. The fitting parameters at different temperatures are presented in table 5.2. All $M_s(H)$ curves are computed with $h_1 = 0.02$, $\alpha = 0.63$. The parameter β is used for fine tuning of the fitting curves. It is equal to 1 for most curves, at lower temperatures a better fit is reached with the value of $\beta = 1.2$ at 5 K and at 10 K. Checking the estimated value of H_{c2} in table 5.2, the values are far higher than the applied field in the measurement (7 T). This is in good agreement with the initial hypothesis that $B_2 \gg \mu_0 H$. Additionally, the penetration field H_p is computed. The value of H_p is slightly smaller than the product of j_{c0} and R, which is equal to the penetration field in the Bean model. The temperature

dependences of H_{c2}, H_{irr} and H_p together with $j_{c0}(T)R$ are plotted in Fig. 5.21. The temperature evolution of the H_{irr}/H_{c2} is shown in the inset to Fig. 5.21. The temperature dependence of H_{irr} of the present sample is similar to other Bi-2212 materials investigated in the literature [97].

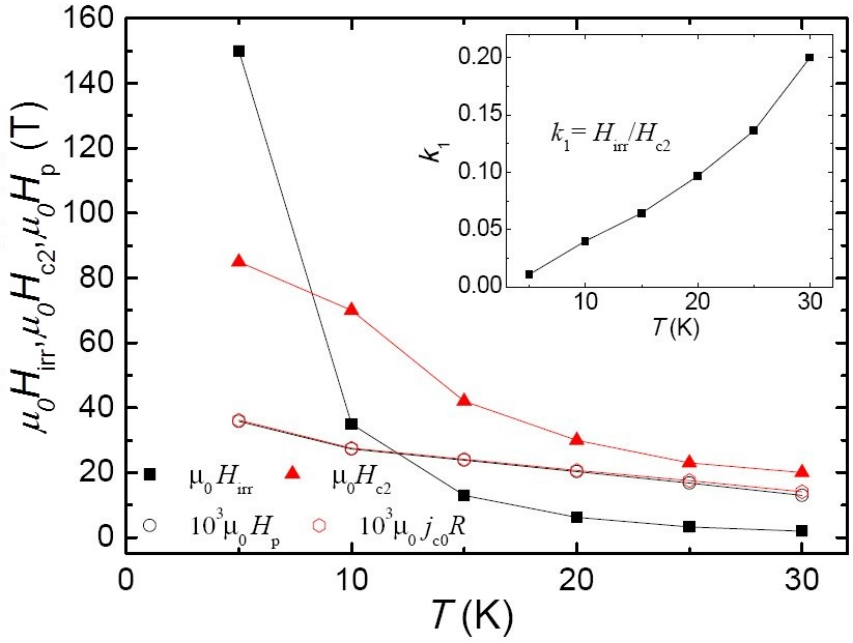

Figure 5.21: The upper critical field H_{c2}, the irreversibility field H_{irr}, and the penetration field H_p at different temperatures. The inset displays the temperature dependence of H_{irr}/H_{c2} [71].

The values of intragrain critical current density (or average critical current density) $J_c(H)$ can be calculated from the local current density $j_c(H)$ by equation (5.5). Expressing J_c at $H = 0$ as $J_{c0} = P_s j_{c0}(1 - l_{s0}/R)^n$, the $J_c(H)$ dependence of the ECSM can be written as [71]:

$$J_c(H) = J_{c0} \frac{1 - |H/H_{c2}|^\alpha}{1 + |H/(h_1 H_{c2})|^\alpha} (1 - |H/H_{irr}|)^\gamma, \tag{5.8}$$

where $\gamma = \beta \times n$. $J_c(H)$ decreases faster than $j_c(H)$ and tends to reach 0 as soon as H approaches $H_{irr}(T)$. The dependence of $J_c(H)$ presented in Fig. 5.22 is calculated by using j_{c0} and l_{s0}/R given in table 5.2 and $n = 3$. The calculated values of J_{c0} are listed in table 5.2. In the same temperature range, the J_{c0} values of this porous nanowire network decrease from 10.4×10^6 A/cm^2 to 2.5×10^6 A/cm^2, similar to the intragrain critical current densities of the Bi-2212 whiskers [98]. Meanwhile, these values are much larger than the critical current density of Bi-2212 wires [99] which is strongly limited by the grain boundaries. As a comparison, $J_c(H)$ is estimated from the width of the magnetization loops ΔM by the Bean formula $J_c(H) = 3\Delta M/(2R)$. The porosity is not taken into account, therefore, the resulting value should be multiplied by $1/P_s$. The $J_c(H)$ dependence resulting from the Bean model is presented by the dotted line in

T (K)	j_{c0} (10^6 A/cm^2)	l_{s0}/R	$\mu_0 H_{c2}$ (T)	$\mu_0 H_{irr}$ (T)	J_{c0} (10^6 A/cm^2)	$\mu_0 H_p$ (mT)
5	16.9	0.15	85	∼80	10.4	35.8
10	13.7	0.19	70	35	7.3	27.3
15	12.0	0.205	42	13	6.0	23.8
20	10.3	0.225	30	6.2	4.8	20.3
25	8.75	0.25	23	3.3	3.7	16.8
30	7.0	0.29	20	2	2.5	13.0

Table 5.2: Fitting parameters and estimated values of ECSM. The critical current density j_{c0} determines the width (ΔM) of the magnetization hysteresis. The depth of the surface layer with equilibrium magnetization l_{s0} determines the hysteresis asymmetry relative to the H axis. H_{c2} gives the rate of decrease for $j_c(B)$, and H_{irr} gives the rate of increase for $l_s(H)$ [71].

Fig. 5.22. For a given radius of $R = 160$ nm, the Bean model estimations are in good agreement with the computed data of ECSM. The reason for this quantitative coincidence is the same influence of the surface on the macroscopic critical current and on the irreversible magnetization ΔM. The Bean model establishes the relation between the irreversible magnetization $\Delta M(H)$ and the $J_c(H)$ dependence. The $J_c(H)$ of smaller samples decreases faster than the

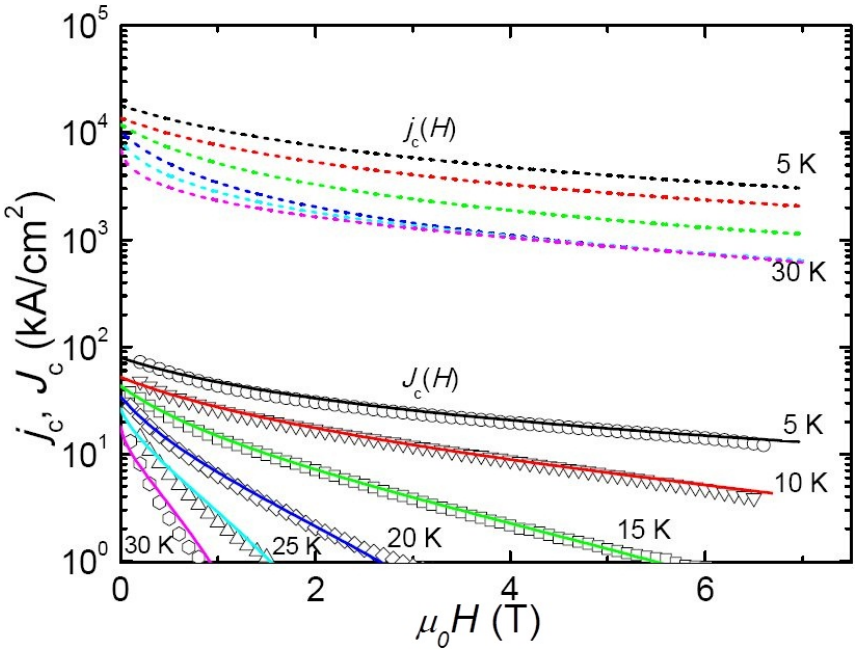

Figure 5.22: The dependence of the intragrain critical current density on the magnetic field. The lines are ECSM curves. The points are the critical current density obtained from evaluating the width of the experimental $M(H)$ loops using the Bean formula [71].

$J_c(H)$ of larger samples, due to omitting the surface region with field-dependent depth $l_s(H)$. The irreversible magnetization of smaller samples also decreases faster than ΔM of the larger samples. As the numerical calculation display, the dependences $J_c(H)$ and $\Delta M(H)$ decrease simultaneously and are both equal to 0 at $H > H_{irr}$. Ignoring the consideration of the magnetization of a porous, polycrystalline superconductor, an equivalent superconducting sample, whose radius is equal to the average nanowire radius is considered instead. With this simplification, the Bean model can be used to estimate the J_c values of porous, polycrystalline superconductors.

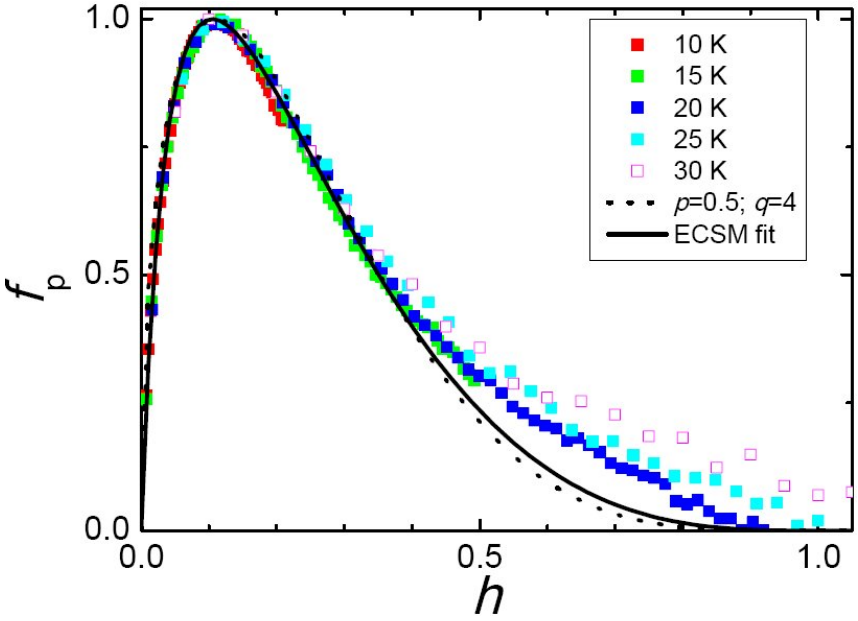

Figure 5.23: Scaling of the normalized pinning force $f_p = F_p/F_{p0}$ vs. the reduced field $h = H/H_{irr}$. The data points are obtained from the width of the experimental loops (Bean formula). The solid line is the ECSM fitting curve for $T = 15$ K; the dotted line gives the DH function with p = 0.5 and q = 4 [71].

The dependence of the pinning force density on the applied magnetic field is determined by the definition $F_p(H) = \mu_0 H \times J_c(H)$. In Fig. 5.23, the normalized pinning force $f_p = F_p/F_{p0}$ (F_{p0} is the maximal pinning force density at a given T) is plotted as a function of the reduced field $h = H/H_{irr}$ for different T. The solid line represents the $f_p(h)$ dependence computed by ECSM using equation (5.8) and the parameters from table 5.2. The estimation from the Bean model is plotted as spots in Fig. 5.23. For the purpose of further comparison of the results, the scaling law of Dew-Hughes (DH) is used to fit the $f_p(H)$ dependence [94]:

$$\frac{F_p(H,T)}{F_{p0}(T)} = \left(\frac{h}{h_0}\right)^p \left(\frac{1-h}{1-h_0}\right)^q, \tag{5.9}$$

where h_0 is the position of the maximum of f_p, $h_0 = p/(p+q)$. The maximum flux pinning is found at $h_0 \approx 0.11$ for all T, which is smaller than the typical result of the Bi-2212 samples of $h_0 = 0.2$. Following the analysis of Eisterer [95], this reflects the influence of anisotropy and percolation. The nanowires are polycrystalline without a specific texture of the grains, so the supercurrents flowing within a nanowire have to pass grains with different orientations and numerous interconnections between the nanowires, forming a percolation network. An anisotropy which is larger than 4 yields a position of $h_0 = 0.1$ for the grain boundary pinning, which is certainly fulfilled for Bi-2212. In contrast, the influence of percolation effects on the peak position is much smaller. The scaled curves are fitted with $p = 0.5$ and $q = 4$. These values differ from the Kramer parameters ($p = 0.5$ and $q = 2$), which indicates the anisotropic and polycrystalline characteristics of the Bi-2212 nanowire network sample [95, 96].

5.2.3 Electric properties of $Bi_2Sr_2CaCu_2O_8$ nanowires

According to the former analysis, the polycrystalline Bi-2212 nanowires consist of superconducting grains and non-superconducting grain boundaries. Therefore, the current flow in the nanowires has to pass through the superconductor-insulator-superconductor connection, in other words, the intergranular electron transportation is based on the intrinsically forming Josephson junctions. In previous [100] it has been discussed that the connections between grains (intergrain connections) and nanowires (weak-link connections) must be taken into account. Therefore, the Bi-2212 nanowire network should be treated as a RCSJ network. Figure 5.24 presents the RCSJ model incorporating Josephson junctions between superconducting grains. The electric properties of the Bi-2212 nanowire network are characterized by the four-probe measurement. In order to enhance the contact quality, 100 nm Au was coated between the sample and the electrodes (The influence of Au to superconductivity is discussed in the next section). Figure 5.25 shows the $U(I)$ measurement of the non-doped Bi-2212 nanowire network at various temperatures ranging from 18 K to 100 K. It can be found that from 18 K to 71 K, the curves can be separated into two regimes with different slopes. They can be defined as the superconducting regime and the normal state regime respectively. The superconducting regime shows an obvious tilting. This indicates high residual resistance. This result is in good agreement with the RCSJ model demonstrated in Fig. 5.24. Above 85 K, the curves become linear. This indicates that the sample reaches T_c at around 85 K. Unlike the bulk or thin film superconductors, the hysteretic effect is not as strong as in the nanowire network. This can be explained by the static heat effect [101]. With a thinner diameter of the nanowire, the hysteretic effect would be weaker. Due to the influence of the residual resistance, the values of the critical current $I_c(T)$ can not be simply estimated from the x-intercept of the $U(I)$ curves. The I_c value of each $U(I)$ curve is evaluated by the crossing point of the tangent lines on the superconducting regime and normal regime. The $I_c(T)$ increases with decreasing temperature from 0.072 A to 0.172 A (0.072

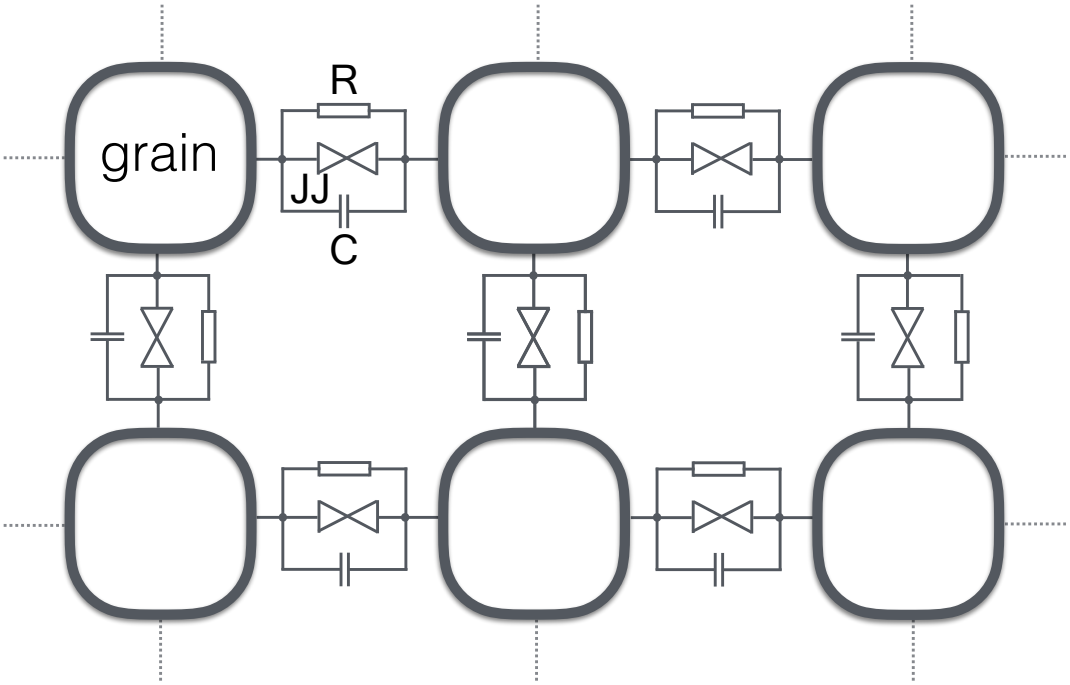

Figure 5.24: The RCSJ model of the polycrystalline nanowire network (R: resistor, C: capacitor and JJ: Josephson junction) [100].

A at 71 K, 0.101 A at 60 K, 0.126 A at 50 K, 0.147 A at 33 K, 0.172 A at 18 K).

Figure 5.26 presents the $R(T)$ measurement results at different fields ranging from 0 T to 10 T. The applied current is 50 µA. Strong field dependence of the resistance and a stepwise resistance behavior are observed. The first drop in resistance stems from the phase transition of the grains from normal to superconducting state. As shown in Fig. 5.24, when the grains become superconducting, the total resistance of the whole network system decreases, leading to the first resistance drop similar to bulk superconductors. The onset temperature of the first resistance drop at 0 T is around 84 K, corresponding to the T_c estimation from the $U(I)$ curves. On the other hand, the resistance drop is not as sharp as the one in the bulk superconductors. It turns out that an exponential expression $\exp(-\Delta F/k_B T)$ matches the $R(T)$ regimes around T_c, as shown in the highlight red regimes in the inset to Fig. 5.26a. Therefore, the broadening of the resistance drop around T_c can be attributed to either the thermally activated phase slip or the thermal activation of flux flow (TAFF). Both effects originate from the thermal fluctuation of the system and ΔF is the energy required to locally suppress superconductivity in TAPS or the pinning potential in TAFF. In order to find out whether TAPS or TAFF is dominating the resistance behavior around T_c, it is necessary to clarify the dependence of $\Delta F(T)$.

In the case of TAPS, $\Delta F(T)$ follows the temperature dependence $\Delta F(T) \approx \Delta F(0) \times (1 - T/T_c)^{3/2}$ [102]. $\Delta F(T)$ extracted from the data of non-doped

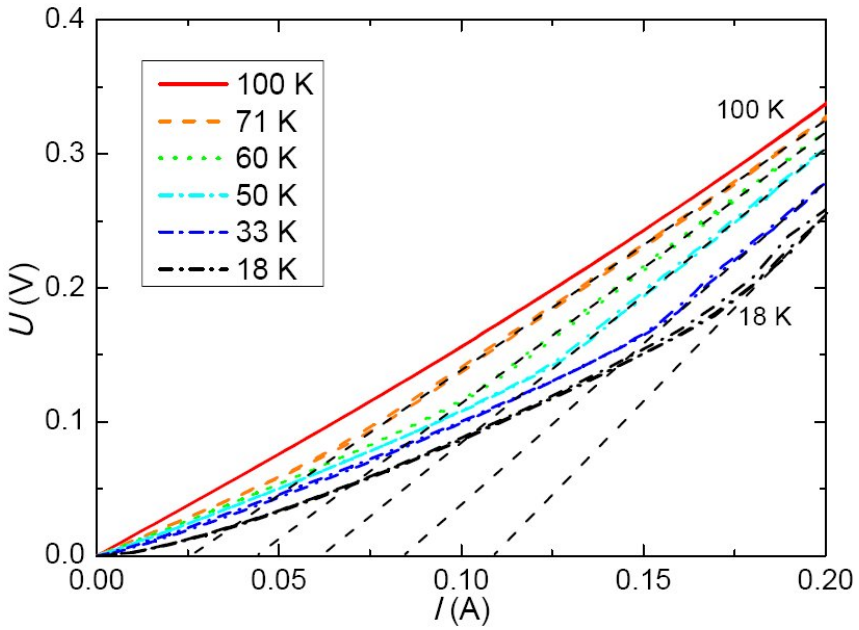

Figure 5.25: U/I characteristics of the non-doped Bi-2212 nanowire network measured at various temperatures between 18 K and 100 K [70].

Bi-2212 nanowire network is in good agreement in the temperature dependence as mentioned above, where $\Delta F(0) = 27.2$ meV at 0 T. Tinkham demonstrated the relationship between $I_c(T)$ and $\Delta F(T)$ for TAPS [103]:

$$\Delta F(T) = \frac{4}{3a}\left(\frac{\hbar}{2e}\right) I_c(T). \tag{5.10}$$

From the comparison of the $I_c(T)$ data and the result of the $\Delta F(T)$ from

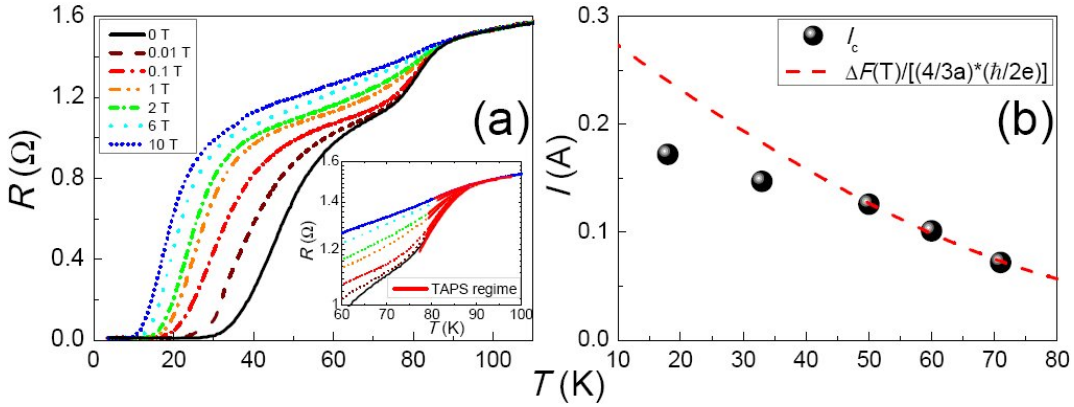

Figure 5.26: (a) Resistance R as function of temperature T measured in fields from 0 T to 10 T, the inset shows a fit (bold lines) to the data by the TAPS model; (b) A comparison of $I_c(T)$ and the curve $\Delta F(T)/\left[\frac{4}{3a}\left(\frac{\hbar}{2e}\right)\right]$ [70].

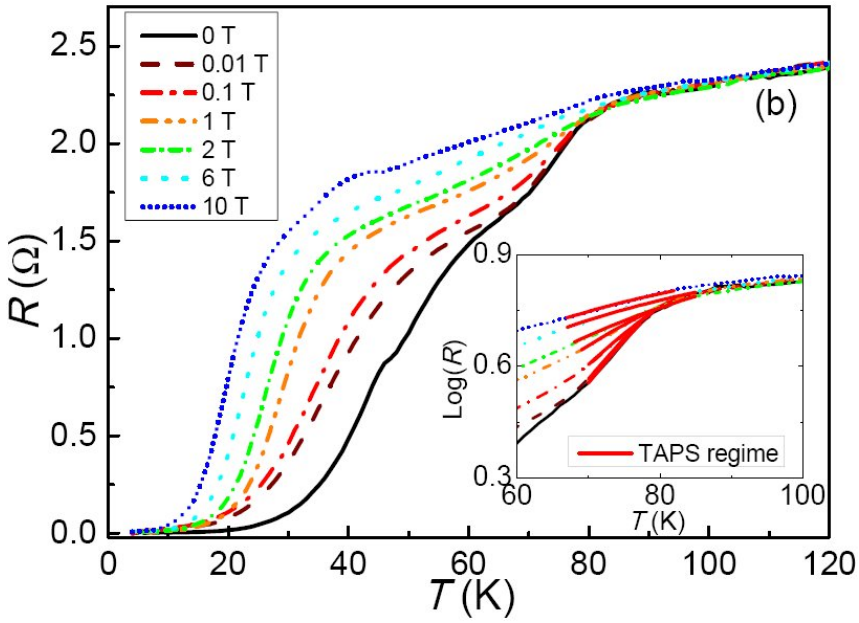

Figure 5.27: $R(T)$ curves of the Pb-doped Bi-2212 nanowire network measured in fields from 0 T up to 10 T, the inset shows a fit (bold lines) to the data by the TAPS model [72].

the fitting, it can be seen in Fig. 5.26b that $\Delta F(T)$ matches the $I_c(T)$ data above 50 K, which certifies the contribution of TAPS to the sample. Since TAPS and TAFF can only be used to explain the resistance behavior around T_c, it is valid to find the deviation between $\Delta F(T)$ and $I_c(T)$ below 50 K. In equation (5.10), a is a constant of order unity. In this fitting, the value of a is 2.72×10^4, which is much larger than the result of Ref. [102]. Their nanowires were fabricated by e-beam lithography with a superconducting thin film. The granular effect stems mainly from the fixed grain boundaries. Therefore, less inner stress can be induced by an external magnetic field and the resistance does not vary as much with the field. In contrast, the nanowire network is much more sensitive to the applied field due to numerous grain boundaries and interconnections between the individual nanowires. Furthermore, the critical currents of the nanowire networks are 1000 times higher, which may explain the difference in a. After the first drop, the resistance does not reach zero immediately, a non-zero resistance appears at the second step in the resistance curve (ranging from 40 to 80 K at 0 T). In this regime, the resistive behavior of the Josephson junctions is dominating. The supercurrent can not directly pass through the grain boundaries and the weak-links between the individual nanowires. As a result, the electron scattering induces a normal state resistance in the $R(T)$ curve. At lower temperature, part of the supercurrent goes through the Josephson junctions, leading to the second drop of the resistance. At very low temperatures near 4 K, the resistance is small but non-zero, which can be related to the scattering of the charge carriers at the grain boundaries.
Similar behavior can be found in the Pb-doped Bi-2212 nanowires as shown in

Fig. 5.27. The onset temperature of the first resistance drop is at around 78 K at 0 T, indicating that the T_c of the Pb-doped sample is 78 K. The regimes around T_c can be fitted by the exponential expression like the non-doped Bi-2212 nanowires, indicating the existence of the TAPS influence in the Pb-doped Bi-2212 nanowires. It denotes that when the sample size decreases to ∼300 nm, the TAPS should be taken into account for the analysis of the resistance behavior.

5.2.4 Influence of metal coating layers on superconducting nanowires

According to the magnetization data, the T_c of the non-doped Bi-2212 sample is 76 K, however, the estimated T_c from the $R(T)$ curve is 85 K. The 9 K enhancement can be attributed to the influence of the Au coating layer. Figure

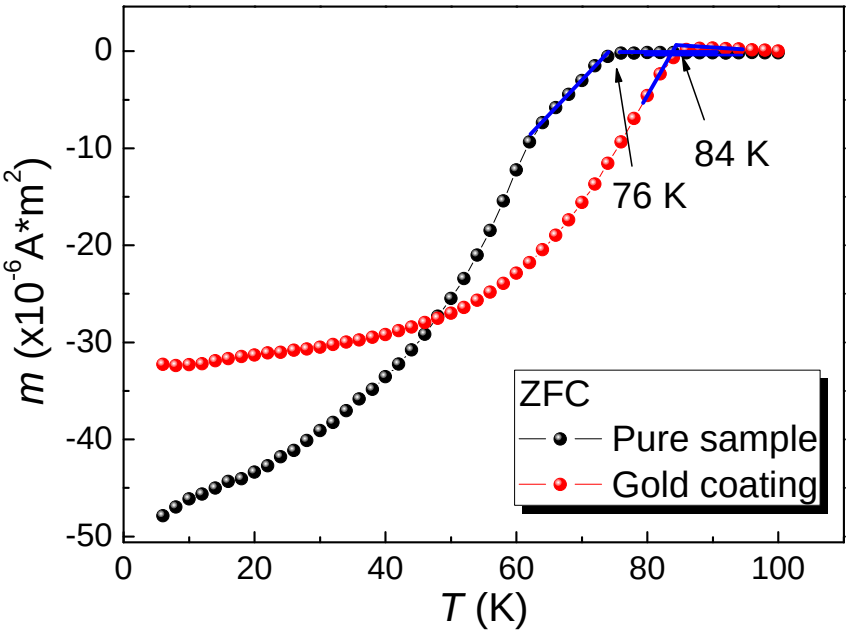

Figure 5.28: $m(T)$ measurements of the non-doped Bi-2212 nanowires before and after the Au coating [72].

5.28 presents the $m(T)$ dependence of the non-doped Bi-2212 nanowires before and after 100 nm Au coating. The difference between the two T_c shown in the graph certifies the Au contribution on the enhancement of T_c to the nanowires. For the Pb-doped sample, the 0 T curve shows a T_c around 78 K. It is lower than the one obtained from the $m(T)$ curve (84 K). Recalling the $m(H)$ behavior of both types of Bi-2212 nanowires, at 70 K, the non-doped nanowires maintain superconductivity while the Pb-doped nanowires only present a paramagnetic behavior as shown in the inset graphs of Fig. 5.12b. Furthermore, the $m(T)$ dependence of the non-doped sample starts to become field reversible at 70.2 K which corresponding to the $m(H)$ behavior while the $m(T)$ dependence of the Pb-doped sample becomes field reversible at a much lower temperature, 62.7 K. This indicates that the 'real' T_c of the Pb-doped nanowire network is lower

than 70 K. That means actually both the non-doped Bi-2212 nanowire network and the Pb-doped Bi-2212 nanowire network present T_c enhancement after Au coating.

One of the well-known effects of metal layer influence on superconductivity is the proximity effect [104]. When a superconductor is contacted with a thin layer of non-superconducting metal, the superconductivity is suppressed leading to a decrease of T_c. In a superconductor, the electrons are paired up within the coherence length. On the other hand, the electrons in a normal metal are in a single-electron state. The electron order cannot abruptly change into the other order at the interface between the superconductor and non-superconducting metal. The Cooper pairs around the interface have a high possibility of losing their coherence due to the scattering event on electrons from the metal region. This is the origin of the proximity effect.

The Au layer should have weakened the superconductivity of the sample, as the applied current from the electrode has to pass through the Au layer before entering the superconducting sample. According to the proximity effect, the T_c of the sample with Au coating should be lower than the original one. However, the opposite seems to be the case of the experimental result. The sample with 100 nm Au coating presents a T_c 9 K higher than the one without Au coating. Therefore, the influence of Au here cannot be simply interpreted by the proximity effect. As it has been mentioned before, the nanowire network system should not be treated as a normal superconductor. It is a complicated

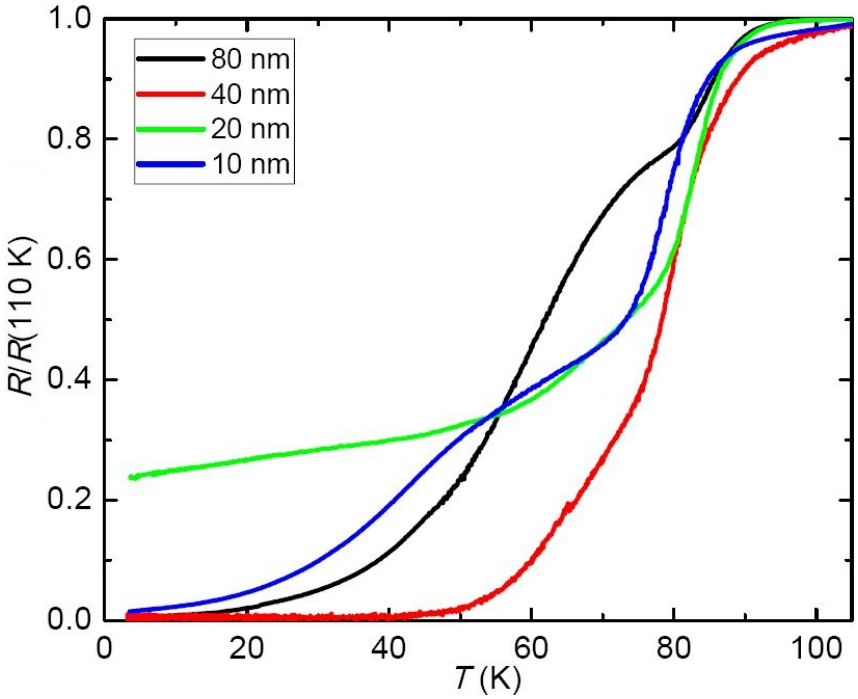

Figure 5.29: Normalised $R(T)$ curves of the non-doped Bi-2212 nanowires coated with 10, 20, 40, 80 nm thick Au layers at 0 T [100].

network system connected by Josephson junctions. In the electric measurement, the strong phase fluctuations (e.g. thermal fluctuation) provide a retardation of the formation of the global superconductivity. This is also one of the reasons why the T_c of the nanowire network is lower than that of bulk materials. The Au layer enhances the Josephson coupling of the whole system. This leads to an enhancement of the phase stiffness. As a result, this counteracts the influence of the phase fluctuations and provides a higher T_c to the Au coated nanowire network [105].

To investigate the influence of the Au coating layer on the electric properties of the nanowire network, a comparison between the $R(T)$ curves of the non-doped Bi-2212 nanowires with various thicknesses of Au coating layers was made. As shown in Fig. 5.29, there is no monotonous variation of the electric properties with increasing Au coating thickness. With 40 nm Au coating, the sample presents the highest T_c, the first and second step of the resistance nearly merge. This denotes that 40 nm may be the optimal value of the Au coating layer thickness. The Au layer significantly enhances the Josephson coupling and improves the superconductivity of the sample. Samples with 10, 20 and 80 nm thick Au layers have nearly the same T_c. The second resistance drop of the $R(T)$ curve of the 80 nm Au sample appears at around 63 K which is similar to the one with 100 nm Au coating, while the one from the 10 nm Au sample appears at a much lower temperature, around 47 K. This indicates that the 10 nm Au induces phase stiffness and increases the T_c of the nanowires, but the coupling effect is not as strong as it is in nanowires with thicker Au layers. The sample with 20 nm Au coating is precarious, above 50 K, the resistance behavior of the 20 nm sample is similar to the 10 nm sample, whereas the resistance shows no obvious drop even below 40 K. Further investigation of this feature is required.

Since the thickness influence of an Au layer on the superconductivity of the nanowire network has been specifically investigated, it is interesting to further investigate the influence of the ultrathin metal layer. The non-doped Bi-2212 nanowires were coated with Au in the sputtering machine with a deposition rate of 3.3 Å/sec. For comparison, two samples were chosen to be coated with Ag with a deposition rate of 4.2 Å/sec. Figure 5.30 presents the $m(T)$ measurement results of the non-doped Bi-2212 nanowires with different thicknesses of Au and Ag. The T_c dependence on the thickness is presented in Fig. 5.30e. When the coated layer gets thinner than 10 nm, the Au does not provide an enhancement of phase stiffness to the nanowires. The sample with around 1.7 nm Au coating possesses a T_c similar to the one without any Au coating. With this thickness, the Au coating provides nearly no influence to the T_c. With less than 10 nm Au, the suppression of the superconductivity of the nanowire increases with increasing thickness of the Au coating layer. On the other hand, even though the samples present lower T_cs with Ag coating, their T_cs increase with the thickness of the Ag layer.

One of the possible reasons for this result is that below 10 nm, the coating metal forms separate islands instead of a continuous layer. The coupling effect

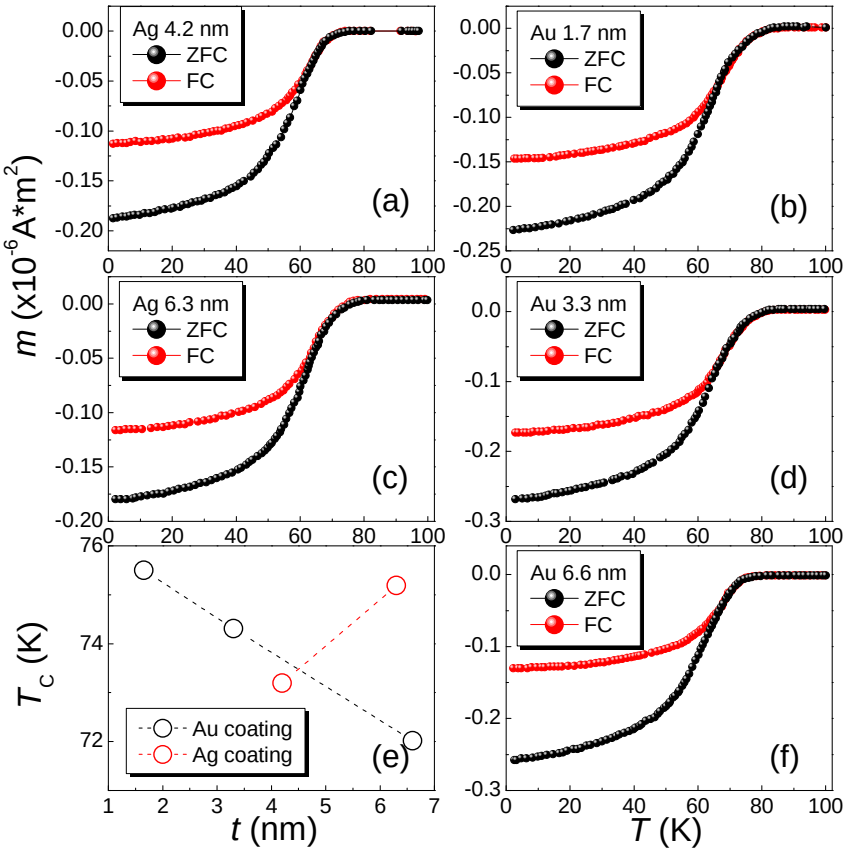

Figure 5.30: $m(T)$ results of the non-doped Bi-2212 samples with different thicknesses t of Ag layer ((a), (c)) and Au layer ((b), (d), (f)), (e) presents the T_c dependence on the thickness of the coating layer.

of Au is weaker than that of Ag. When the Au is not a continuous layer, it loses the coupling function. As a result, the superconductivity of the nanowires is weakened by the Au layer due to the proximity effect, while the Ag provides stronger coupling, therefore, it attempts to recover the superconductivity with an increasing thickness.

5.2.5 Li-doped $Bi_2Sr_2CaCu_2O_8$ nanowires

According to Fig. 4.12, the Bi-2212 phase starts to form at around 600 °C. However, no matter an increase of the amount of excessive element Cu and Ca or modifying the Pb doping level, the electrospun nanowires are not able to obtain the Bi-2212 phase below 800 °C. 800 °C is a high treatment temperature for electrospun nanowires, especially for BSCCO precursors. In the former synthesis, the obtained as-prepared nanowires have an average diameter of ∼800 nm, and they shrink to 200-300 nm after the thermal treatment. With certain thickness, the fibers maintain the wire structure, but the average length decreases dramatically from centimeter scale to micrometer scale.
For the non-doped Bi-2212 and the Pb-doped Bi-2212, both types of nanowires

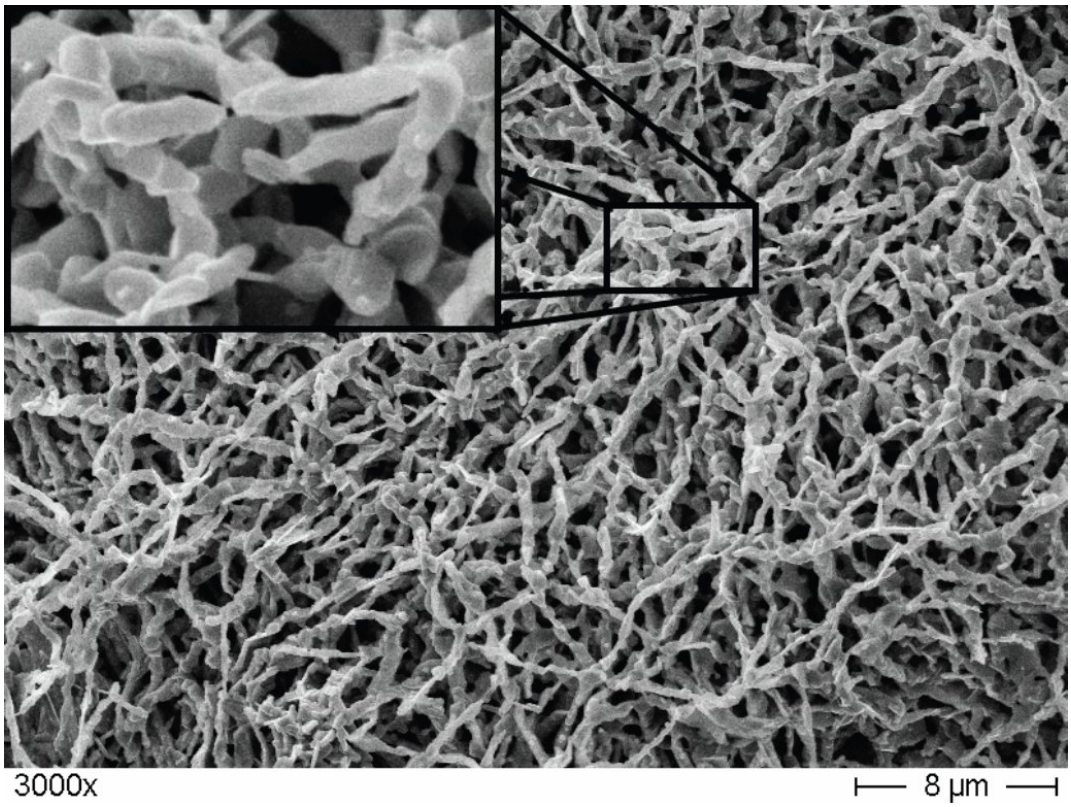

Figure 5.31: SEM image (magnification 3000x) of the Li-doped Bi-2212 nanowire network after the heat treatment. The inset gives a higher magnification (10000x), revealing the arrangement of the Bi-2212 grains within the nanowires [73].

have an average length of about 100 µm, and some of the nanowires are even less than 5 µm long. Once the as-prepared electrospun nanowires get thinner, the average length of the nanowires will become even shorter, which is not suitable for applications. An attempt to reduce the final treatment temperature of the nanowires while maintaining the superconducting phase becomes significant. It has been reported that a reduction of reaction temperature for forming superconducting phase can be achieved by doping with alkali metals [106, 107]. The Bi-2212 phase can be obtained at 710 - 720 °C by Li doping [108]. Therefore, it is possible to synthesize long Bi-2212 nanowires at lower annealing temperatures by Li doping. Currently, three Li doping levels: 15 %, 30 % and 45 % have been tested. It turns out that with 30 % Li doping the sample can obtain the Bi-2212 phase at 750 °C, which is 50 °C lower than the former two precursors. In Fig. 5.31, the resulting microstructure of the Li-doped nanowires is presented as an SEM image. The nanowires are typically formed by chain-like grains, which are linked together. The elliptical shape of the grains becomes more obvious in the Li-doped nanowires. The average diameter of the nanowires is ∼300 nm, and the average length of the nanowires is nearly 200 µm. It denotes that the 50°C reduction of the treatment temperature does help to

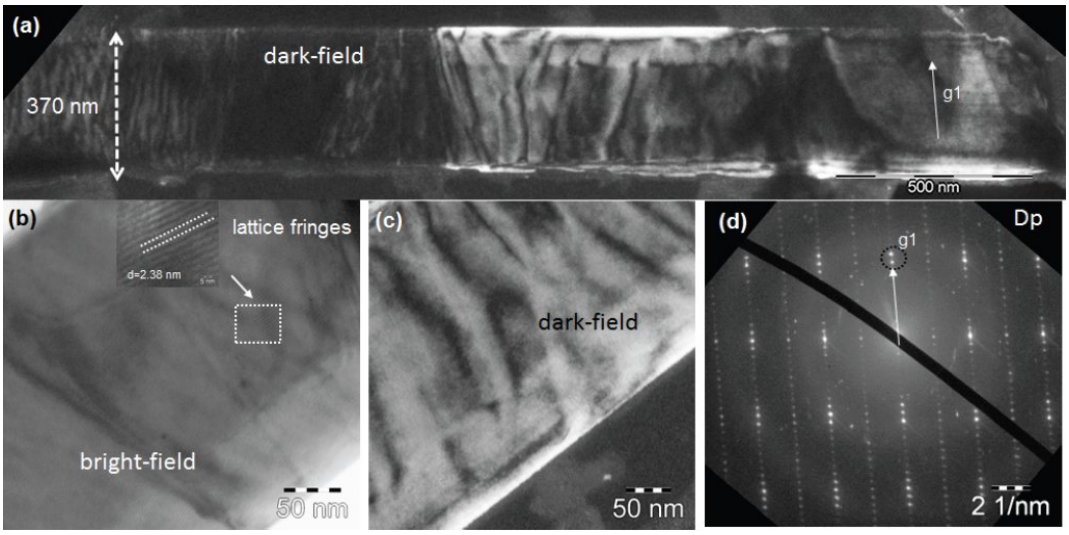

Figure 5.32: TEM investigation on an individual nanowire. (a) Darkfield image reveals the internal structure of the nanowire. Images (b) and (c) give higher magnification in brightfield (b) and darkfield modes (c). The inset to (b) shows the lattice fringes, and (d) gives the corresponding diffraction pattern [73].

maintain longer nanowires.
Figure 5.32 presents the TEM images of a Li-doped nanowire separated from the network. The width of this wire is 370 nm. Figure 5.32a reveals the internal structure within the wire consisting of randomly oriented Bi-2212 grains. Figs. 5.32b and 5.32c are high magnification images illustrating the arrangement of the grains within the nanowires. The inset in Fig. 5.32b shows the lattice fringes with a distance of 2.38 nm, which corresponds to bulk Bi-2212 [109]. Figure 5.32d confirms the well-developed crystallographic modulation within individual Bi-2212 grains. According to the XRD result shown in Fig. 4.13, the Li-doped sample has a Bi-2201 impurity phase. The EDX analysis of the selected Bi-2212 grains demonstrates that the element ratio of the chosen regime is Bi : Sr : Ca : Cu = 2.04 : 1.86 : 1.27 : 1.83, which is close to the 2212 phase. Similar results are obtained from different grains of the chosen nanowire. No information about the Bi-2201 phase is observed in the chosen regimes. This indicates that the Bi-2212 phase and the Bi-2201 phase do not coexist in a single nanowire.
Figure 5.33 presents the magnetic measurement of the Li-doped nanowires. The T_c of the Li-doped Bi-2212 nanowire network is ∼74 K, as shown in the ZFC $M(T)$ curve. This is similar to the non-doped Bi-2212 nanowires. The FC curve starts to deviate from the ZFC curve below 65 K, denoting that the field irreversibility starts from 65 K. This value is right between the one from the non-doped Bi-2212 nanowires (70.2 K) and the Pb-doped Bi-2212 nanowires (62.7 K). Similar to the non-doped Bi-2212 nanowire network, the Li-doped sample presents a paramagnetic background in the superconducting loops. This

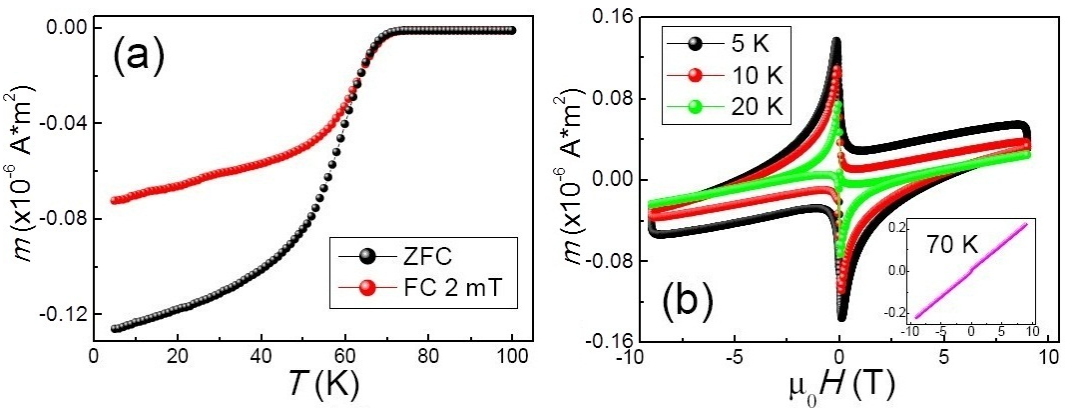

Figure 5.33: Magnetic measurement of the Li-doped nanowires: (a) ZFC and FC $m(T)$ measurements at 2 mT; (b) $m(H)$ magnetization loops at low temperatures, the inset presents a $m(H)$ loop at 70 K [73].

may be attributed to the excessive amount of element Cu and Ca in its precursor, or the Li impurity. Li^+ is a non-magnetic ion. However, it may induce the appearance of localized moments in the tetragonal phase, which destroys the 3D antiferromagnetic order as found in $YBa_2Cu_3O_x$ [110]. An influence of Bi-2201 impurities can be excluded because Bi-2201 is superconducting below 20 K. The

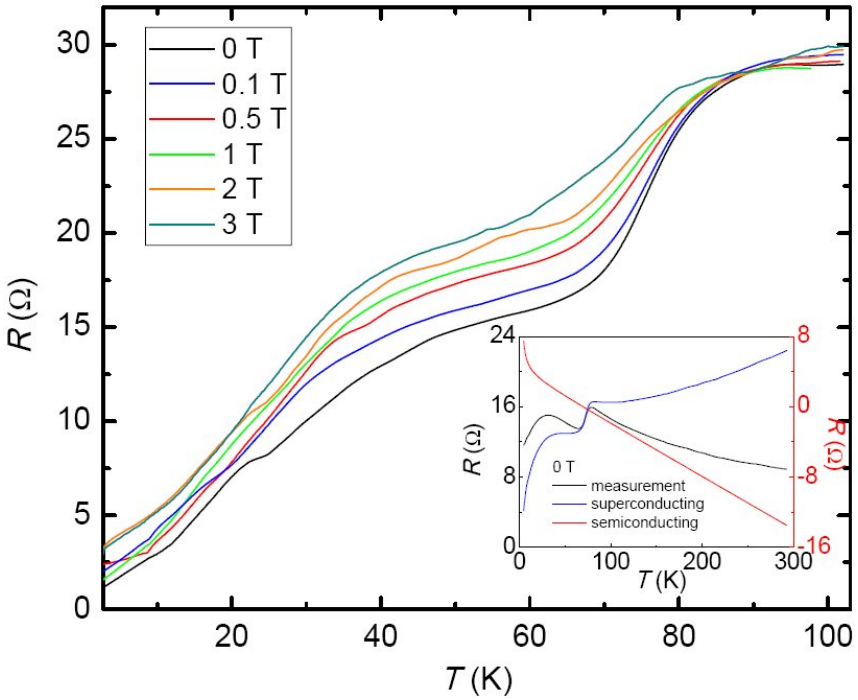

Figure 5.34: $R(T)$ measurements in various applied magnetic fields, with applied current 0.1 mA. The inset shows the $R(T)$ curve at 0 T ranging between 5 K and 290 K. The black line is the measured curve, the blue and red curves are the superconducting component and the semiconducting component, respectively [73].

inset in Fig. 5.33b shows a paramagnetic $M(H)$ loop at 70 K, indicating that the sample loses its superconductivity. This can be ascribed to the vanishing of pinning vortices above the field irreversible temperature, which was already the case in the Pb-doped Bi-2212 nanowires.
The electric properties of the Li-doped nanowires were characterized by a four-probe measurement. In order to avoid the influence of the Au layer, the electrodes were directly connected to the sample without any Au sputtering. Surprisingly, the junction resistance of the whole setup is not as strong as the former two types of Bi-2212 nanowires, the Au layer is not necessary for the Li-doped Bi-2212 nanowires. Recalling the microstructure of the non-doped Bi-2212 nanowires and the Pb-doped Bi-2212 nanowires, there are a lot of nanowires with lengths less than the average value. As a result, there are more weak-links between individual nanowires in the whole network system. They increase the resistance of the system above T_c. The Au layer provides a shrunk path for the applied current before the sample enters the superconducting state. As a comparison, the average length of the Li-doped nanowires are nearly doubled compared to the other two types of Bi-2212 nanowires. There are more wires maintaining their 'long' lengths in the network system, which decrease the weak-links between nanowires and reduce the whole system resistance. Generally speaking, for the same material, longer nanowires provide a better conductivity in the nanowire network system.
The resistance measurements are presented in Fig. 5.34. A semiconducting

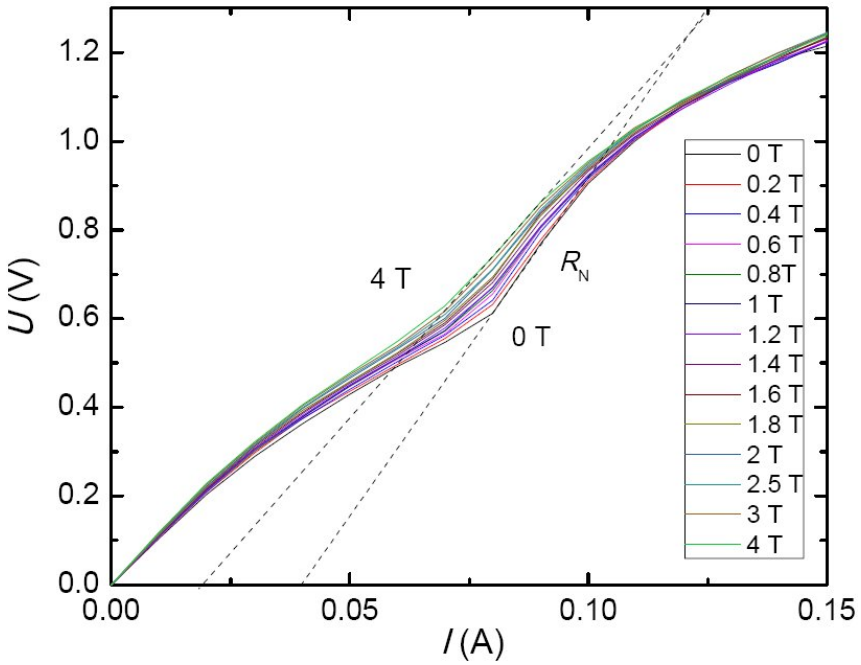

Figure 5.35: $U(I)$ characteristics of the Li-doped nanowire network measured at $T = 20$ K (positive branch) and in various applied magnetic fields. The dashed lines are linear fits to the data to determine I_c and R_N [73].

background can be observed from the $R(T)$ curve in full temperature range as shown in the inset of Fig. 5.34. The black line shows the measured data, the blue, and red lines demonstrate the superconducting and semiconducting component respectively. It can be reckoned that the semiconducting background stems from the Li impurities as its existence has been proved in the magnetic measurement. The background removed $R(T)$ curves are shown in the main graph. Similar to the non-doped Bi-2212 nanowires, a stepwise resistance behavior is observed. The resistance drop at the first step denotes the T_c is ∼80 K. This value is higher than the one estimated from the ZFC $M(T)$ curve. It may be attributed to the influence of the paramagnetic Li impurity. The non-zero resistance at the second step is not only due to the electron scattering at grain boundaries and weak-links between nanowires, but also the non-superconducting Bi-2201 phase in this temperature range. At 0 T, the second kink of the $R(T)$ curve starts at around 65 K. This coincidently resembles the field irreversible temperature. An unnoticeable step appears at ∼20 K. It can be attributed to the superconducting transition of the Bi-2201 impurity. However, thermal fluctuations around T_c induce a non-zero resistance to the sample, below 20 K, the resistance is much higher compared to the non-doped Bi-2212 nanowires.

Figure 5.35 shows the $U(I)$ characteristics of the Li-doped nanowire network in fields up to 4 T at 20 K. All the $U(I)$ curves are lying on a semiconducting background resulting from the Bi-2201 phase and Li impurity. According to the two-fluid model [111], which assumes that both the applied magnetic field and electric current are related to weak coupling effects within the constraint

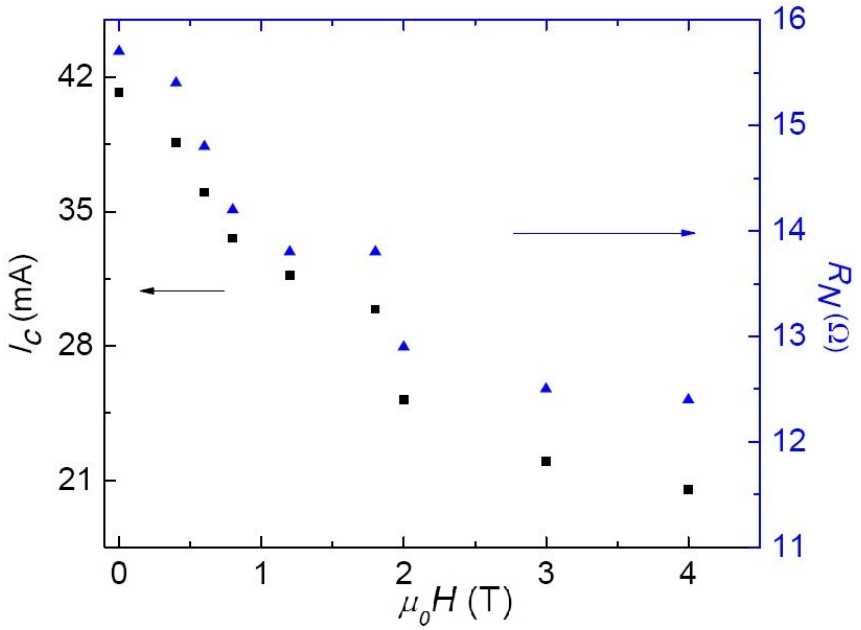

Figure 5.36: I_c and R_N as functions of the applied magnetic field, determined from the $U(I)$-characteristics at 20 K [73].

of Cooper pairs, the linear part of the $U(I)$ curve after the tilt in the superconducting regime is extrapolated linearly. The crossing point of the extrapolations between the superconducting regime and the normal state regime denotes the value of I_c. The slope of the extrapolation in normal state regime determines the normal state shunt resistance of the Josephson junctions R_N of the sample. The temperature dependence of I_c and R_N are illustrated in Fig. 5.36. I_c decreases from 41.2 mA at 0 T to 20.5 mA at 4 T. The decrease rate significantly lowers above 2 T. A similar behavior is observed for R_N, which decreases from 15.7 Ω to 12.4 Ω in the same range. Compared to the non-doped Bi-2212 nanowires, the R_N is enhanced for the doped nanowires. This is again pointing to the possible presence of Li-containing compounds at the grain boundaries considering the reports on alkali-doped superconductors [112, 113, 114].
In conclusion, Li-containing precursors can reduce the reaction temperature of electrospun Bi-2212 nanowires, which brings the desired advantage of maintaining longer nanowires. However, the payment is creating a more complicated microstructure: The Bi-2201 does not fully convert to Bi-2212 at the lower reaction temperature with the help of Li. The sample synthesized from the precursor with an additional 30 % Li and treated at 750 °C contains about 30 % Bi-2201 phase estimated from XRD data. The influence of the Li impurity and the Bi-2201 phase are found in the magnetic and electric properties as a significantly paramagnetic semiconducting background. An enhancement of the conversion rate from Bi-2201 to Bi-2212 at lower reaction temperatures is required for further optimization of the approach in order to produce nanowire samples with sufficient superconducting properties.

5.2.6 Li-doped $Bi_2Sr_2CaCu_2O_8$ mesoscopic fiber

So far, the superconductivity of polycrystalline superconducting nanowires networks has been discussed. In these nanowire network systems, the sample can not be simply treated as a homgenous superconductor but has to be considered as a complicated network consisting of numerous Josephson junctions. The stepwise resistance drop behavior is a characteristic feature of their electric properties. This feature vanishes in the thin film and bulk sample synthesized by the same precursor with consistent thermal treatment. Thus it can be reckoned that such behavior is size and shape related. With the purpose of having a further exploration, a closer examination of a single Bi-2212 nanowire was made. Since the Li-doped Bi-2212 nanowire network provides longer nanowires, this system was chosen to be the source of the single nanowire. The preparation procedure of a single nanowire setup was described in section 4.4 and Fig. 4.7. However, the single nanowire got burnt and broke easily during the measurement due to the noise fluctuation from source meter. As compensation, the investigation switched to the Li-doped Bi-2212 mesoscopic fiber. With 30 % Li doping, the precursor provides longer Bi-2212 nanowires at 750 °C, accompanied with Bi-2201 impurity. According to the EDX analysis, the Bi-2212 phase and the Bi-2201 phase do not coexist in a single nanowire. A similar

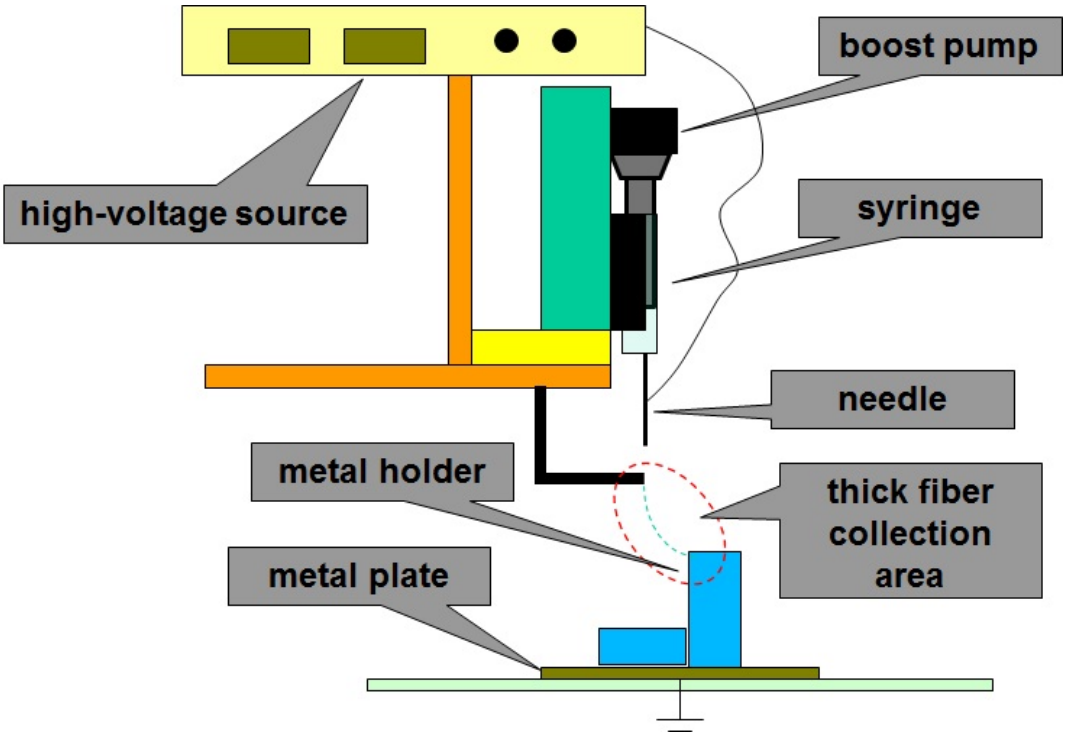

Figure 5.37: Electrospinning setup for thick fibers.

result occurs in the mesoscopic fiber system. Therefore, when investigating a single fiber with the Bi-2212 phase, the influence of the Bi-2201 phase can be ignored.

The mesoscopic fibers were obtained by modifying the electric field distribution in the electrospinning setup. Recalling the electrospinning process, before the fiber locates to the collection holder, it experiences a thinning process due to the rapid evaporation of the solvent and the elongation by the electric field. It can be separated into one straight segment and two spiral segments. The first segment experiences the least influence from the evaporation. Therefore this segment is thicker than the fiber locating on the collector far away from the needle. In order to obtain mesoscopic fibers, a steel holder was set between the original collection holder and the needle as shown in Fig. 5.37. With less distance between the holder and the needle, the electric field in between is stronger than the former setup. The region of the first segment is consequently elongated. It has been confirmed that the diameters of the fibers collected with the new setup are larger than the former one. The as-prepared fibers can reach centimeter scale as shown in Fig. 5.38a. These fibers present higher flexibility than the nanowires due to the polymer bridge and the thicker diameter. After the same thermal treatment as the nanowires, the fibers lose their flexibility, however, instead of breaking into segments as nanowires do, the fibers maintain the original structure after the whole thermal treatment. They just shrink to a smaller size as the result of the removal of the organic component. After the thermal treatment, the average length of the fibers is in the millimeter scale

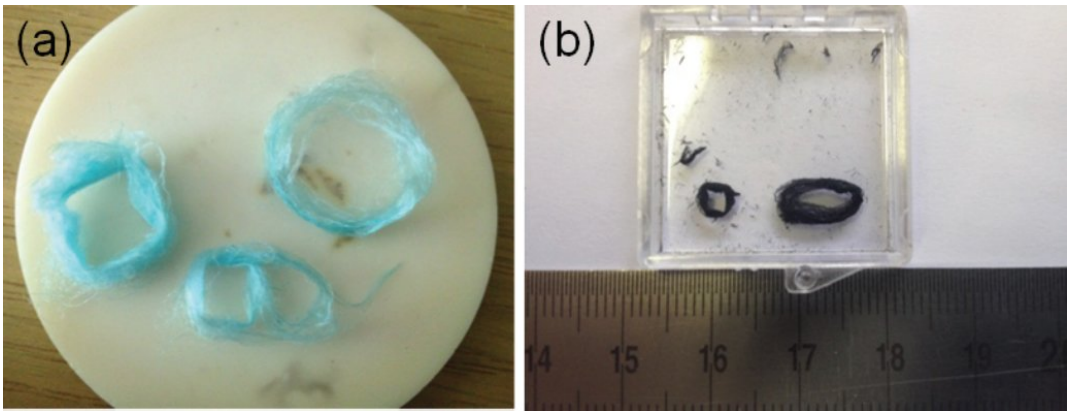

Figure 5.38: Images of the Li-doped mesoscopic fibers before and after thermal treatment [115].

as shown in Fig. 5.38b. The microscopic structure has been characterized by SEM observation as shown in Fig. 5.39. The average diameter of the fibers is around 1 µm. Since it is not in nanometer scale, these fibers should be called 'mesoscopic' fibers.
A refined element ratio analysis is applied to the fibers via a high resolution EDX detector in an aberration-corrected transmission electron microscopy (Cs-TEM, FEI Tian 80-300). With a spot size of ∼1 nm for the detector, element analysis on individual grains of the fibers is available. In this work, the grains from two chosen fibers were detected, and some features can be found from the EDX data:

1. Bi-2212 phase and Bi-2201 phase do not coexist in a single fiber. This result corresponds to the EDX analysis of the Li-doped Bi-2212 nanowires.
2. CuO appears in grains of both chosen fibers.
3. The oxidization level differs in various Bi-2212 grains within one single fiber.

The result from the EDX analysis ensures the electric measurement on a

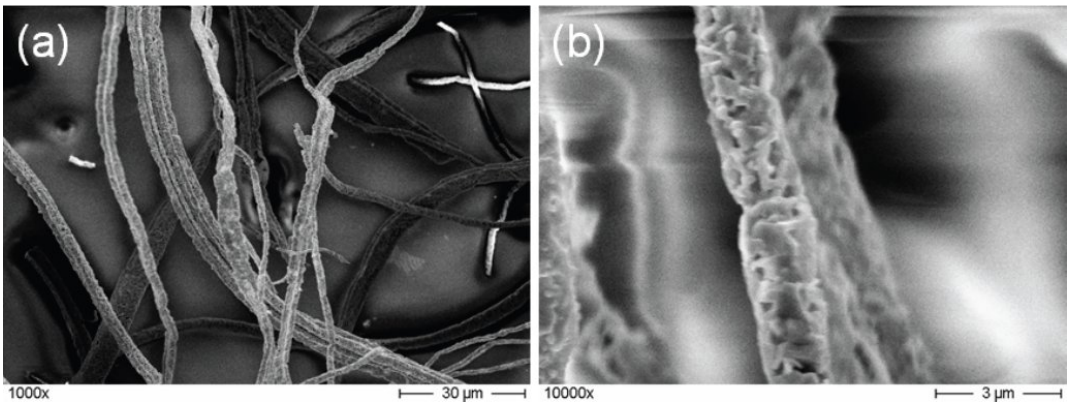

Figure 5.39: Microscopic view of the Li-doped mesoscopic fibers by SEM observation.

single Li-doped Bi-2212 mesoscopic fiber is not influenced by the Bi-2201 phase. However, the influence of CuO and different oxidization levels cannot be ignored.

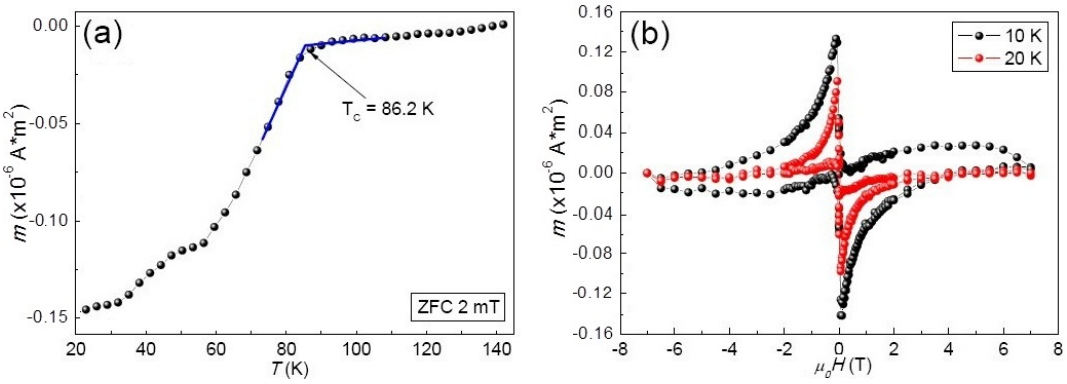

Figure 5.40: Magnetic properties of the Li-doped mesoscopic fibers measured in PPMS.

Figure 5.40 presents the magnetic properties of the Li-doped mesoscopic fibers measured in a physics properties measurement system (PPMS). The Li-doped mesoscopic fibers present a higher T_c (86.2 K) in the ZFC $M(T)$ curve. The T_c is higher than the one of the nanowires (74 K). In the $M(H)$ loops at 10 K and 20 K, there is no obvious paramagnetic background as in the nanowires. This denotes that the signal from the superconducting fibers is strong enough

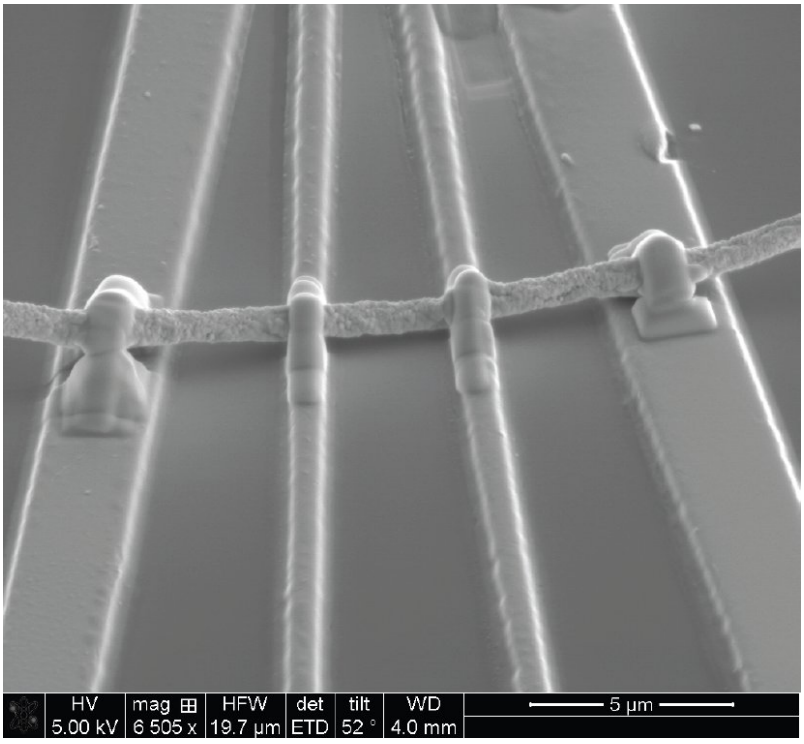

Figure 5.41: 45° view of the Li-doped fiber connected to the electrodes in FIB.

to suppress the signal of the non-superconducting ingredients. On the other hand, the magnetization loops of the mesoscopic fibers are different from the traditional superconducting hysteresis loops. An arch appears at the high field regime, where there is expected to be a horizontal area with respect to the axis $M = 0$. Similar cases appear in the non-doped Bi-2212 nanowires and the Pb-doped Bi-2212 nanowires in low field regimes. This is called the fishtail effect. It indicates an underlying increase of pinning at high fields, which can be attributed to the transition of the vortex lattice [116] or the phase separation [117]. The order-disorder transition of the vortex lattice mainly happens when the temperature approaches T_c, therefore it is not valid in case of the mesoscopic fibers. Because the fishtail effect is strong at 10 K rather than 20 K. It is confirmed from the EDX data that the grains in the Bi-2212 fiber can be classified into three types: CuO grains, weakly oxidized Bi-2212 grains, and highly oxidized Bi-2212 grains. This means that the superconducting phase of the Bi-2212 fiber is separated by different oxidization levels. Therefore, the phase separation is a more plausible explanation of the fishtail effect in the magnetization loops.

The electric properties of a single mesoscopic fiber are characterized by the four-probe method as shown in Fig. 5.41. The fiber is transported in FIB and connected to the electrodes with Pt deposition (details can be seen in section 4.4). Figure 5.42 presents the $R(T)$ curves of a single Li-doped mesoscopic fiber with an applied current of 50 nA. At normal state, the fiber behaves more like a semiconductor rather than a metal, unlike the bulk materials. The resistance of the fiber is very high (10 MΩ scale). Before entering the superconducting state,

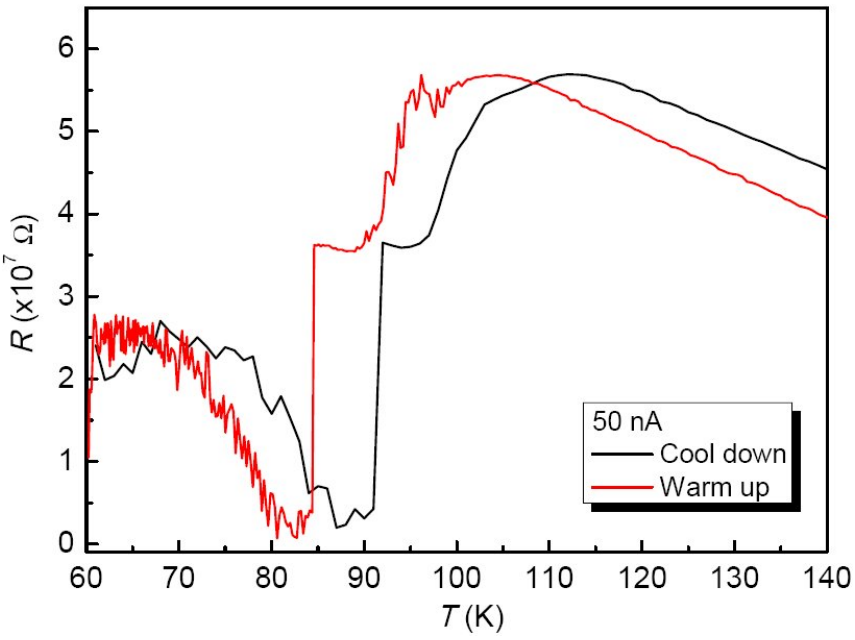

Figure 5.42: The $R(T)$ measurement of the Li-doped mesoscopic fiber with an applied current of 50 nA [115].

the area of the contact interface between the fiber and the electrode is not larger than 1 μm^2. Even with platinum deposition, the high value interface junction resistances dominate the main resistance contribution of the whole system. At lower temperatures, the electric behavior of the single fiber is not as trivial as the bulk superconductor. In the warm-up measurement, the first resistance drop appears at around 95 K, while the second one appears at around 86 K, which corresponds to the T_c estimation from the magnetic data. Right below T_c, around 83 K, the resistance rises with decreasing temperature till around 65 K. Unfortunately, the resistance measurement was hindered at around 60 K by the high frequency noise of the source meter and multimeter. According to the experience from the Li-doped Bi-2212 nanowire network system, the resistance will decrease but never reach zero. The non-zero resistance below T_c leads to a temperature difference between the fiber and the thermal sensor at the bottom of the PCB holder, as a result, a T_c deviation can be found between the warm-up and cool-down curves.

The stepwise resistance behavior was discovered in Bi-2212 nanowire network, and an explanation has been given in section 5.2.3. However, a resistance drop at above 90 K has not been found in the nanowire network system. The possible explanation is hidden in its polycrystalline structure and the phase separation feature. According to the report from Boulesteix [118], the T_c of the Bi-2212 crystal is strongly related to the dependence on the excess of oxygen atoms presenting in the BiO layers. Meanwhile, when the current passes through the BiO layer, the resistance behavior can be separated into metallic behavior and semiconducting behavior, depending on if the current is in-plane or out-of-plane of the layer. Figure 5.43 presents all the resistance behaviors

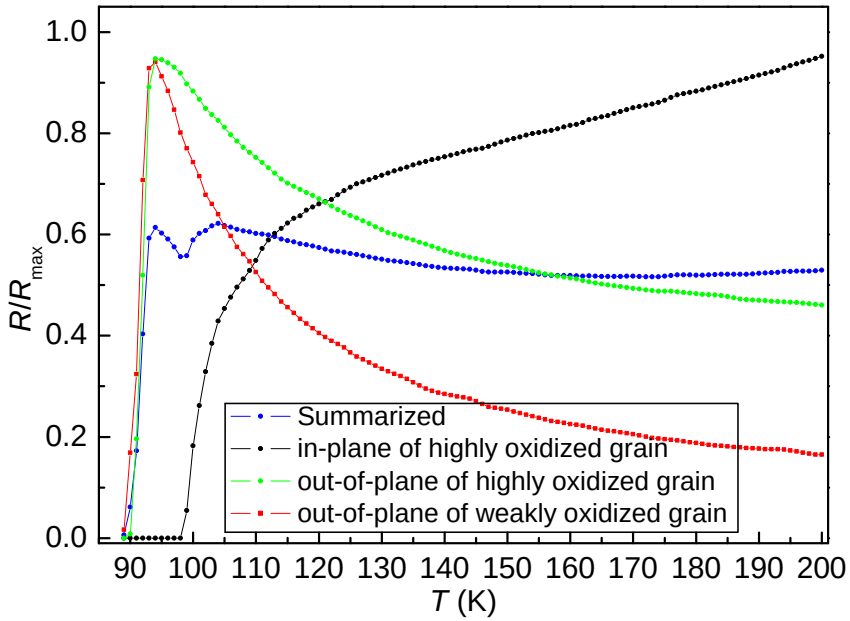

Figure 5.43: The $R(T)$ behaviors of the Bi-2212 crystal grains [118].

mentioned above. When summarizing these cases together, a $R(T)$ curve with stepwise resistance behavior appears as shown in the blue dotted line. This means when the current passes through various grains with different oxidization levels and various lattice orientations, the resistance temperature will be able to present a stepwise resistance drop behavior. This is in good agreement with the resistance behavior of the Li-doped mesoscopic fiber as shown in Fig. 5.42. Combined with the semiconducting contribution from CuO grains, this provides a suitable explanation for the electric properties of the Li-doped Bi-2212 single mesoscopic fiber.

From the investigation of the Li-doped Bi-2212 mesoscopic fiber, it can be confirmed that the Bi-2212 phase and the Bi-2201 phase do not coexist in a single fiber. Since the grains are larger in the mesoscopic fibers, the features of grains provide more influence to its magnetic and electric properties. For example, larger grains provide a bigger regime for the existence of carrier Cooper pairs, as a result, the mesoscopic fiber presents a higher T_c than the nanowire network. The fishtail effect occurs in magnetization loops due to the phase separation between grains. The stepwise behavior (there are three steps in $R(T)$ curve of mesoscopic fiber while there are only two steps presented in the $R(T)$ curves of nanowire network.) appears due to the applied current passing through different types of grains at various orientations.

5.3 $La_{1-x}Sr_xMnO_3$ nanofibers

$La_{2-x}Sr_xCuO_4$ has a Ruddlesden-Popper (RP) phase, consisting of 2D perovskite slabs interleaved with cations (La^+ or Sr^+). $La_{1-x}Sr_xMnO_3$ (LSMO), on the other hands, has a simplified perovskite structure. The superconductivity of LSCO nanowires and nanoribbons has been discussed in section 5.1. Both LSCO nanowires and nanoribbons present weak superconductivity in magnetic measurements. On the other hand, LSMO is ferromagnetic material and it is well known for its CMR properties. It is questioning that how ferromagnetic LSMO nanowires will interact with superconducting LSCO nanowires. Whether the superconductivity of LSCO component is entirely suppressed by the ferromagnetism of LSMO, or the CMR effect of LSMO is influenced by LSCO is one of the main research topics in this work. The answer is given in this section. In the first part of this section, a characterization of the LSMO nanowires is presented. The magnetic and electric properties, especially the magnetoresistive (MR) effect of this system is introduced. Then a discussion about the influence of Sr doping level on the LSMO nanowires is given in the second part. In the last part of this section, an investigation of the properties of the $La_{1.85}Sr_{0.15}CuO_4/La_{0.7}Sr_{0.3}MnO_4$ (LSCO/LSMO) hybrid nanowire network is carried out.

5.3.1 $La_{0.8}Sr_{0.2}MnO_3$ nanowires

The $La_{0.8}Sr_{0.2}MnO_3$ nanowires were fabricated by the electrospinning technique with the precursor listed in table 4.2. The thermal treatment of the as-prepared fiber was separated into four steps: 212 °C, 282 °C, 344 °C and 650 °C. The sample was kept at each step for 1 hour and then naturally cooled down. The first three steps were chosen from peak positions of the DSC graph in Fig. 4.9, with the purpose of smoothly completing all of the intensive exothermal reactions before obtaining the targeted phase. In this way, it is possible that the sample effectively maintains the fiber structure during the thermal treatment. The last step at 650 °C is applied to obtain the $La_{0.8}Sr_{0.2}MnO_3$ phase and completely remove the organic component.

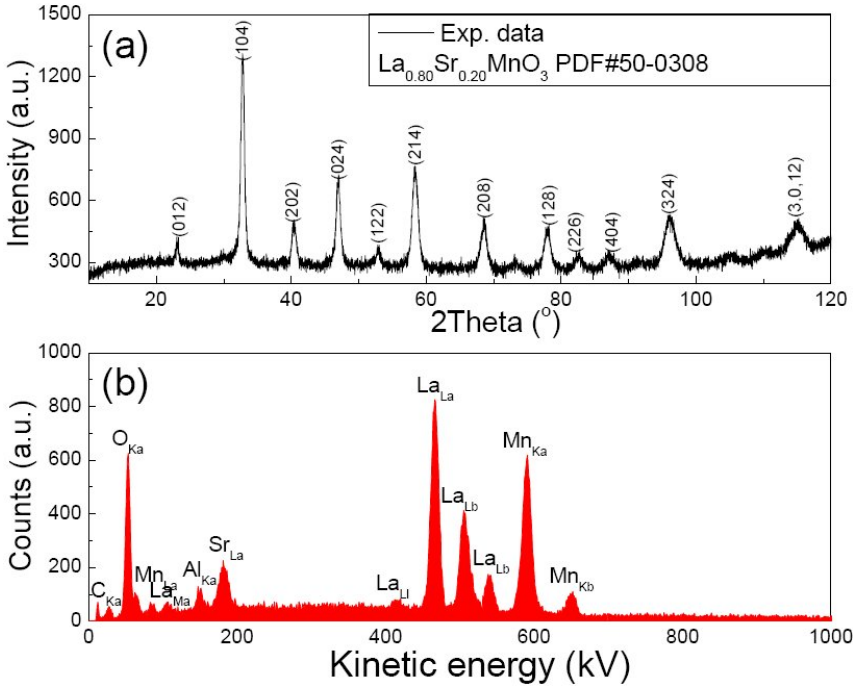

Figure 5.44: (a) XRD result of the $La_{0.8}Sr_{0.2}MnO_3$ nanowire network, with the peaks defined by the standard PDF card #50-0308 and (b) the EDX spectrum of the same sample on an aluminum holder.

The XRD data of the nanowires after thermal treatment is shown in Fig. 5.44a. The experimental data is indexed with the standard PDF-card #50-0308, indicating that the sample is pure $La_{0.8}Sr_{0.2}MnO_3$ with tetragonal lattice structure. No additional phase is discovered. The EDX spectrum is shown in Fig. 5.44b. Table 5.3 presents the results from three different samples with the same treatment. The results from different samples present a similar element distribution as La : Sr : Mn = 0.185 : 0.780 : 1.034, which is close to the target ratio of La : Sr : Mn = 0.2 : 0.8 : 1. It can be concluded that the sample has a uniform element distribution within the pure $La_{0.8}Sr_{0.2}MnO_3$ phase.
The microscopic structure of the $La_{0.8}Sr_{0.2}MnO_3$ nanowires was characterized by SEM and TEM observation as shown in Fig. 5.45. Similar to the other

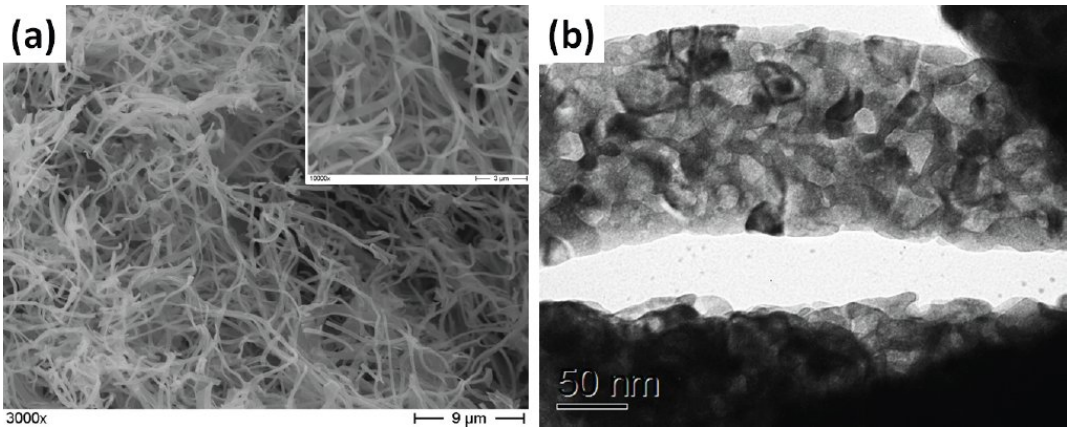

Figure 5.45: (a) SEM image of the nanowire network at 3000× magnification. The inset shows a higher magnification (10000×), illustrating the numerous interconnects between the long nanowires. (b) gives a TEM image of an individual $La_{0.8}Sr_{0.2}MnO_3$ nanowire revealing the polycrystalline, randomly-oriented grain structure.

Element	O K	Sr L	La L	Mn K
Area 1	44.69 %	4.74 %	21.91 %	27.66 %
Area 2	48.24 %	4.92 %	20.93 %	25.91 %
Area 3	49.85 %	4.64 %	19.58 %	25.93 %

Table 5.3: EDX analysis of the LSMO ($x = 0.2$) sample at three different positions.

nanowire sample fabricated by the electrospinning technique, the nanowires are randomly aligned, forming a network structure. The length of an individual nanowire can reach over 100 µm. The interconnections between the nanowires can be seen in the higher magnification SEM image in the inset of Fig. 5.45a. Such interconnections provide weak-links in the sample. These links help the current passing from one nanowire to another through the network system. Figure 5.45b presents the TEM image of a segment of an individual nanowire. From this segment, the diameter of the nanowire can be estimated to be about 200 nm. The polycrystalline character is clearly observed. As the effective microstructure of the sample plays an important role for the comprehension of the magnetoresistive properties, the transmission electron-backscattering diffraction (t-EBSD) technique is employed to obtain details of the grain structure and the arrangement of grain boundaries within an individual nanowire. The t-EBSD technique enables here for the first time a proper analysis of samples with nanometer-sized grains. The grains are oriented randomly as indicated by a large number of grain boundaries with high misorientation angles. Figure 5.46a presents an inverse pole figure (IPF) mapping in [0001] direction of the nanowire segment as shown in Fig. 5.45b. There is no dominating texture in the grains, only some crystallographic orientations are dominating as shown in

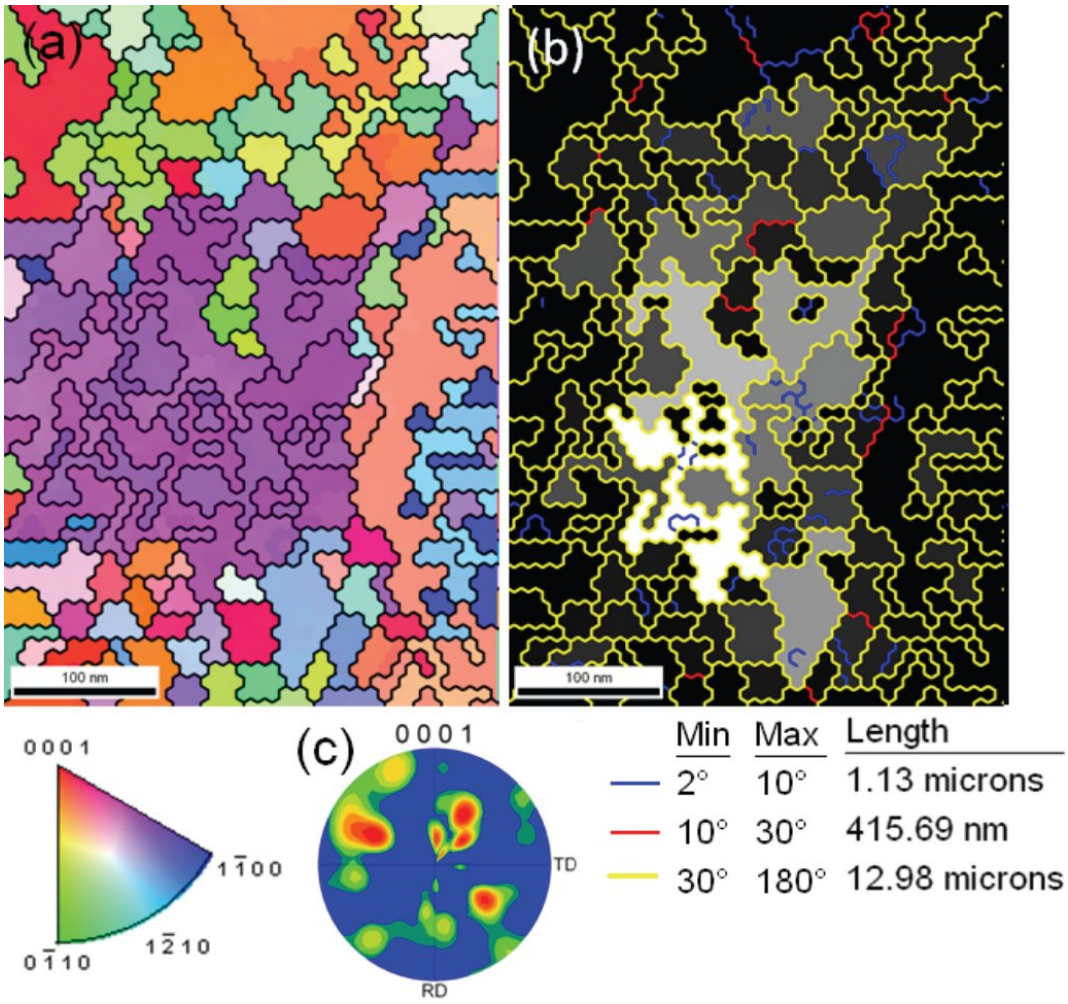

Figure 5.46: t-EBSD analysis on a segment of an individual $La_{0.8}Sr_{0.2}MnO_3$ nanowire. (a) gives the inverse pole figure (IPF) mapping in [0001]-direction. The color code for the orientations is given in the stereographic triangle below the figure. (b) is a grain size mapping in grayscale (0 – small, white – big), together with the grain boundary misorientations indicated in color (2-10°: blue, 10-30°: red and 30-180°: yellow). Additionally, the length of the detected grain boundaries is given below the map. (c) presents the pole figure of the measured region.

the pole figure (Fig. 5.46c). Figure 5.46b shows a grain size mapping of the detection region. It displays the misorientation angles of the grain boundaries and the length of the detected grain boundaries. There are a certain number of small-angle grain boundaries with a length of 1.13 µm, which are marked by blue lines. The grain boundaries with angles between 10° - 30° just occupy some separated area as shown by the red marked lines. The high-angle grain boundaries (30° - 180°) are dominating the segment, with a length of 12.98 µm. Figure 5.47 presents the analysis of the nanowire grain size and diameter distribution from statistics of several SEM and TEM images. The average

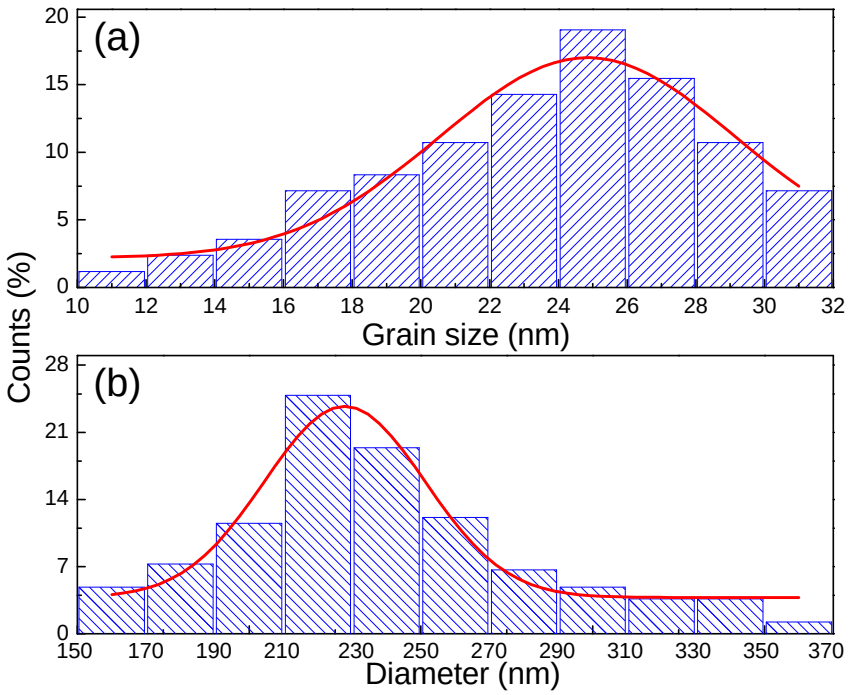

Figure 5.47: Statistics of the nanowire (a) grain size and (b) the diameter.

diameter of the nanowires is 228 nm. The grain size observed from TEM images varies from 10 to 32 nm with an average of 25 nm. Analyzing the XRD data in Fig. 5.44a, the grain sizes estimated from the full width at half maximum (FWHM) of the three strongest peaks (104), (024) and (214) are 15 nm, 18 nm, and 13 nm, respectively. The larger average grain size observed from the TEM data indicates that there are multiple domains in the nanowire. As shown in Fig. 5.48, the temperature dependence of the magnetic properties of the $La_{0.8}Sr_{0.2}MnO_3$ nanowires are measured by SQUID and magnetic thermogravimetric analysis (MTGA). In Fig. 5.48a, the ZFC $m(T)$ curve in the temperature range from 2 K to 350 K is presented. The Curie temperature determined from the fitting is 325.5 K, which is higher than that found in amorphous $La_{0.8}Sr_{0.2}MnO_3$ powder ($T_{\mathrm{Cuire}} \approx 305$ K) [119]. In Fig. 5.48b, the results of the MTGA in the temperature range from 300 K to 470 K are shown with an applied magnetic field of 0.1 T, which is the same as the detection field in the SQUID measurement. When sample changes from paramagnetic to ferromagnetic state, the experienced magnetic force counteracts the gravity of the sample mass. Therefore, the Curie temperature can be estimated by using the mass difference between the curves with and without an applied magnetic field. From the resulting dashed red line, a kink is revealed at 325 K, which corresponds to the Curie temperature obtained from the $m(T)$ measurement.

Figures 5.49a and 5.49b present the magnetization data obtained at 10 K and 300 K. The soft magnetic character of the sample is clearly revealed from the

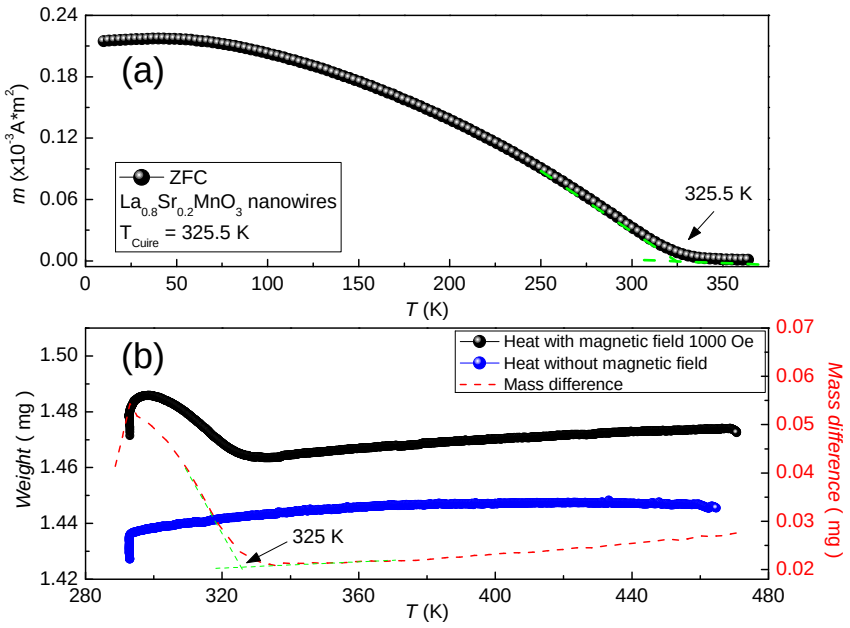

Figure 5.48: (a) ZFC $m(T)$ behavior in the temperature range 2 K $< T <$ 350 K measured with SQUID; (b) magnetic thermogravimetric analysis with (black curve) and without a field of 0.1 T (blue curve). The dashed red line gives the difference between the two curves. The kink in this curve is an indication of the Curie temperature, determined to be 325 K.

magnetization loops. The values of the saturation magnetization M_s are 52.12 A*m^2/kg and 18.10 A*m^2/kg at 10 K and 300 K, respectively. These values are lower than the ones from the corresponding bulk materials (56 A*m^2/kg [120]). The smaller M_s can be attributed to the smaller grain size in the nanowires. The MR plots are calculated from the resistance data obtained by sweep measurements at different field strengths using the relation:

$$MR[\%] = \frac{R_H(T) - R_0(T)}{R_0(T)}, \tag{5.11}$$

where $R_0(T)$ and $R_H(T)$ are the resistance values of the sample under zero field and external field H at temperature T, respectively. Figure 5.50 presents the resistance measurements and the MR ratio of the $La_{0.8}Sr_{0.2}MnO_3$ nanowire network measured in applied fields up to 10 T (with the field applied perpendicular to the sample surface) in the temperature range from 2 K to 275 K. The $R(T)$ curves are shown in Fig. 5.50a, with the inset demonstrating the electric connections to the nanowire network. The MR vs. T curves from 0 to 10 T are shown in Fig. 5.50b, and the MR ratio as a function of the external field in the temperature range from 3 K to 270 K is presented in Fig. 5.50c, with the inset showing the low-field MR at 0.1 T as a function of temperature. Three main features can be seen from Fig. 5.50:

1. There is a suppression of the metal-insulator (MI) transition. This pro-

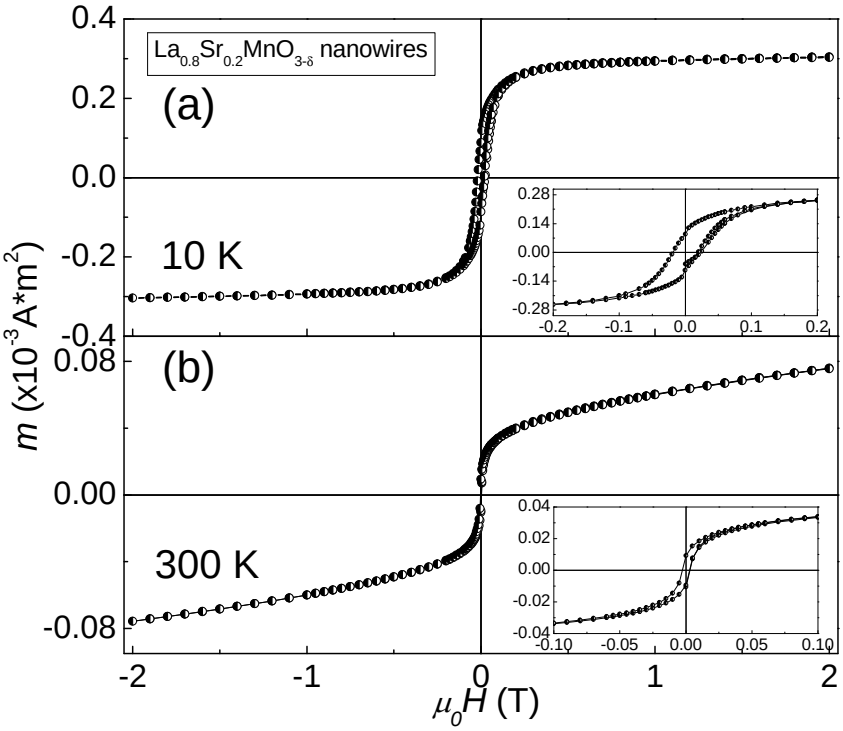

Figure 5.49: The $m(H)$ measurement of the $La_{0.8}Sr_{0.2}MnO_3$ nanowire network at (a) 10 K and (b) 300 K. The insets present the low-field parts of the $m(H)$ loops.

vides another evidence of the size effect. Nanoscale grains are always accompanied by a large number of grain boundaries, which enhance electron scattering. By plotting the $\log(\rho) - 1/\sqrt{T}$ curve (ρ is the resistivity of the sample) at 0 T as shown in Fig. 5.51, a linear behavior is observed when $T \leq 13$ K. This means in this regime the resistivity follows the relationship $\rho \sim \exp\sqrt{\delta/T}$, with an activation energy $\delta = 0.7$ meV. It indicates that the anti-metallic behavior at a lower temperature may be attributed to the Coulomb blockade [121]. To confirm this argument, a calculation of the charging energy E_c is required. E_c can be defined via the following equation:

$$E_c = \left(\frac{e^2}{\pi\varepsilon_0\varepsilon_d}\right)\left(\frac{s}{s+d/2}\right), \tag{5.12}$$

where ε_0 is the dielectric constant of the medium, which for the manganites is taken as 10 [128]. The size related parameter ε_d follows the equation $\varepsilon_d = d/s$ with the average grain size d and the interparticle separation s. For polycrystalline materials, the value of s can be chosen from the thickness of its grain boundary. In the $La_{0.8}Sr_{0.2}MnO_3$ nanowires, the average grain size is 25 nm and the average thickness of the grain boundaries is about 5 nm according to the TEM observation, thus $E_c \approx 1.147$ meV ≈ 13.3

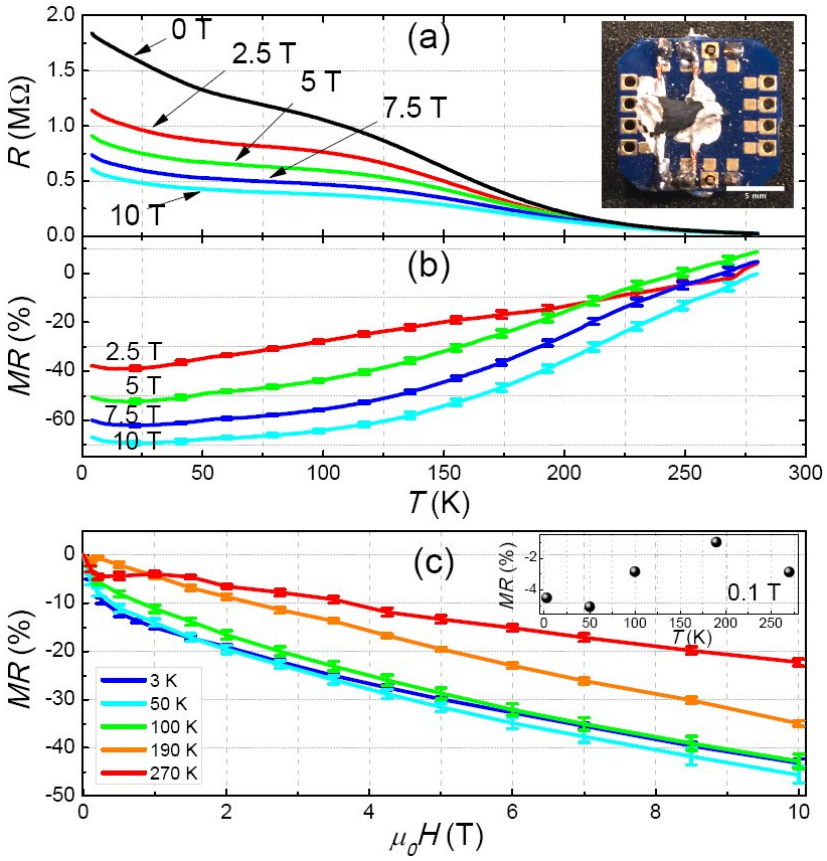

Figure 5.50: Resistance (a) and MR ratio (b) of the $La_{0.8}Sr_{0.2}MnO_3$ nanowire network measured up to 10 T with applied magnetic fields ($H \perp$ sample surface) in the range 2 K $< T <$ 275 K. The inset to (a) shows the sample with the electric connections mounted on the sample holder. (c) presents the MR ratio as a function of the applied magnetic field for various temperatures. The inset to (c) gives the low-field magnetoresistance measured at 0.1 T as a function of temperature.

K. Since the temperature regime of the $\rho \sim \exp\sqrt{\delta/T}$ behavior is below 13 K, which is just below E_c, the contribution of the Coulomb blockage is confirmed. On the other hand, the influence from certain size effects varies with the Sr doping level x in LSMO materials. A step-shaped resistance behavior can still be observed for the $x = 0.2$ sample. This indicates that the MI transition is not completely suppressed.

2. At an external field of 0.1 T, a maximum MR of 5.05 % is obtained at $T = 50$ K as shown in the inset of Fig. 5.50b. This value is not particularly high, however, it can only be achieved when mixing other compounds to the $La_{0.8}Sr_{0.2}MnO_3$ powder [123], which can enhance the low field magnetoresistance (LFMR). Jugdersuren et al. [124] reported a large LFMR at room temperature in their LSMO nanowires extracted from network fabrics produced by electrospinning. They showed a dependence of the LFMR on the nanowire diameter, but no information on the

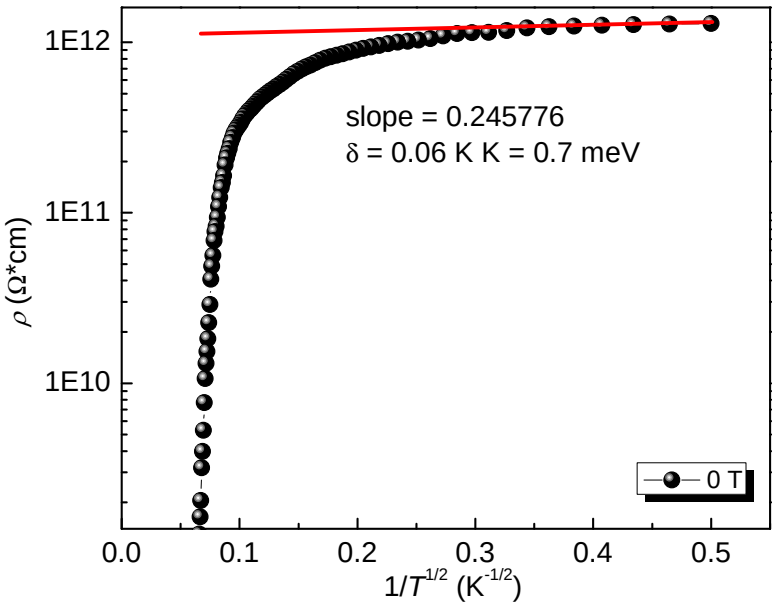

Figure 5.51: Plotting of ρ vs. $1/\sqrt{T}$ at 0 T. When $T \leqslant 16$ K ($1/T \geqslant 0.25$ $\mathrm{K}^{-1/2}$), ρ follows the $\exp(\sqrt{\delta/T})$ behavior, with the δ value shown in the graph.

LSMO grain size was presented. The LFMR at 300 K for the sample in this work is comparable to their data, even though the chemical composition is different. Nevertheless, it demonstrates that the LFMR can be considerably enhanced by reducing the nanowire diameter as well as the LSMO grain size. This discovery demonstrates another possibility

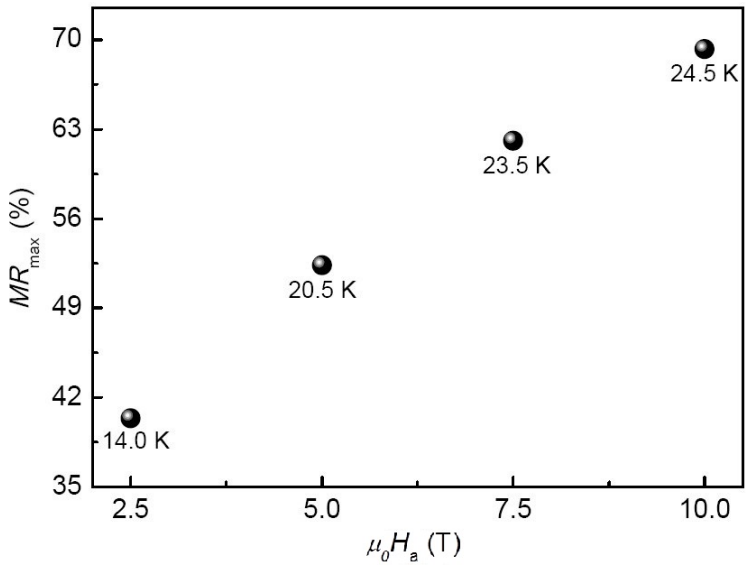

Figure 5.52: Relationship of maximum MR at given temperatures to the applied external field H_a, extracted from Fig. 5.50b.

of LFMR enhancement besides adding other compounds.

3. The sample exhibits a strong MR effect at low temperatures as shown in Fig. 5.52. At an applied field of 2.5 T, the maximum of the MR is already over 40 %, while an MR ratio of nearly 70 % is observed for the sample at 24.5 K and 10 T. It confirms that the high field magnetoresistance (HFMR) can be increased by reducing the grain size and the interface area as reported by Balcells et al. [128].

So far, a morphology characterization and the magnetic and electric properties of the $La_{0.8}Sr_{0.2}MnO_3$ nanowire network fabricated by electrospinning technique have been introduced. As expected, a size influence on the MR of the LSMO materials has been discovered. The reduced dimensions of the nanowires (grain size, wire diameter) and a large number of interconnects between them have been found to increase the MR effect as compared to bulk LSMO samples. In the next step, the influence of the Sr doping level x on the LSMO nanowire network system is introduced.

5.3.2 Sr doping level influence on $La_{1-x}Sr_xMnO_3$ nanowires

Thanks to the convenience of element ratio adjustment in the sol-gel, LSMO nanowires with different Sr doping level can be easily fabricated by the electrospinning technique and the subsequent thermal treatment. Here the Sr doping levels $x = 0.2$, 0.3 and 0.4 are chosen, and the precursors are listed in table 4.2.

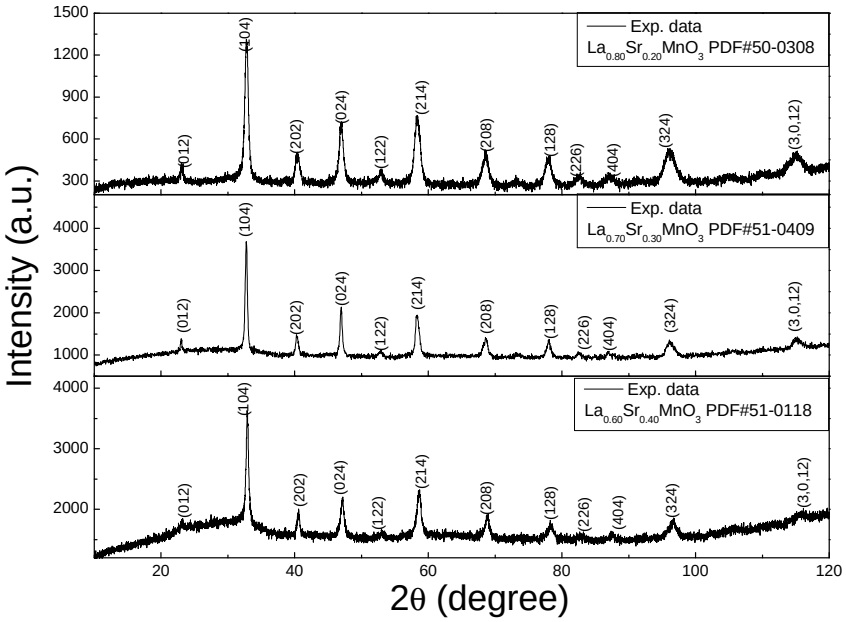

Figure 5.53: XRD measurements on all three types of LSMO nanowires.

The phases of all three types of nanowires have been confirmed by the XRD measurement as shown in Fig. 5.53. All peak positions of the experimental spectra are consistent with the corresponding data from the reference PDF-cards.

Figure 5.54 presents the microstructures of all three types of LSMO nanowires

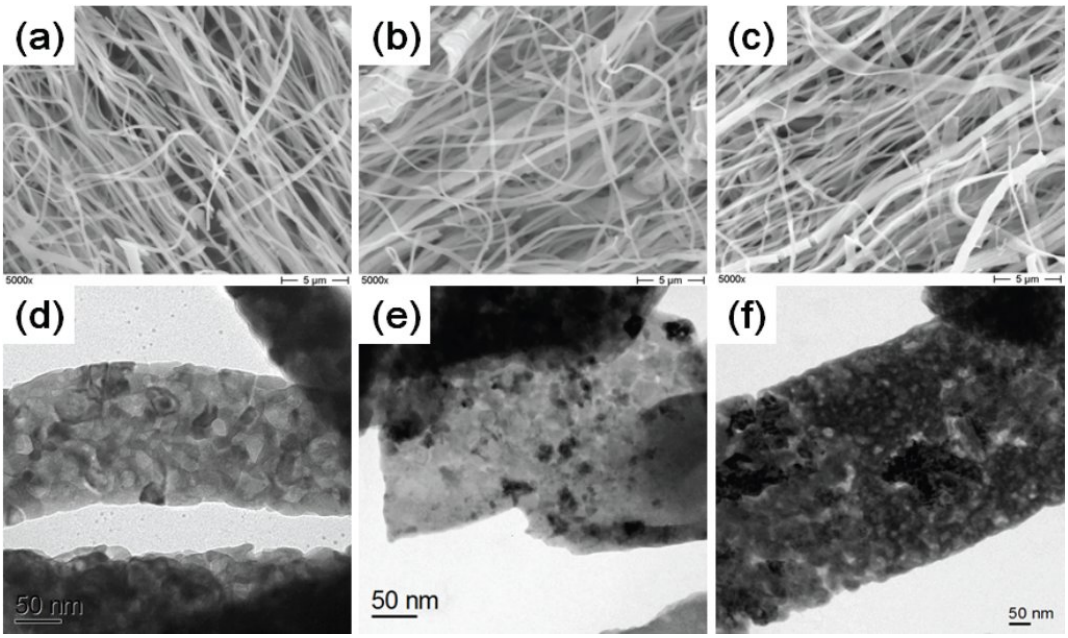

Figure 5.54: SEM image of the LSMO nanowires at 5000× magnification and the brightfield TEM images of the corresponding nanowire segments above. (a), (d) $x = 0.2$; (b), (e) $x = 0.3$; (c), (f) $x = 0.4$.

through the SEM and TEM observation. Similar to the LSMO nanowires with $x = 0.2$, all three types of nanowires have an average diameter of around 220 nm and an average length of up to 100 µm. They are all polycrystalline with an average grain size of about 20 nm. Hence it can be ensured that the LSMO nanowires with expected Sr doping levels have been successfully synthesized. There is no obvious morphological difference between these three types of LSMO nanowires. The upcoming observed differences are ascribed to their only difference – the Sr doping level.

Figure 5.55 presents the magnetization data obtained from SQUID for the LSMO nanowires. From the ZFC $M(T)$ curves, it can be found out that all three types of LSMO nanowires have the Curie temperatures of over 320 K. The sample with $x = 0.3$ has the highest $T_{\mathrm{Cuire}} = 333.7$ K. In the magnetization loops, all nanowires demonstrate soft ferromagnetic behavior. From the Sr doping level $x = 0.2$ to 0.4, the saturation magnetizations M_{s} are 52.12 A*m^2/kg, 58.13 emu/g, 55.03 A*m^2/kg at 10 K and 18.10 A*m^2/kg, 33.09 A*m^2/kg, 24.62 A*m^2/kg at 300 K, respectively. These values are lower than the ones from the corresponding bulk materials (56 A*m^2/kg, 33.09 A*m^2/kg, 24.62 A*m^2/kg) [125, 126]. As mentioned in the last section, this is due to the smaller grain size in the nanowires. The $x = 0.3$ nanowire network shows the highest M_{s} while the $x = 0.2$ nanowire network shows the lowest M_{s} at both 10 K and 300 K. This is in good agreement with the conclusion drawn from the bulk materials that the optimized doping level around $x = 0.33$ supplies the strongest magnetism. Figure 5.56 presents the resistance measurements for all three types of LSMO

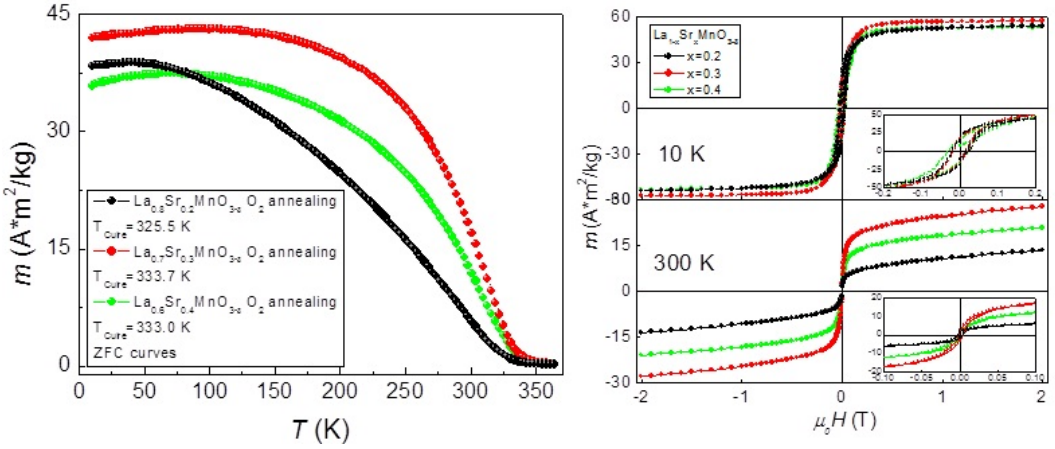

Figure 5.55: Magnetic properties of the LSMO nanowires. The plotting on the left side is the ZFC $m(T)$ curves with detection field 0.1 T; the plotting of the right side is the $m(H)$ measurements at 10 K and 300 K, the insets present the zoom-in details at low fields. In order to compare the magnetic properties of three types of nanowires, the magnetic moments m are divided by the masses of the samples.

nanowires at temperatures from 5 K to 275 K. The external field is applied perpendicular to the surface of the nanowire network, in other words, the current flow is perpendicular to the field. Similar to the $x = 0.2$ nanowires, the other two LSMO nanowires demonstrate a suppression of the metallic behavior. However, the suppression varies with the doping level. For $x = 0.2$ nanowires, a step-shaped resistance behavior can be observed, which indicates that the MI transition is not completely suppressed. For $x = 0.4$ nanowires, the resistance decreases almost linearly from 5 K to 200 K. According to the MR curves, it can be seen that the $x = 0.3$ sample with the highest saturation magnetization shows the weakest MR effect, inversely, the $x = 0.2$ sample exhibits the strongest MR. Table 5.4 presents the MR comparison of different Sr doping levels at 2.5 T

	MR (%) at 2.5 T			MR (%) at 10 T		
x	100 K	270 K	MR_{max}	100 K	270 K	MR_{max}
0.2	27.69	1.81	39.05 (14 K)	64.12	4.62	69.28 (25 K)
0.3	13.20	6.32	15.18 (169 K)	40.88	5.84	40.93 (92 K)
0.4	17.48	13.00	17.97 (57 K)	41.99	23.47	43.45 (54 K)

Table 5.4: MR comparison of the LSMO nanowire networks with Sr doping levels of $x = 0.2$, 0.3 and 0.4 at 2.5 T and 10 T.

and 10 T. Interestingly, the maximum of MR of the $x = 0.3$ sample appears at a relatively high temperature while the $x = 0.2$ sample always reaches maximum MR at the lowest temperature among all three types of nanowires.
With the measurements above, the influence of the Sr doping level has been demonstrated. According to the comparison, the strongest magnetism appears

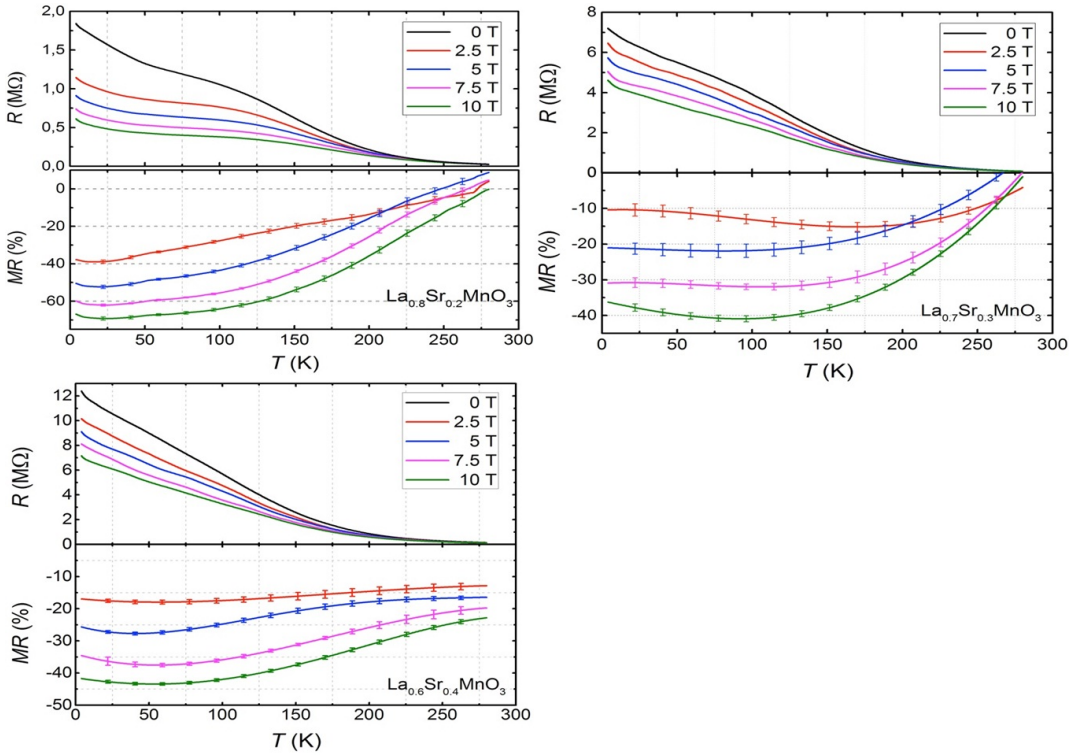

Figure 5.56: Resistance and MR ratio of all LSMO nanowires measured up to 10 T applied magnetic field in the range 5 K $< T <$ 275 K.

in the $x = 0.3$ sample, but it shows the weakest MR effect. In contract, the $x = 0.2$ sample exhibits the weakest magnetism but strongest MR effect. The suppression of the metallic behavior in the $R(T)$ curves is not only determined by the grain size of the sample but also the Sr doping level.

5.3.3 $La_{1.85}Sr_{0.15}CuO_4/La_{0.7}Sr_{0.3}MnO_3$ hybrid nanowire network

In the previous sections, the properties of the superconducting nanowires, mesoscopic fibers, and the CMR nanowires have been demonstrated. In this last

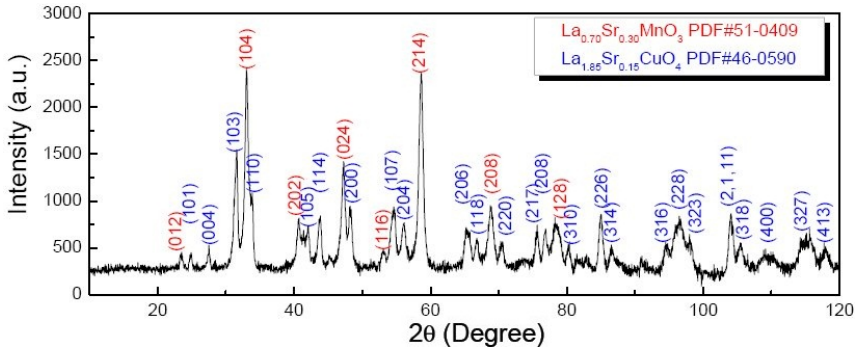

Figure 5.57: XRD result of the hybrid nanowires.

section, an investigation of the hybrid nanowire network with superconducting material LSCO and CMR material LSMO (in this section, LSMO stands for $La_{0.7}Sr_{0.3}MnO_3$ instead of $La_{1-x}Sr_xMnO_3$) is given. Such hybrid nanowire structure can be fabricated by electrospinning with two different precursors in the same procedure: In one period, each precursor is electrospun for fixed time and then switched to the other one, with the purpose of ensuring a thin layer created by nanowire crossing each other is formed. In this way, a hybrid structure with two different materials duplicated layer by layer is obtained.
The thermal treatment of the hybrid sample is nearly the same as the treatment of the LSMO nanowires except that the last treatment temperature was increased to 700 °C with the purpose of obtaining the LSCO phase. According to the XRD measurement as shown in Fig. 5.57, the sample does present two phases as expected. And no mixed phase of other impurities are found.

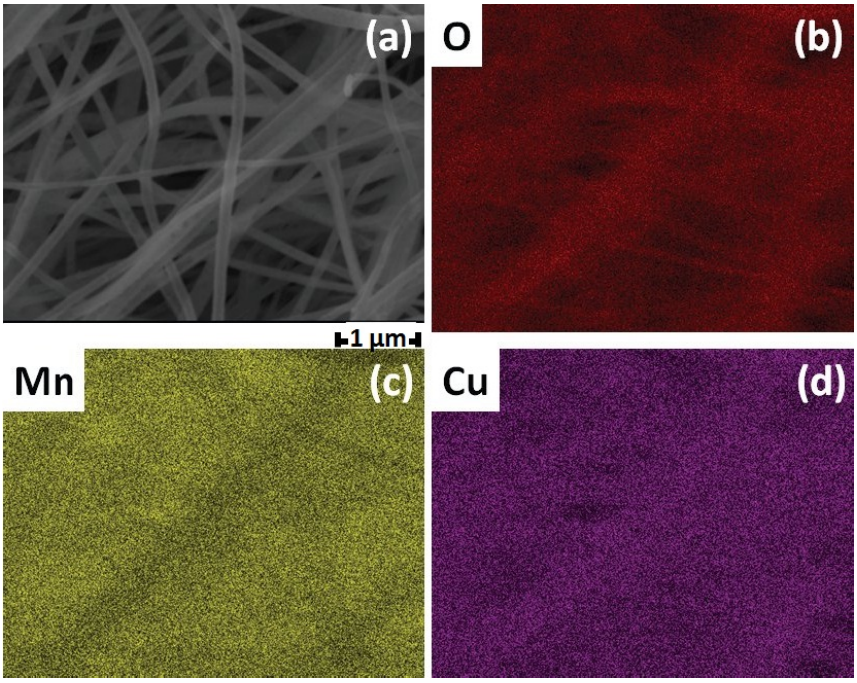

Figure 5.58: (a) SEM image of the hybrid sample observed by SEM, and the EDX mapping for the elements (b) O, (c) Mn and (d) Cu.

Figure 5.58 presents the microstructure of the hybrid nanowires together with their EDX element mapping. The average diameter of the nanowires is about 220 nm. The length of the nanowires reaches over 50 µm. In the Mn mapping, dark fiber shape regimes can be found, which are the Cu rich regimes. The opposite case appears in Cu mapping, where the Mn rich regimes can be found as dark fiber shaped structures. The element O is distributed equally in the image as expected. This observation demonstrates that the LSMO and LSCO nanowires are homogeneous: There is no mixture phase containing both Cu and Mn, which is in a good agreement with the XRD result.
Figure 5.59a presents the $M(T)$ ZFC curves for pure LSMO and the hybrid

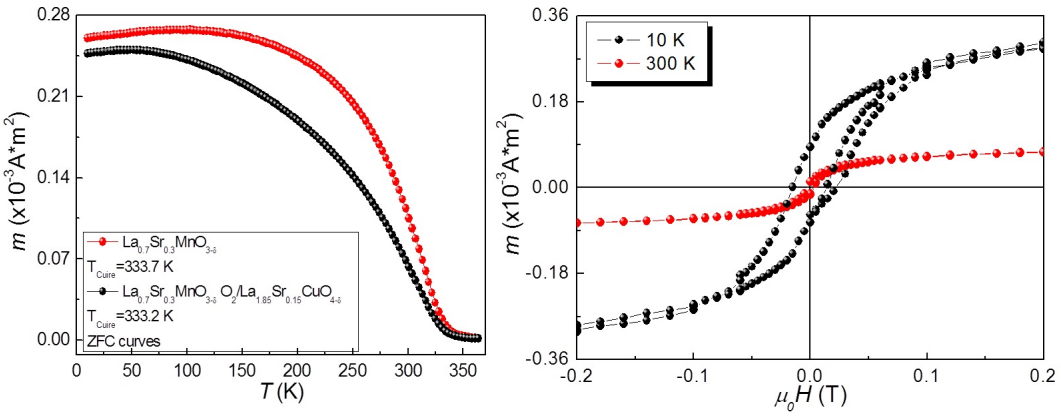

Figure 5.59: Magnetic properties of the LSCO/LSMO hybrid nanowire network: (a) The ZFC $m(T)$ comparison between the hybrid nanowire network and the pure LSMO nanowires with a detection field of 0.1 T; (b) The $m(H)$ loops of the hybrid nanowire network at 10 K and 300 K. The magnetic moments m are divided by the masses of the samples for comparison of the magnetic properties.

LSCO/LSMO sample. The resulting magnetization of the hybrid sample is smaller than that of the pure sample, corresponding to the smaller volume content of the LSMO phase as compared to the pure sample. The Curie temperature, T_{Cuire}s, of both samples are, however, quite similar (333.2 K and 333.7 K). The superconducting diamagnetic behavior does not appear at low temperatures as it does in the other LSCO sample. This can be ascribed to the high detection field of 1000 Oe applied in the measurement, as the pure LSCO nanofibers just present superconductivity with low detection fields of around 20 Oe [68]. Figure 5.59b presents the magnetization hysteresis loops ($M(H)$) for the LSCO/LSMO hybrid sample ($H \perp$ sample surface) measured at 10 K and at 300 K. The magnetization loops clearly demonstrate the soft magnetic character of the LSCO/LSMO nanowire network samples. At 10 K, it is interesting that the initial curve deviates from the rest of the magnetization loop. Furthermore, at a higher external field, where the ferromagnetic samples should reach their saturation, a weak field irreversible behavior is discovered. These two features can be attributed to the superconductivity contribution of the LSCO component.

Figure 5.60 presents the resistance behavior of the hybrid sample in various applied magnetic fields (0 T, 2.5 T, 5.0 T, and 7.5 T) in a temperature range from 5 K to 300 K. Different from the bulk LSMO sample, the pure LSMO nanowires present a suppression of the MI transition at low temperatures, the slope change at around 100 K certifies the residual of the MI transition. It has been discussed in the previous section that such a suppression can be attributed to the Coulomb blockade effect stemming from the small grain sizess [121, 127, 128]. In the LSCO/LSMO hybrid nanowires, the MI transition is completely suppressed, even though the average grain size (∼30 nm) is slightly

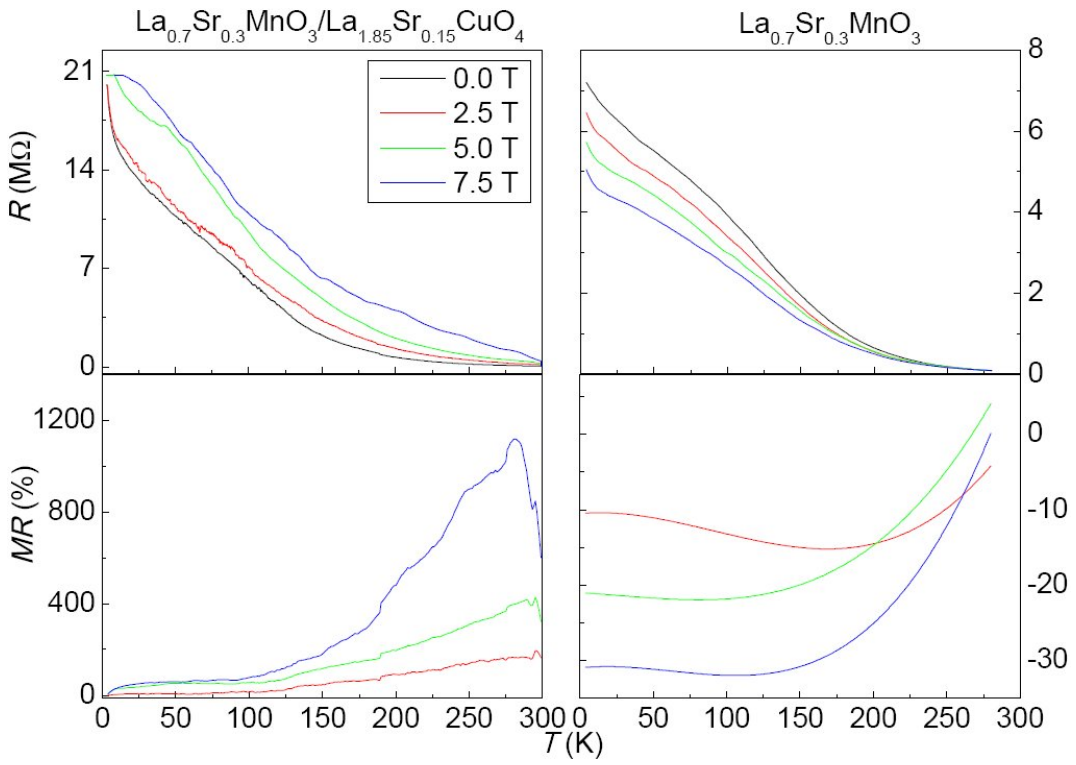

Figure 5.60: $R(T)$ diagram and the MR ratio for the LSCO/LSMO hybrid sample (left) and the pure LSMO nanowires (right) as a function of the temperature.

larger than that in the pure LSMO nanowires (∼20 nm). The lower graphs in Fig. 5.60 present the MR ratios of both types of samples. Unlike the pure LSMO nanowires, the resistance of the hybrid sample increases with a rising field, therefore, it shows a positive MR effect. Overall, it seems like the hybrid sample shows no superconductivity in the electric measurement. Actually, this is a result of the competition between the magnetoresistive LSMO component and the superconducting LSCO component:

1. The field increasing resistance stems from the LSCO component as the resistance of the superconductor increases with a rising magnetic field.
2. Different from the pure LSMO sample, the shape of the $R-T$ curve varies with the magnetic field. At 5 T, a bending appears at around 50 K, at 7.5 T, the bending becomes more obvious and appears at around 20 K. Such bending results from the competition between the field increasing resistance effect of the LSCO component and the negative MR effect of the LSMO component. At temperatures below 150 K, the MR curves intent to merge together. At this temperature range, the MR effect is stronger than the one at high temperatures, it is sufficient to compensate for the resistance increase from the superconducting component.

To summarize, the LSCO/LSMO hybrid nanowire network can be successfully fabricated by electrospinning. The XRD and EDX analysis confirm that the

LSCO phase and the LSMO phase do not interfere with each other during the phase formation process. The presenting magnetic and electric properties of the hybrid nanowire network demonstrate a competition of the ferromagnetic magnetoresistive LSMO component and the superconducting LSCO component.

6 Conclusion and outlook

All the samples in this work were fabricated by the electrospinning technique. With regular electrospinning, the samples are nanowires with a diameter of ∼300 nm. The nanowires overlap with each other and form a network system. The average length of the nanowires is determined by the final annealing temperature. When the nanowires are annealed at 800 ^{o}C, the average length of the nanowires is ∼100 µm. If the annealing temperature is reduced to 750 ^{o}C, the average length is doubled to ∼200 µm. By controlling the concentration of the precursor, it is possible to tailor the shape of the fiber. For example, with higher concentration, ribbons are obtained (as seen in section 4.2). With rearrangement of the electric field distribution of the setup, parallel nanowires (section 4.3) and mesoscopic fibers (section 5.2.6) can be fabricated.
All the samples in this work are polycrystalline. The grain structure and grain boundaries are essential factors for the physical properties of these nanowire network systems. The LSCO nanoribbons possess higher T_c than the LSCO nanowires, due to the larger grain size in nanoribbons (section 5.1.2). The LSMO nanowires have a smaller M_s than the bulk materials mainly because of a smaller average grain size of the LSMO nanowires. Such small grains and their grain boundaries cause Coulomb blockades within the nanowires, as a result, the MI transition is suppressed in the electric measurement (section 5.3.1).
Research on the superconductivity of Bi-2212 nanowire networks was one of the main targets of this work. Three different types of Bi-2212 nanowire network (non-doped Bi-2212, Pb-doped Bi-2212 and Li-doped Bi-2212) have been synthesized. In order to suppress the formation of the Bi-2201 phase, excessive Ca and Cu were applied to the precursor of the non-doped Bi-2212 nanowire network. The Bi-2212 phase was obtained at 800 ^{o}C. Pb doping can also help to form the Bi-2212 phase. By means of 5 % Pb doping, the Bi-2212 phase was obtained at 800 ^{o}C without additional Ca and Cu applied. Li doping can help to convert the Bi-2201 phase to the Bi-2212 phase at a lower temperature. With 30 % Li doping, 70 % of the Bi-2201 phase converts to the Bi-2212 phase at 750 ^{o}C (section 4.5.2). According to the EDX analysis, the Bi-2212 phase and the Bi-2201 phase do not coexist in the same fiber (section 5.2.5 and 5.2.6).
The superconductivities of Bi-2212 nanowire networks were characterized by magnetic and electric measurements:

1. Bi-2212 nanowire networks present polycrystalline characteristics in magnetic measurements. Below T_c, the magnetization loops are asymmetric with respect to the $M = 0$ axis (section 5.2.1). An estimation of J_c by

the Bean model is not possible. Therefore, ECSM was applied for the estimation of J_c and F_p (section 5.2.2).

2. The stepwise resistance behavior appears in all three types of Bi-2212 nanowire networks. This indicates that Bi-2212 nanowire networks cannot be treated as simple polycrystalline superconductors. They are network systems consisting of superconducting grains and Josephson junctions. The RCSJ model provides an explanation of this stepwise behavior. According to the analysis of the data from $R(T)$ and $U(I)$ curves, it has been confirmed that the TAPS contributes to the non-zero resistance below T_c (section 5.2.3).
3. Since the Bi-2212 nanowire network is a network system with Josephson junctions, a metal layer can enhance the Josephson coupling of the sample. As a result, the T_c is higher after coating a metal layer with a certain thickness (section 5.2.4). Both the proximity effect and the Josephson coupling enhancement occur when the nanowire network is coated by a metal layer. Therefore, whether the T_c increases or decreases depends on the thickness of the metal layer.

With the assistance of FIB, it is feasible to prepare a setup for a single nanowire measurement (section 4.4). However, the single nanowire was damaged during the measurement due to the noise fluctuation from source meter. As compensation, the investigation switched to the Li-doped Bi-2212 mesoscopic fiber. The high resolution EDX analysis showed that the Li-doped fibers consist of either Bi-2212 grains and CuO grains or Bi-2201 grains and CuO grains. The Bi-2212 grains can be classified into either weakly oxidized grains or highly oxidized grains. In other words, the superconducting phase of Bi-2212 is seperated by different oxidization levels. Such phase separation leads to the fishtail effect observed in magnetization loops and the stepwise resistance behavior in electric measurement (section 5.2.6).

Investigation of the interaction between superconducting nanowires and ferromagnetic nanowires was the other main target of this work. The La-based materials $La_{1.85}Sr_{0.15}CuO_4$ and $La_{0.7}Sr_{0.3}MnO_3$ were chosen to be the superconducting component and ferromagnetic component respectively. $La_{2-x}Sr_xCuO_4$ has a Ruddlesden-Popper (RP) phase, consisting of 2D perovskite slabs interleaved with cations (La^+ or Sr^+). The superconductivity of these nanowires was confirmed by magnetic measurements. The T_c was found at $\sim$19.2 K. This is lower than the nanoribbons (29.3 K) and the bulk material (37 K) (section 5.1.2). $La_{1-x}Sr_xMnO_3$ has a simplified perovskite structure. It is one of the well known materials of the CMR family. Its physical properties are influenced by the Sr doping level:

1. A suppression of the MI transition was discovered in the $La_{0.8}Sr_{0.2}MnO_3$ nanowires (section 5.3.1). The suppression becomes more obvious with higher Sr doping levels (section 5.3.2).
2. When the Sr doping level is close to 33%, the nanowire networks present the strongest magnetism, while the maximum MR of this sample is the lowest among the samples with various Sr doping levels (section 5.3.2).

Hybrid nanowire networks present soft ferromagnetic behavior in magnetic measurements. A deviation between the initial magnetization curve and the rest of the magnetization loop is observed in the $M(H)$ curve at 10 K. A complete suppression of the MI transition appears in the electric measurement. Unlike the pure $La_{0.7}Sr_{0.3}MnO_3$ nanowire network, the negative MR is replaced by a positive one. This can be attributed to the electric properties of the superconducting component. All these features demonstrate a competition of the ferromagnetic magnetoresistive component and the superconducting component in the hybrid nanowire network (section 5.3.3).

Polycrystalline superconductivity has been investigated since the discovery of non-metal superconductors. Most of the research focusses on polycrystalline thin films [23, 24, 25]. Research on 1D superconductors is developing with the progress of nanotechnology. Most of the research is based on superconductors with a diameter below 10 nm. Because this is close to the limit distance of the existence of the Cooper pair. Some quantum effects like QPS occur when the size of the sample reaches this level [17, 18, 33]. The superconducting polycrystalline fibers with diameter range between 100 nm to 1 µm attract less interest of researchers. In the few reports about these fibers, only the magnetic properties are presented as evidence of the superconductivity of the samples [129, 130].

Superconductivity, especially the electric behavior in the superconducting state of polycrystalline nanowires has not been widely investigated. It is a 'vacancy' of research on 1D superconducting fibers. The main purpose of this work is to make some contribution to filling this vacancy. The unique features like stepwise resistance behavior and T_c enhancement by Au coating certify the research value of superconducting nanowire networks. A description of the electric behavior by RCSJ model is a novel idea. It manages to explain the stepwise resistance feature of the nanowire networks. However, it leaves some new questions afterward:

1. What is the prerequisite for the formation of Josephson junctions?
2. Under which conditions is the tunnel current able to pass through the Josephson junctions?
3. How to adjust the temperature of the resistance step?
4. Both gran boundaries and weak-links between nanowires can provide a non-superconducting layer to the Josephson junction. Which one is more important?

By solving these problems, a better comprehension of the electric behavior of the superconducting nanowire network will be established.

It is unfortunate that the electric properties of a single Bi-2212 nanowire were not successfully measured. The electric properties of a single mesoscopic fiber have been investigated in this work. Some new features have been discovered in both magnetic and electric measurements. However, the research on a single nanowire cannot be simply replaced by the investigation on a mesoscopic fiber. The research on the electric properties of a single superconducting nanowire can help to gain a deeper comprehension of the electric behavior of the nanowire

network. It would further verify the concept of applying the RCSJ model to the electric mechanism of the nanowire network.
So far, there is no application of polycrystalline superconducting nanowire networks. However, potential applications can be foreseen from its unique features:

1. The temperature dependence of resistance is stepwise in Bi-2212 nanowire networks. This means that the Bi-2212 nanowire network possesses three different states at different temperature ranges:
   a) A high resistance, above T_c state, called normal state.
   b) intermediate state between T_c and the temperature of the second step T_{2nd}. The resistance becomes lower, but it is not completely zero. In the magnetic measurements, it has been confirmed that the Bi-2212 nanowire network shows diamagnetic behavior in this state.
   c) final state below T_{2nd}. The resistance reaches a minimum. It behaves like a trivial superconductor in the superconducting state. Therefore, it is not influenced by the external magnetic field as long as the field is not above a critical value.

   It can be found that at a certain temperature range the Bi-2212 nanowire network possesses both relative stable resistance and diamagnetic property. This feature can not be found in other superconductors.
2. The Josephson junctions can be used in the digital circuit and memory application [131, 132]. The Bi-2212 nanowire network is a system consisting of a large amount of Josephson junctions. Maybe it can be applied to a similar field.

These are the questions and tasks I will try to answer in the future. I will devote to the research of functional nano-materials, not only superconductor or CMR materials, but also, I will try to develop the high yield system for nanofiber fabrication.

7 List of publications during the PhD work

1. **Xian-Lin Zeng**, Michael R. Koblischka, Uwe Hartmann "Synthesis and characterization of electrospun superconducting (La,Sr)CuO4 nanowires and nanoribbons" Mater. Res. Express, **2**, 095022 (2015).
2. Miryala Muralidhar, Nakazato Kenta, **Xian-Lin Zeng**, Michael R. Koblischka, Pavel Diko, Masato Murakami, "Record critical current densities in IG processed bulk YBa2Cu3Oy fabricated using ball-milled Y2Ba1Cu1O5 phase" Physica Status Solidi A-Applications And Materials Science, **213**, 443 (2016).
3. Michael R. Koblischka, **Xian-Lin Zeng**, Thomas Karwoth, Uwe Hartmann, "Magnetic properties of electrospun non-woven superconducting fabrics" AIP Adv., **6**, 035115 (2016).
4. Michael R. Koblischka, **Xian-Lin Zeng**, Thomas Karwoth, Thomas Hauet, Uwe Hartmann, "Transport and Magnetic Measurements on $Bi_2Sr_2CaCu_2O_8$ Nanowire Networks Prepared Via Electrospinning" IEEE Trans. Appl. Supercond., **26**, 1800605 (2016).
5. **Xian-Lin Zeng**, Michael R. Koblischka, Thomas Karwoth, Thomas Hauet, Uwe Hartmann, "Preparation of granular Bi-2212 nanowires by electrospinning" Supercond. Sci. Technol. **30**, 035014 (2017).
6. **Xian-Lin Zeng**, Michael R. Koblischka, Thomas Karwoth, Uwe Hartmann, Dennis Gokhfeld, Crosby Chang, Thomas Hauet, "Analysis of magnetization loops of electrospun nonwoven superconducting fabrics" Phys. Rev. Mat. **1**, 044802 (2017).
7. **Xian-Lin Zeng**, Michael R. Koblischka, Fabian Laurent, Thomas Karwoth, Anjela Veneva Koblischka, Uwe Hartmann, Crosby Chang, Praveen Kumar, Oliver Eibl, "Characterization of Electrospun $Bi_2Sr_2CaCu_2O_{8+\delta}$ Nanowires With Reduced Preparation Temperature" IEEE Trans. Appl. Supercond. **28**, 1-5 (2018).
8. Thomas Karwoth, **Xian-Lin Zeng**, Michael R. Koblischka, Uwe Hartmann, Crosby Chang, Thomas Hauet, Jian-Min Li, "Magnetoresistance and structural characterization of electrospun $La_{1-x}Sr_xMnO_3$ nanowire network fabrics with x = 0.2" submitted to Solid State Commun **290**, 37-41 (2019).
9. **Xian-Lin Zeng**, Michael R. Koblischka, Thomas Karwoth, Uwe Hartmann, "Properties of $La_{1.85}Sr_{0.15}CuO_4/La_{0.7}Sr_{0.3}MnO_3$ hybride nanowire networks prepared by electrospinning" J. Magn. Magn. Mater. **475**, 741-745 (2019).

Bibliography

[1] F. Anton, U.S. Patent No. 2158415 (May 16, 1939).

[2] F. Anton, U.S. Patent No. 2349950 (May 30, 1944).

[3] F. Anton, U.S. Patent No. 1975504 (October 2, 1934).

[4] H. L. Simons, U.S. Patent No. 3,280,229 (October 18, 1966).

[5] G. Taylor, Proc. R. Soc. London, Ser. A **313**, 453 (1969).

[6] F. London, H. London, Sciences, **149**, (866):71 (1935).

[7] V. L. Ginzburg and L. D. Landau, Zh. Eksp. Teor. Fiz. **20**, 1064 (1950).

[8] J. Bardeen, L. N. Cooper and J. R. Schrieffer, Phys. Rev. **106**, 162 (1957)

[9] S. Fujita and S. Godoy, Theory of High Temperature Superconductivity (Kluwer Academic Publishers, Dordrecht, 2002).

[10] M. Casas, A. Rigo, M. de Llano, O. Rojo, M.A. Solis, Phys. Lett. A **245**, 55 (1998).

[11] S. Fujita, K. Ito and S. Godoy, Quantum Theory of Conducting Matter, Superconduc- tivity (Springer-Verlag, Heidelberg, 2009).

[12] P. Drude, Annalen der Physik. **308**(11), 369 (1900).

[13] A. Bezryadin, Superconductivity in Nanowires: Fabrication and Quantum Transport (Wiley-VCH Verlag GmbH & Co. KGaA, 2013).

[14] N. D. Mermin, H. Wagner, Phys. Rev. Lett. **17**, 1133 (1966).

[15] J. S. Langer, V. Ambegaokar, Phys. Rev. **164**, 498–510 (1967).

[16] D. E. McCumber, B. I. Halperin, Phys. Rev. B **1**, 1054–1070 (1970).

[17] J. E. Lukens, R. J. Warburton, W. W. Webb, Phys. Rev. Lett. **25**, 1180–1183 (1970).

[18] R. S. Newbower, M. R. Beasley, M. Tinkham, Phys. Rev. B **5**, 864– 868 (1972).

[19] T. T. M. Palstra, B. Batlogg, L. F. Schneemeyer, R. B. van Dover, and J.

V. Waszczak, Phys. Rev. B, **38**, 5102 (1988).

[20] F. Altomare, A. M. Chang, One-dimensonal superconductivity in nanowires (Wiley-VCH Verlag GmbH & Co. KGaA, 2013).

[21] D. S. Golubev and A. D. Zaikin, Phys. Rev. Lett. **78**, 144502 (2008).

[22] H. Hilgenkamp, J. Mannhart, Rev. Mod. Phys. **74**, 485 (2002).

[23] R. Li, X. Z. Duan, X. Zhu, Y. Yang, D. B. Zhou, and Z. Q. Li, Solid State Commun. **279**, 34-38 (2018).

[24] K. Makise, F. Ichikawa, T. Asano, and B. Shinozaki, J. Phys. Condens. Matter **30**, 065402 (2018).

[25] M. C. Cha, M. P. A. Fisher, S. M. Girvin, M. Wallin, and A. P. Young, Phys. Rev. B **44**, 6883-6902 (1991).

[26] T. Kirzhner, and G. Koren, Sci. Rep. **4**, 6244 (2014).

[27] O. M. Froehlich, A. Beck, R. Gross, H. Sato, and M. Naito, Europhys. Lett. **36**, 467 (1996).

[28] J. M. Li, X. L. Zeng, A. D. Mo, Z. A. Xu, CrystEngComm, **13**, 6964, (2011).

[29] W. A. Little, Phys. Rev. **156**, 396 (1976).

[30] P. W. Anderson, A. H. Dayem, Phys. Rev. Lett. **13**, 195-197 (1964).

[31] A. J. Van Run, J. E. Mooij, Jpn J. Appl. Phys. **26**, 1765-1766 (1987).

[32] N. Giordano, Phys. Rev. Lett. **61**, 2137 (1988).

[33] A. Bezryadin, C. N. Lau, M. Tinkham, Nature **404**, 971–974 (2000).

[34] P. W. Anderson, Y. B. Kim, Rev. Mod. Phys. **36**, 39-43 (1964).

[35] B. S. Blagoev, T. K. Nurgaliev, V. Štrbik, E. S. Mateev1, A. J. Zaleski, Bulg. J. Phys. **40**, 337–347 (2013).

[36] A. E. Spivak, Y. A. Dzenis, and D. H. Reneker, Mech. Res. Commun. **27**, 37-42 (2000).

[37] J. M. Deitzel, C. Krauthauser, D. Harris, and J. Kleinmeyer, in Polymeric Nanofibers, ACS Symposium Series, edited by D. H. Reneker and H. Fong (American Chemical Society, Washington, DC, 2006), Vol. **918**.

[38] D. H. Reneker, H. Fong, Polymeric nanofibers (Washington, DC: American Chemical Society, 2005).

[39] A. L. Yarin, S. Koombhongse, and D. H. Reneker, J. Appl. Phys. **89**, 3018 (2001).

[40] A. J. Guenthner, S. Khombhongse, W. Liu, P. Dayal, D. H. Reneker, and T. Kyu, Macromol. Theory Simul. **15**, 87-93 (2006).

[41] J. E. Mark, 'Polymer Data Handbook', Oxford University Press, New York (1999).

[42] L. P. Gor'kov, Sov. Phys. JETP **36**, 1364 (1959).

[43] R. P. Feynman, R. B. Leighton, and M. Sands, The Feynman lectures on Physics, **III**, Quantum Mechanics, Addison-Wesley Publishing Company, Inc (1965).

[44] B. D. Josephson, Rev. Mod. Phys. **46** (2), 251–254, (1974).

[45] P. W. Anderson, J. M. Rowell, Phys. Rev. Lett. **10**(6), 230, (1963).

[46] A. A. Abrikosov, J. Phys. Chem. Solids, **2 (3)**, 199–208 (1957).

[47] C. Bean, Phys. Rev. Lett. **8**, 250-253 (1962).

[48] C. Bean, Rev. Mod. Phys **36**, 31-39 (1964).

[49] W. A. Frietz, W. W. Webb, Phys. Rev. **178**, 657 (1969).

[50] D. X. Chen, R. B. Goldfarb, R. W. Cross, and A. Sanchez, Phys. Rev. B: Condens. Matter **48**, 6426 (1993).

[51] D. X. Chen, A. Hernando, F. Conde, J. Ramirez, J. M. Gonzaález-Calbet, and M. Vallet, J. Appl. Phys. **75**, 2578 (1994).

[52] D. X. Chen, A. Sanchez, and J. S. Munoz, J. Appl. Phys. 67, 3430 (1990).

[53] D. M. Gokhfeld, D. A. Balaev, M. I. Petrov, S. I. Popkov, K. A. Shaykhutdinov, and V. V. Valkov, J. Appl. Phys. **109**, 033904 (2011).

[54] V. V. Val'kov and B. P. Khrustalev, Sov. Phys. JETP **80**, 680 (1995).

[55] D. M. Gokhfeld, Phys. Solid State **56**, 2298-2304 (2014).

[56] M. Forsthuber and G. Hilscher, Phys. Rev. B: Condens. Matter **45**, 7996 (1992).

[57] J. I. Gorina, G. A. Kaljujnaia, V. I. Ktitorov, V. P. Martovitsky, V. V. Rodin, V. A. Stepanov, A. A. Tsvetkov, and S. I. Vedeneev, Solid State Commun. **85**, 695 (1993).

[58] I. Chong, Z. Hiroi, M. Izumi, J. Shimoyama, Y. Nakayama, K. Kishio, T.

Terashima, Y. Bando, and M. Takano, Science **276**, 770 (1997).

[59] J. Shimoyama, Y. Nakayama, K. Kitazawa, K. Kishio, Z. Hiroi, I. Chong, and M. Takano, Physica C **281**, 69 (1997).

[60] J. Tao, S. Shivkumar, Mater. Lett. **61**, 2325-2328 (2007).

[61] D. Li, Y. Wang, Y. Xia, Nano. Lett. **3**, 1167-1171 (2003).

[62] K. Manabe, M. Mitarai, and S. Kujio, 'Bulletin of the Chemical Society of Japan **23**, 1', Chemistry & chemical industry **3(7)**, 26-33 (1950).

[63] P. Majewski, J. Mater. Res., **15**, 854-870 (2000).

[64] T. Kawai, T. Horiuchi, K. Mitsui, K. Ogura, S. Takagi, and S. Kawai, Physica C, **161**, 561-566 (1989).

[65] M. P. Volkov, B. T. Melekh, V. I. Bakharev, N. F. Kartenko, N. V. Matykin, and Yu. N. Filin, Phys. Solid State, **41**, 15-17 (1999).

[66] S. M. Khalil, Physica B, **391**, 130-135 (2007).

[67] W. W. Schmahl, M. Lehmann, S. Räth, M. Gerards and R. Riddle, Supercond. Sci. Technol., **11**, 1269-1276 (1998).

[68] X. L. Zeng, M. R. Koblischka, and U. Hartmann, Mater. Res. Express, **2**, 095022 (2015).

[69] M. R. Koblischka, X. L. Zeng, T. Karwoth, T. Hauet and U. Hartmann, AIP Adv. **6**, 035115 (2016).

[70] M. R. Koblischka, X. L. Zeng, T. Karwoth, T. Hauet, U. Hartmann, IEEE Trans Appl. Supercond., **26**, 1800605 (2016)

[71] X. L. Zeng, M. R. Koblischka, T. Karwoth, U. Hartmann, D. Gokhfeld, C. Chang, T. Hauet, Phys. Rev. Mat. **1**, 044802 (2017)

[72] X. L. Zeng, M. R Koblischka, T. Karwoth, T. Hauet, and U. Hartmann, Sci. Technol. **30**, 035014 (2017).

[73] X. L. Zeng, M. R. Koblischka, F. Laurent, T. Karwoth, A. V. Koblischka, U. Hartmann, C. Chang, P. Kumar, O. Eibl, IEEE Trans. Appl. Supercond. **28**, 1-5 (2018).

[74] Z. M. Huang, Y. Z. Zhang, M. Kotakic, S.Ramakrishnabcd Compos. Sci. Technol. **63**, 2223 (2003).

[75] D. Lampakis, D. Palles, E. Liarokapis, C. Panagopoulos, J. R. Cooper, H. Ehrenberg and T. Hartmann, Phys. Rev. B: Condens. Matter, **62**, 8811 (2000).

[76] W. H. Weber, C. R. Peters and E. M. Logothetis, J. Opt. Soc. Am. B, **6**, 455 (1989).

[77] S. Sugai, Phys. Rev. B, **39**, 4306 (1989).

[78] S. Sugai, S. I. Shamoto and M. Sato, Phys. Rev. B, **38**, 6436 (1988).

[79] S. Sugai, Y. TakayanagiN. HayamizuY. SoneN. NakagawaT. Muroi, J. Supercond. Nov. Magn., **26**, 2697–2701 (2013).

[80] B. Vignolle, S. M. Hayden, D. F. McMorrow, H. M. R∅nnow, B. Lake, C. D. Frost and T. G. Perring, Nat. Phys., **3**, 163 (2007).

[81] N. Hudakova, V. Plechacek, P. Dordor, K. Flachbart, K. Knizek, J. Kovac and M. Reiffers, Supercond. Sci. Technol. **8**, 324 (1995).

[82] L. Winkeler, S. Sadewasser, B. Beschoten, H. Frank, F. Nouvertné and G. Güntherodt, Physica C **265**, 194 (1996).

[83] A. Sotelo, Sh. Rasekha, G. Constantinescu, H. Amaveda, M. A. Torres, M. A. Madre and J. C. Diez, J. Eur. Ceram. Soc. **34**, 2977 (2014).

[84] M. Werner, F. M. Sauerzopf, H. W. Weber and A. Wisniewski, Phys. Rev. B **61**, 14795 (2000).

[85] O. Kizilaslan, G. Kirat and M. A. Aksan, J. Magn. Magn. Mater. **384**, 186 (2015).

[86] M. Jirsa, L. Půst, D. Dlouhýaa and M. R. Koblischka, Phys. Rev. B **55**, 3276 (1997).

[87] V. Oganesyan, D. A. Huse, and S. L. Sondhi Phys. Rev. B **73**, 094503 (2006).

[88] M. R. Koblischka and J. Sosnowski, Eur. Phys. J. B **44**, 277 (2005).

[89] S. Senoussi, J. Phys. III France, **2**, 1041-1257 (1992).

[90] P. N. Mikheenko, K. K. Uprety, and S. X. Dou, BSCCO, in Handbook of Superconducting Materials, **1**, edited by D.A. Cardwell and D. S. Ginley (IOP Publishing, Bristol, UK, 2003).

[91] D. M. Gokhfeld, D. A. Balaev, S. I. Popkov, K. A. Shaykhutdinov, and M. I. Petrov, Physica C **434**, 135 (2006).

[92] A. Maeda, Y. Iino, T. Hanaguri, N. Motohira, K. Kishio, and T. Fukase, Phys.Rev.Lett. **74**, 1202 (1995).

[93] R. Prozorov, R. W. Giannetta, A. Carrington, P. Fournier, R. L. Greene, P. Guptasarma, D. G. Hinks, and A. R. Banks, Appl. Phys. Lett. **77**,

4202-4204 (2000).

[94] D. Dew-Hughes, Philos. Mag. **30**, 293 (1974).

[95] M. Eisterer, Phys.Rev.B **77**, 144524 (2008).

[96] P. Fabbricatore, C. Priano, A. Sciutti, G. Gemme, R. Musenich, R. Parodi, F. Gomory, and J. R. Thompson, Phys. Rev. B **54**, 12543 (1996).

[97] B. Chen, W. Halperin P. Guptasarma, D. G. Hinks, V. F. Mitrović, A. P. Reyes, and P. L. Kuhns, Nature Physics 3, 239-242 (2007).

[98] P. Badica, K. Togano, S. Awaji, K.Watanabe, and H. Kumakura, Supercond. Sci. Technol. **19**, R81 (2006).

[99] F. Kametani, J. Jiang, M. Matras, D. Abraimov, E. E. Hellstrom, and D. C. Larbalestier, Sci. Rep. **5**, 8285 (2015).

[100] T. Karwoth, Master Thesis, 'Electronic Transport Measurements on Electrospun High-Tc Superconducting Fibers', (2016).

[101] M. Tinkham, J. U. Free, C. N. Lau, and N. Markovic, Phys. Rev. B, **68**, 134515 (2003).

[102] K. Xu, J. R. Heath, Nano Lett., **8**, 3845-3849 (2008).

[103] M. Tinkham, C. N. Lau, Appl. Phys. Lett., **80**, 2946-2948 (2002).

[104] H. Meissner, Phys. Rev. **117**, 672 (1960).

[105] O. Yuli, I. Asulin, O. Millo and D. Orgad, Phys. Rev. Lett. **101**, 057005 (2008).

[106] T. Kawai, T. Horiuchi, K. Mitsui, K. Ogura, S. Takagi, and S. Kawai, Physica C, **161**,561-566 (1989).

[107] M. P. Volkov, B. T. Melekh, V. I. Bakharev, N. F. Kartenko, N. V. Matykin, and Yu. N. Filin, Phys. Solid State, **41**, 15-17 (1999).

[108] S. M. Khalil, Physica B, **391**, 130-135 (2007).

[109] O. Eibl, Physica C, **168**, 239-248 (1990).

[110] A. Veneva, D. K. Petrov, P. Dittrich, and M. J. Naughton, Physica C, **271**, 230-234 (1996).

[111] C. A. M. dos Santos, C. J. V. Oliveira, M. S. da Luz, A. D. Bortolozo, M. J. R. Sandim, and A. J. S. Machado, Phys. Rev. B, **74**, 184526 (2006).

[112] B. Gopalakrishna, M. Chandra Sekhar, and S. V. Suryanarayana, Cryst.

Res. Tech- nol., **30**, 411-417 (1995).

[113] A. Veneva, D. K. Petrov, P. Dittrich, and M. J. Naughton, Physica C, **271**, 230-234 (1996).

[114] I. Nedkov, Supercond. Sci. Technol., **11**, 21-25 (1998).

[115] A. Wiederhold, Master Thesis, 'Charaterization of individual filaments of high-temperature superconductors', (2018).

[116] Mikitik, G.P., Brandt, E.H.: Phys. Rev. B **64**, 184514 (2001).

[117] Nakamura, M. et al. Physica C **259**, 295 (1996).

[118] C. Boulesteix, Y. Marietti, T. Badèche, H. Tatarenko-Zapolsky, V. Grachev, O. Monnereau, H. Faqir, and G. Vacquier, J. Phys. Chem. Solids **61**, 585 (2000).

[119] D. L. Rocco, R. Almeida Silva, A. Magnus, G. Carvalho, A. A. Coelho, J. P. Andreeta, S. Gama, J. Appl. Phys. **97**, 10M317 (2005).

[120] M. Dominiczak, A. Ruyter, P. Limelette, I. M. Laffez, F. Giovannelli, M. D. Rossell, G. V. Tendeloo, Solid State Commun. **149**, 1543 (2009).

[121] T. Sarkar, M. V. Kamalakar, A. K. Raychaudhuri, New J. Phys. **14**, 033026 (2012).

[122] Ll. Balcells, J. Fontcuberta, B. Martinez, X. Obradors, Phys. Rev. B **58**, R14697 (1998).

[123] W. J. Lu, Y. P. Sun, X. B. Zhu, W. H. Song, and J. J. Du, Mat. Lett. **60**, 3207 (2006).

[124] B. Jugdersuren, S. Kang, R. S. Di Pietro, D. Heiman, D. McKeown, I. L. Pegg, J. Philip, J. Appl. Phys. **109**, 016109 (2011).

[125] B. X. Huang, Y. H. Liu, X. B. Yuan, C. J. Wang, R. Z. Zhang, and L. M. Mei, J. Magn. Magn. Mater., **280**, 176 (2004).

[126] K. Vijayanandhini and T. R. N. Kutty, J. Phys. D: Appl. Phys., **39**, 2902 (2006).

[127] S. Kar, J. Sarkar, B. Ghosh and A. K. Raychaudhuri, J. Nanosci. Nanotech., **7**, 2051 (2007).

[128] Ll. Balcells, J. Fontcuberta, B. Martinez and X. Obradors, Phys. Rev. B, **58**, R14697 (1998).

[129] X. M. Cui, W. S. Lyoo, W. K. Son, D. H. Park, J. H. Choy, T. S. Lee, and W. H. Park, Supercond. Sci. Technol. **19**, 1264–1268 (2006).

[130] E. A Duarte, N. G Rudawski, P. A Quintero, M. W Meisel, and J. C Nino, Supercond. Sci. Technol. **28**, 15006-15013 (2015).

[131] W. H. Mallison, S. J. Berkowitz, A. S. Hirahara, M. J. Neal, and K. Char, Appl. Phys. Lett. **68**, 3808 (1996).

[132] V. V. Ryazanov, V. V. Bol'ginov, D. S. Sobanin, I. V. Vernik, S. K. Tolpygo, A. M. Kadin, and O. A. Mukhanov, Phys. Procedia **36**, 35-41 (2012).

List of Figures

List of Tables